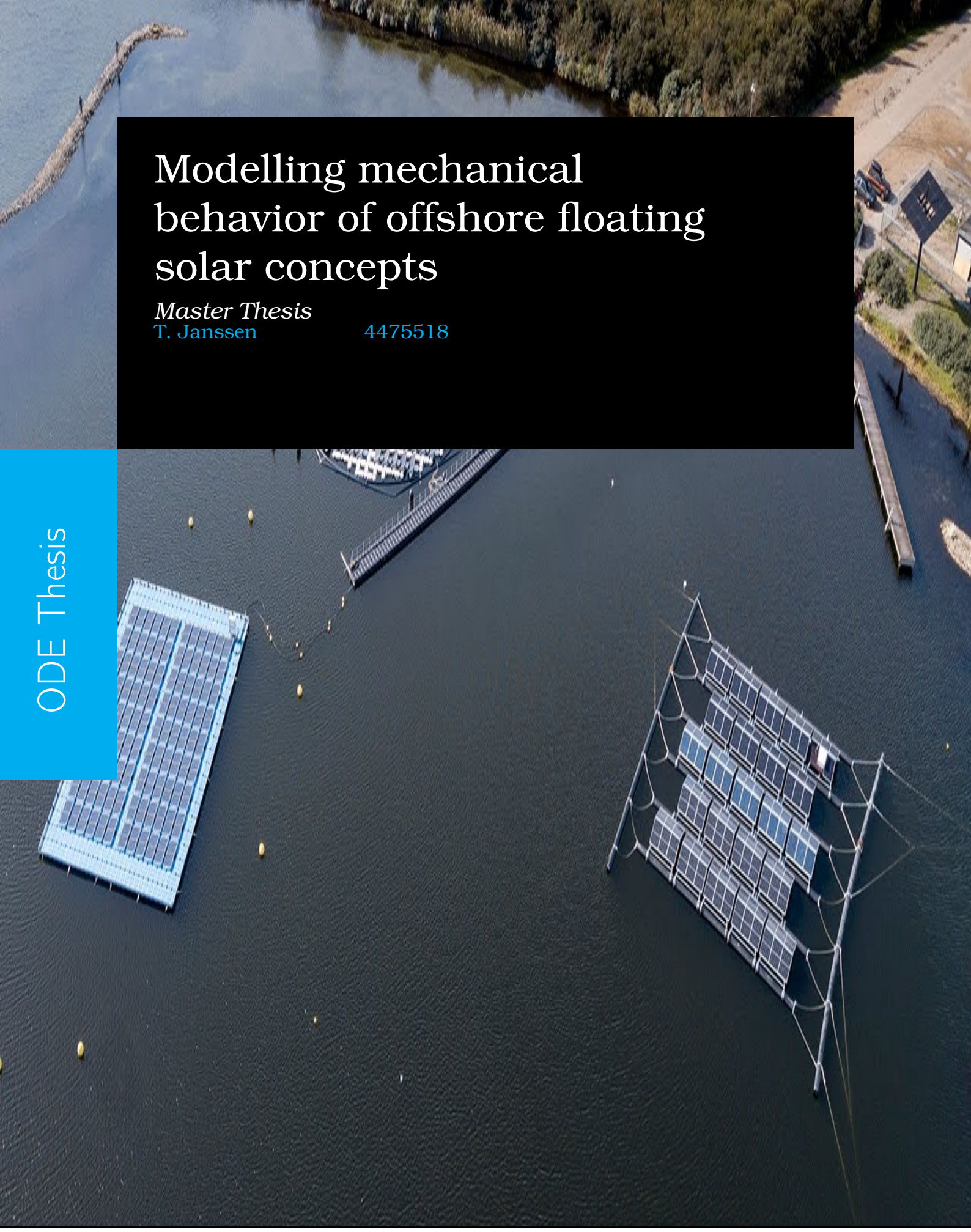

Modelling mechanical behavior of offshore floating solar concepts

Master Thesis

T. Janssen 4475518

ODE Thesis

TU Delft Delft University of Technology

TNO innovation for life

April 29, 2022

Modelling mechanical behavior of offshore floating solar concepts

by
Tjeerd Janssen

performed at TNO

To obtain the degree Master of Science
at the Delft University of Technology

To be defended on the 11th of May 2022

Company supervisors
Responsible supervisor: Ir. M.G. Hoogeland

TU Delft supervisors
Chair: Dr. ir. A. Jarquin Laguna
Committee member: Dr. ir. A. Antonini
Committee member: Dr. ir. O.J. Colomés Gené
Committee member: Dr. ir. H. Hendrikse

Author details
Student number: 4475518

The front page contains an image from TNO of different floating solar concepts on Oostvoornse Lake.[1]

Abstract

The world is currently in a global energy transition. To reach the goals set by the International Energy Agency massive deployment of clean and efficient energy technologies is required. To scale up the use of solar photovoltaic (PV), large areas of solar farms are needed. One of the suitable solutions for this is offshore floating PV, for which several concepts are currently being developed. This study explores one of these concept designs, a design consisting of offshore floating PV structures using interconnected rectangular floaters on which the solar panels are mounted. The study focuses on modelling and predicting the forces that arise in the connections between these panels due to the motion and loading of the offshore PV structure in waves. This research aims to to give insight into the interaction between connection forces and different concept choices regarding the size of the floaters and the connection compliance of the connections between the floaters.

A model consisting of two floaters connected with two connections at each end is developed. The forces and motions of the floating structure are computed in the frequency domain. First, the hydrodynamic coefficients and wave excitation forces are obtained using the open source boundary element method (BEM) software NEMOH. Two different complications arise when using NEMOH, irregular frequencies and unrealistically high gap resonance peaks. A method is developed to deal with the removal the irregular frequencies as this is not a physical phenomenon. Another method is developed to suppress the gap resonance in the gap between the floaters. The results are validated using earlier studies by Sun et al.[1] and show good resemblance. The connections between the floater are modelled as a set of linear springs in all degrees of freedom and are implemented into the equation of motion in frequency domain as a joint stiffness matrix. The motions of the connected structure are validated using another study by Sun and Choo [2].

The influence of the design choices is then investigated for application at the North sea for two different wave directions. The results are obtained as a force energy density spectrum for each degree of freedom. The results are analysed and compared using the significant value of the force energy density spectrum. First, four different dimensions are varied, the length, the width and the draft of the floaters and the size of the gap between the floaters. Secondly, the connection stiffness is varied in four different directions, axial, shear, bending and torsion.

With the developed model the interaction between forces and moments in the connections and different design choices can be quantified. The results can be used to give an initial indication of the occurring forces within the connections between two floaters for application at the North sea and allows simulation of effects of different design choices. However, non-linear effects are not taken into account as well as mooring design and can be implemented in future work. Furthermore, only two bodies with connections are modelled, this can be extended to a grid or multiple connections at different locations. This can be implemented in future work.

[1] L. Sun et al, 2010, First- and second-order analysis of resonant waves between adjacent barges, Journal of Fluids and Structures

[2] Choo Y.S., Sun L., Eatock Taylor R., 2011, Responses of interconnected floating bodies. The IES Journal Part A: Civil and Structural Engineering

Acknowledgements

After a bachelor in Mechanical engineering, this thesis marks the end of the master Offshore and Dredging Engineering at the TU Delft. I would like to give my appreciation to all people that helped me during my time as a student.

First of all I would like to thank Martijn Hoogeland from TNO for his guidance on my thesis through our meetings and for his feedback. I would also like to thank the rest of the TNO staff, of the structural dynamics department and other departments, that helped during my research.

Secondly, I would like to thank my graduation committee members, Antonio Jarquin Laguna as the chair and Alessandro Antonini and Oriol Colomes Gene as committee members for their guidance in the process and their useful feedback on the results. I would also like to thanks Hayo Hendrikse for joining the graduation committee as an external member.

A special thanks goes out to my roommates, Jochem, Koen, Jip and Dennis for their support and motivation during my master and my thesis. As well as some much needed relaxation now and then. I would also like to thank my friend Gerard, for all the time we studied together during the master Offshore and Dredging Engineering.

A very special thanks goes out to my parents and sisters for all their love and support during my years in Delft and for giving me the opportunity to be able to do this. Especially my mom for giving her feedback on my report.

Finally, I want to thank all the people that I forgot to mention that supported me and helped my during my studies in Delft!

Tjeerd Janssen, May 2022

Contents

List of Figures

List of Tables

Chapter 1 Introduction

In this chapter offshore floating solar and its concept developments are introduced. Section 1.1 explains why offshore floating solar is important in our current world. Section 1.2 describes several different offshore floating solar concepts already existing or currently under development. In section 1.3 the design choices made in these offshore floating solar concepts are evaluated. This leads to the research question and subquestions for this thesis that are formulated in section 1.4. Section 1.5 will give an outline of the the rest of the report.

1.1 Importance Offshore Floating Solar

The world is currently in a global energy transition. Global warming is one of the large problems of our current time. The energy sector is responsible for around 75 % of greenhouse gas emissions in 2020 [19]. There is a global goal to building an energy sector with net-zero emissions by 2050. A large number of governments are pledging to reduce their greenhouse gas emissions to net zero. However, the demand for energy still rises and is expected to double and exceed 50000 TWh in 2050 [20]. In a report of the International Energy Agency (IEA) it is stated that the path to net-zero emissions "requires massive deployment of all available clean and efficient energy technologies"[19]. They also state that to stay on the path of net-zero emissions, solar and wind energy should be largely scaled up. For solar Photo Voltaic (PV) that means installing an equivalent of the world's current largest solar park roughly every year [19].

To achieve this increase in energy production by PV, large areas of solar farms are needed. However, there is increasing scarcity of space on land due to the growing global population and an increase in food consumption [21]. Furthermore, the space that is available on land is mostly not in the proximity of the end-user of the energy in large urban areas. Therefore, more countries and companies are looking to place their solar farms offshore, as there is an abundance of space available at sea. Furthermore, PV panels offshore can be cooled by seawater to increase the PV conversion efficiency [22] and thus further increasing the potential for offshore floating solar. The development of floating PV (FPV) is already growing significantly as can be seen in figure 1.1 (until 2018). However, most of the installed FPV is on inland waters and lakes.

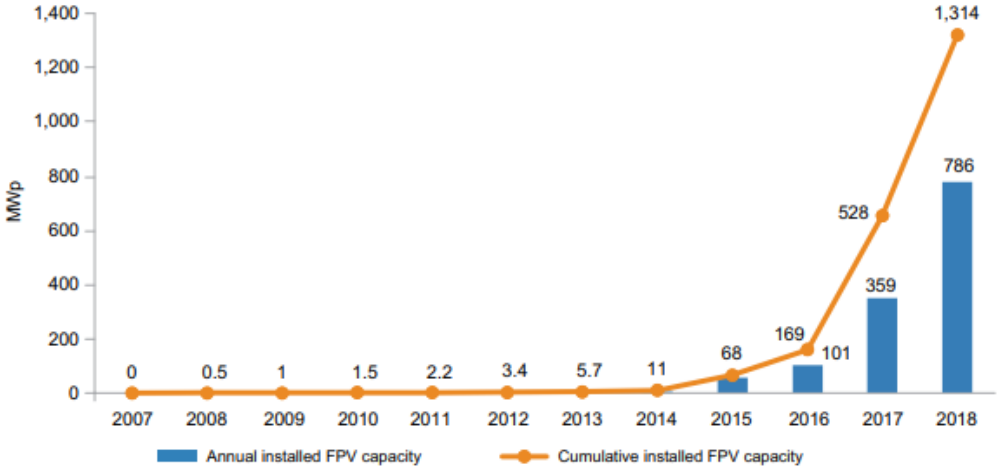

Figure 1.1: Global installed floating PV capacity and annual additions until 2018 [2]

1.2 Different Concepts

In recent years, several companies are starting to develop offshore solar farms. A few of those concepts can be seen underneath. As can be seen, there are multiple design choices for each of these concepts.

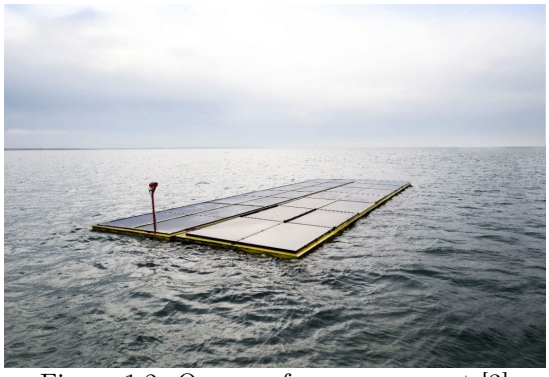

Figure 1.2: Oceans of energy concept [3]

The first concept shown in figure 1.2 shows the concept from Oceans of Energy. They use the pontoon concept. It consists of multiple stiff pontoons hinged to one another. The solar panels are mounted on top of the pontoons. The first pilot for this concept was a 17 kW solar farm. [3]

The second concept shown is the SUNdy concept by DNV in figure 1.3. It consists of a hexagonal structure with flexible thin-film PV panels that can move with the waves. The concept is a sort of spider-web with the thin-film PV panels between held in place using cables. It uses lengthy spread moorings to hold the structure in place. It consists of 4200 PV panels with a total capacity of around 2 MW.[4]

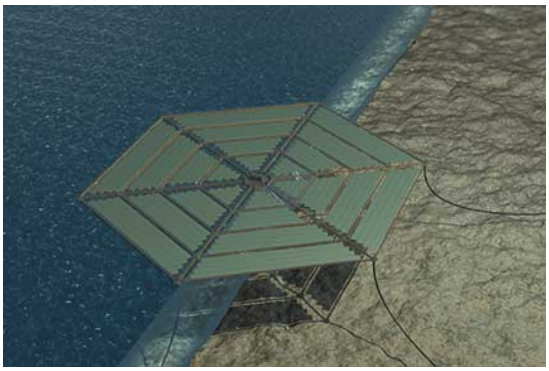

Figure 1.3: SUNdy concept [4]

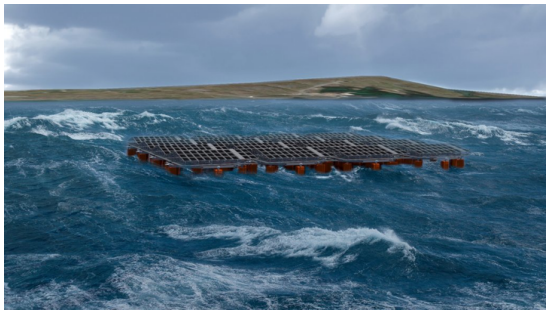

Figure 1.4: Moss-Maritime concept [5]

The third concept shown in figure 1.4 is the concept of Moss-Maritime. The structure is about 80x80m and keeps the PV panels roughly 3m above the sea surface. It consists of small size floaters that hold a lattice structure on which the PV panels are mounted. [5]

The fourth concept in figure 1.5 shows the SwimSol concept currently installed near the Maldives. It is called SolarSea and consists currently of 12 platforms.The platforms are made up of a stiff structure with the PV panels on top well above the water surface. [6].

Figure 1.5: SwimSol concept [6]


Figure 1.6: Oceansun concept [7]

The fifth figure, figure 1.6, shows the Oceansun concept. It is a large circular floating membrane that is in direct contact with the water with a ring structure around to protect the panels from the waves. Due to the direct contact with the water, the panels are directly cooled and therefore have an higher energy yield than structures with an air gap between the water and panels. [7]

The last concept is the concept of the company SolarDuck. The structure consist of vertical buoys that hold up a triangular structure with the PV panels on top. These stiff triangular structures can be hinged to eachother to create a large solar farm. The PV panels are elevated above the waterline to keep them dry. [8]

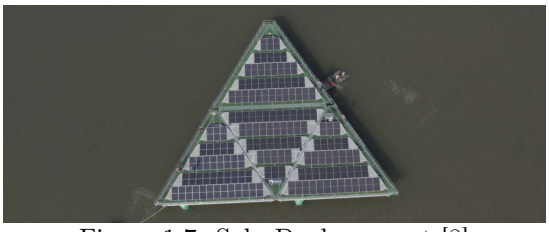
Figure 1.7: SolarDuck concept [8]

1.3 Design Choices

As seen there are multiple design choices possible in offshore solar. There are stiff floating structures that are hinged to one another and have the PV panels high above sea level such as the Solarduck structure. There are also stiff floating structures that are hinged that hold the PV panels much closer to the water, such as the Oceans of energy concept. There are very flexible structures that move with the waves, such as the mattress structure of SUNdy project. Or a fully stiff floating system such as the Swimsol concept. The flexible floating structures are not in the scope of this research due to time constraints. Thus, only rigid floater elements are considered.

Two important aspects to consider when designing offshore floating solar structures using stiff elements are:

- Floatersize or Elementsize
- Connection design

In the next subsections, these two aspects will be further explained.

1.3.1 Floatersize or element size

The size the individual floater elements has a large influence on the hydrodynamic forces and wave-structure interaction and therefore the response of the structure. A very large stiff floater will ignore small and short waves relative to the dimension of the structure, but as the waves get larger, the forces on the structure will increase and therefore the motions of the structure will increase. Furthermore, different dimensions such as width, draft and length all influence the motions and forces within the structure differently.

1.3.2 Connection design

The way the floater elements are connected to each other and the way the connections are designed influences the relative motion between the floaters. When designing offshore floating solar structures, the compliance of the connection should be considered carefully as this will influence the forces within the connections and the relative motion of the floaters. Furthermore, the forces arising within the connections due to the relative motions of the floaters are an important design criterion when designing offshore floating structures.

1.4 Research goal

When designing offshore floating solar concepts the element size and connection compliance have to be considered carefully. Varying in these two areas will give a different dynamic behavior in an offshore environment, due to their difference in size and connection design and thus also in their water-structure interaction. Depending on the offshore environmental conditions, an optimum combination may exist for each of the variables. Therefore, the structural integrity, forces within the connection and robustness of the different concepts needs evaluation. A model that describes the behavior of these offshore floating solar concepts in offshore waters can give more insight in these aspects. This thesis will go deeper into the forces and structural dynamics of the offshore floating solar concepts in order to evaluate the robustness of the concepts and guide robust offshore floating concept design. This raises the first and main research question:

What is the interaction between connection forces and different concept choices regarding the size of offshore floating solar platforms and the connection compliance between them?

In order to obtain the forces on the structure and in the connections, a model has to be created to obtain the wave-induced motions of the structure. The model will be a general simplified model that gives an initial insight in the dynamics and mechanics of the different floater sizes and connection compliance. Using this model, the influence of the floater size on the dynamical behavior can be analyzed. Furthermore, the influence and floater-to-floater connection flexibility on the dynamical behavior can be analyzed as well. This analysis can in a later stage be used to optimize different design aspects.

This raises the following follow-up questions:

What is the influence of different floater sizes on the connection forces?

As can be seen in the currently existing concepts that are shown earlier, all concepts have very different sizes. So the influence of these different sizes has to be investigated. Different floater size selection should be incorporated into the model in order to analyse the influence of the floater size on the forces.

The next aspect that can differ in the concepts is the compliance of the connection. So this raises the second follow-up question:

What is the influence of the connection compliance on the connection forces?

The connection compliance has a big influence on the motion of the structure in the waves. Therefore, it has an influence on the connection forces. Different connection compliance will have to be implemented in the model to investigate the influence of this aspect.

At last, wind forces will have an impact on the different design choices. Wind forces are not taken into account in this research, but should be investigated in further research.

1.5 Outline

The next chapter, chapter 2, presents a review of relevant literature in the field of modelling floating solar structures for both stiff and flexible structures. The flexible floating structures are not further analysed in the research as this was left out of the scope. In chapter 3 the methodology used to solve the research question is described and the basic elements of the model are evaluated and selected. Chapter 4 further elaborates on the model, detailing specific aspects and solving data artefacts related to software choices. The model is tested and validated with results from literature as described in chapter 5. In chapter 6 and 7 the results for 2 different test cases, varying size and connection stiffness, are presented. These are discussed in chapter 8, leading to conclusions in chapter 9.

Chapter 2 Literature

In this chapter, the relevant literature is presented that displays the currently existing models for offshore floating solar farms as well as different modelling choices that have been made in earlier studies. In the first section, section 2.1, the literature on very large floating structures is presented after which section 2.2 goes into more detail on the current existing models for offshore floating solar. Section 2.2.1 gives insight into the modelling of flexible floating structure, section 2.2.2 explains more on the current literature about modelling stiff floating structures. In the last part of this chapter, more information is given about the working conditions in section 2.3 and literature about calculating wind loads in section 2.4.

2.1 Very Large Floating Structures, VLFS

In the late 20th century and early 2000s very large floating structures (VLFS), such as floating airports, enjoyed research and industrial attention. Research efforts were dedicated to model the hydro structural interaction of VLFS. M. Kashiwagi did a lot of research into a very large near shore floating airport in Japan [23] [24] [25]. In his first research Kashiwagi developed a scheme for computing the wave-induced hydroelastic response of a VLFS [23]. In his second work he providess a review on other studies on the hydroelastic response of VLFS and goes further into what should be done in future works [25]. In the last paper from 2004 he goes into the elastic deformation caused by landing and take-off of an airplane on a pontoon-type VLFS. Kashiwagi uses a time-domain expansion method for this [24]. The work of Kashiwagi gives insight into a scheme on modelling the elastic response of very large floating structures in the time domain. The scheme developed in his first work can be used as a basis for the response calculation of the fully flexible floating solar concepts. The work on the landing and take-off of an airplane is for this study not of importance.

In the field of VLFS, Andrianov has proposed a new method to solve wave-structure interaction problems for VLFS in an analytical way [9]. Andrianov used a thin elastic plate as a model of VLFS. He solved the the problem for six different shapes and used 3 different water depths: infinite, finite and shallow water depth. He found that for realistic values of the rigidity and mass, the plate deflections very small, much smaller than the waves, so in practice, VLFS are very stable in a way that it doesn't move structures on the floating structure or unbalance people walking on the structure.

Figure 2.1: Near shore floating airport in Japan, also called the Megafloat [9]

Also, the field of VLFS, Hamamoto has done research in the dynamic response of an artificial floating island subjected to wind waves and sub marine earthquakes. Hamamoto uses modal superposition approach [26]. In 2002, Khabakhpasheva and Korobkin have also done research into the hydroelastic behaviour of floating plates in waves. They modelled the plate by an Euler beam and solved the response numerically. They used basic functions to compute the pressure distribution and beam deflection for plates with different boundary conditions [27]. Further work is done by Riyansyah et al. [28]. Riyansyah et al. looked further into the connection design for a two floating beam system for a pontoon type VLFS. They used the frequency domain approach

for the hydroelastic analysis and the beams are modelled by the Euler-Bernouilli beam theory. Wang et al. also present a mathematical formulation for the hydroelastic analysis of VLFS in the frequency domain and also present some mitigation methods to reduce the structural response. They used a plate with the same dynamic properties in terms of vibration modes and natural periods as a simplified model for the actual VLFS [29]. Finally, Wei et al. present a time-domain method for computing the hydroelastic response of VLFS in inhomogeneous waves based on Cummins' equation [30]. They use frequency-domain hydrodynamic coefficients and transform them into the time-domain hydroelastic model using Cummins' equation. They show that the inhomogeneity of the waves has a significant effect on bending moments, shear forces and torsional moments of the structure [30].

As can be seen, there has been a lot of research into VLFS. The studies all use plates or beams to model the VLFS. They use linear models and only take into account small vertical deflections. Furthermore, only Wei et al. obtain the response of the structure for inhomogeneous waves [30]. These studies all consider very large floating islands with lengths approximately 1000m and larger. The sizes are not in comparison to what is used for this research. However, the modelling approaches used to calculate the response of such a flexible structure can be used to evaluate the response of a smaller flexible floating solar structure and that it can be modelled using an Euler-Bernouilli beam. The work of Riyanyah et al. can be used to evaluate the connection between flexible floating islands [28].

2.2 Models of floating solar

In this section, some of the currently existing models for floating solar are discussed and the methods they used. In the subsections hereafter, currently existing literature about modelling of flexible and stiff floating structures is discussed.

Lee et al. [10] used CFD for wind load analysis and AQWA for wave analysis on a 4x4 array floating PV structure as can be seen in figure 2.2. This figure shows the 3D model, the top shows one unit, the bottom shows the full assembly of the structure. The full assembly consists of main floating bodies with PV panels on top. At the edge there are road blocks that help the system float and help protect the main bodies.

Lee et al. [10] used ANSYS Fluent software for the CFD model for the wind loads. For the wave loads the ANSYS AQWA software was used. They calculated the flow velocity and pressure using the Reynolds-Averaged Navier-Stokes equation. It uses the continuity equation and momentum equation. For the wave diffraction they use the potential theory using the Laplace equation.

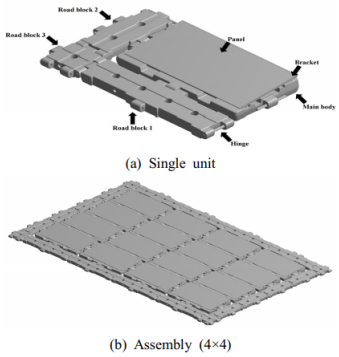

(a) Single unit

(b) Assembly (4×4)

Figure 2.2: 3D model used by Lee et al.[10]

A figure of the results of the AQWA CFD software for incident waves of 0.2m and 1.3m is shown in figure 2.3. Furthermore, they compare the results of the numerical analysis with the results of a more conventional design method. For the wind and wave loads this conventional method calculates the loads using the harboring and fishing design criteria as written by the Ministry of Maritime Affairs and Fisheries. They concluded that the discrepancy between the conventional design method and the numerical simulations was less than 20% for the wave load analysis [10]. However, they only did an analysis for 0.2m and 1.3m waveheight with a wavelength of 16.2m, so rather shallow waves. They furthermore concluded that the conventional design method for wind loads on the structure significantly overestimates the wind load on the PV structure in comparison with the CFD method. [10].

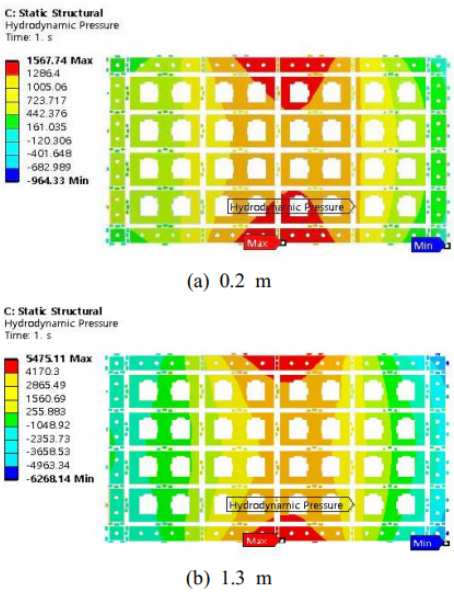

(a) 0.2 m

(b) 1.3 m

Figure 2.3: Result of pressure due to waves at 0.2m and 1.3m[10]

Al-Yacouby et al. [31] conducted a study on the hydrodynamic response of an offshore floating PV pontoon concept subjected to regular waves. Al-Yacouby et al. used analytical simulations using linear airy wave theory and validated the results using CFD simulations. They calculated the Response Amplitude Operators (RAOs) of the structure for surge, heave and pitch using model tests done earlier by Marijuan [32] and Kurian et al.[33]. From which they calculated the response of the structure. They conducted the study for different wave heights, wave periods, water depths and pontoon diameters. The results show that wave height, wave period and pontoon diameter have a large influence on the hydrodynamic loads. The water depth has significantly less influence. Furthermore, the comparison between the two methods shows only 3-4% difference, which is, according to Al-Yacouby et al., within the acceptable limits [31].

2.2.1 Modelling of flexible floating structures

For modelling flexible floating structures, there is not much literature available. Almost all literature about flexible floating structure comes back to VLFS structures, not much research has gone into smaller flexible floating structures such as the oceansun concept [7]. The VLFS literature as mentioned in the previous section, section 2.1, models the structure as a beam or plate and not as a fully flexible membrane. However, Ohkusu and Namba did a hydroelastic analysis for large floating structures for a thin and elongated rectangular plate configuration as seen in figure 2.4. In this configuration the length L and width B are kilometers while the draft is just a couple of meters. They presented an analytical approach to predict the bending vibration of such a structure under the action of a monochromatic incident wave [11]. In this study they used the same values for bending rigidity and Poisson's ratio of the

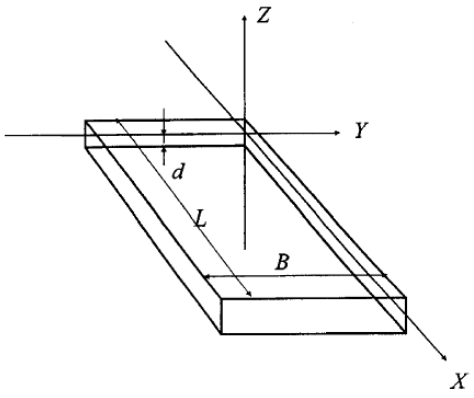

Figure 2.4: Rectangular plate configuration as used by Ohkusu and Namba [11]

structure as Kashiwagi[23]. The results of the analytical approach are also compared to the results Kashiwagi. Both studies have a relatively good agreement in the deflection of the plate. However, the method used by Ohkusu requires way less computational effort than the model by Kashiwagi [11]. It can be concluded that the modelling approaches used for VLFS can be a solid basis to develop a model for smaller flexible floating structures.

In the field of flexible floating structures, Sjoerd van Hoof has done research into the performance of a Finite element model (FEM) for very flexible floating structures for his master thesis in 2021 [34]. He developed a finite element model to asses the hydroelastic behaviour and compare it to experimental research done earlier by Schreier and Jacobi [35]. The model is both in 2D as well as 3D. The floating structure is modelled as an Euler-Bernoulli beam. The report from Van Hoof goes not much further into detail about the movements of the flexible floating structure itself. The report mainly describes the hydroelastic wave deformation caused by the floating structure.

2.2.2 Modelling of stiff floating structures

In the field of stiff floating structures Dombre et al. developed a numerical model for solving wave-structure interaction based on full non-linear potential flow and rigid body approach [36]. They coupled the full non-linear potential flow model to a floating rigid body in order to calculate the motion. Here they assume an incompressible and non-viscous fluid, as well as an irrotational flow. Therefore they can use a Laplace equation in the fluid domain because the velocity potential must satisfy mass conservation. They verified the accuracy and convergence for a forced motion of the body. For small amplitude motions, Dombre et al. observed a very close agreement with the results for linear theory. For large motions the error was larger.

The work from Dombre et al. is an extension on the work done earlier by Guerber et al. Guerber et al. developed a model for fully nonlinear interaction of ocean waves and fully submerged structures. The model is based on potential flow theory.[37] However, the work from Guerber et al. is only valid for fully submerged bodies. Dombre et al. extended the model to bodies at the free surface.

A.B.Z. Feys has done research in a new offshore floating solar concept during his master thesis. The thesis called: 'Support structure for offshore solar: The proposal of a new concept' goes into detail about a new concept design [12]. In the thesis, he designs a buoy and beam structure in a triangular shape, just like the SolarDuck concept. The beams are hinged to the buoys. The beams form a platform on which the PV panels are mounted. In the study, he considers the heave response of the structure to be the most critical response, as this response, when too large, can cause slamming of the water against the panels and structure. When modelling the heave response he uses regular waves and he assumes the buoys to be all cylindrical. Furthermore he uses a small angle approximation to linearize the equation of motion. For the hydromechanical theory he uses airy wave theory and the Morison equation to calculate the loads on the beams, Froude-Krylov was used to calculate the vertical loads on the buoys.

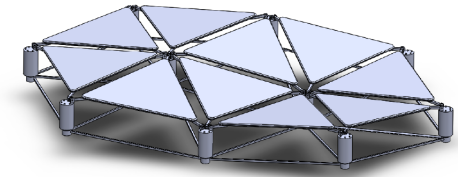

Figure 2.5: Proposed Buoy-Beam structure Feys [12]

In order to calculate the suitable dimensions for the structure, Feys varies different inputs to then see the heave response of the structure. He also uses different layouts of the structure to check the difference in response for multiple layouts. The calculations are all done in the frequency domain in order to find the frequency response of the structure. Figure 2.6 shows one of the results from the paper of Feys where he compared the frequency response in heave of a 5 buoy in-line system vs. a 19 buoy hexagonal system. As can be seen, the frequency response for the 5 buoy in line system is much larger than the 19 buoy system. In the end he proposes a 19 buoy hexagon structure with a lower eigenfrequency than the waves , because within the set of parameters that was used, a 19 buoy system configuration with a high eigenfrequency was not found [12].

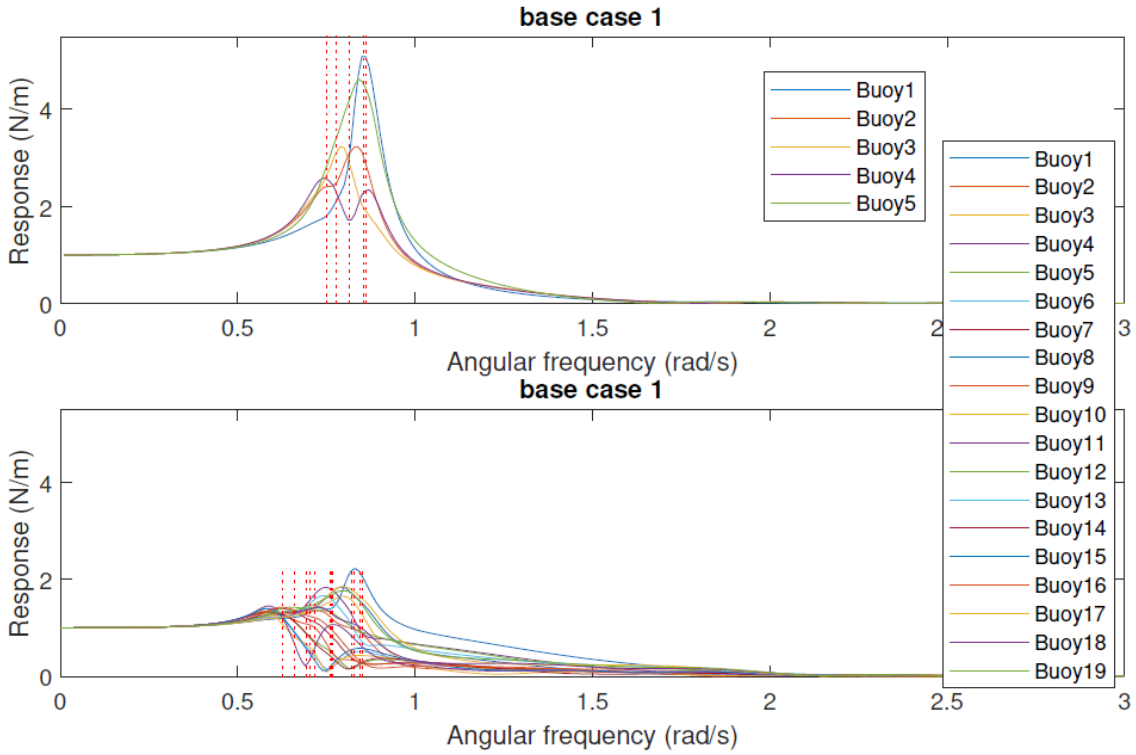

Figure 2.6: Frequency response of 5 buoy inline system (top) and a 19 buoy hexagon system with same element dimensions as the 5 buoy system as found by Feys [12]

A more complex model has been developed by Ma and Yan [13]. They developed a model using the finite element method (FEM). They first applied their model to 2D systems. In 2008 Ma and Yan reported the application to 3D models. In their study they develop several new numerical techniques to cope with the difficulties of a 3D model, among which a technique to move the mesh near the body surface. Using the

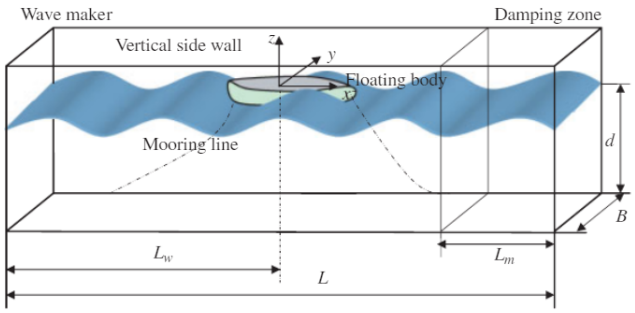

Figure 2.7: Sketch of fluid domain used by Ma and Yan [13]

model, several different floating bodies are simulated with up to 6 degrees of freedom. Ma and Yan adopt the fully non-linear potential flow theory in their work as well as full coupling between waves and floating body. In the formulation of the fully non-linear potential flow theory the velocity potential satisfies the Laplace equation expressed in equation 2.1.

$$\Delta^2\phi = 0 \tag{2.1}$$

In figure 2.7 a sketch is given of the fluid domain used by Ma and Yan. They validated their work using experimental results from other different studies, as well as validating it by a convergence study. Furthermore, they tested several different cases, among which a single body over a flat seabed, a single body near a bump in the seabed and several cases with 2 bodies. All these different investigations are carried out using a numerical tank with a floating body. Figure 2.8 shows an illustration of the initial mesh near the floating body. Because they developed a new technique to move the mesh near the body, this mesh will change during the simulation according to the scheme that can be seen in figure 2.9 [13].

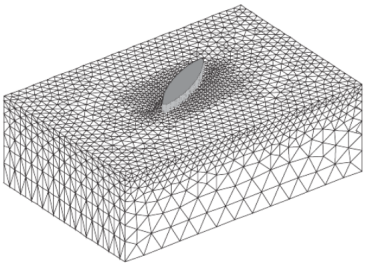

Figure 2.8: Illustration of initial mesh used by Ma and Yan[13]

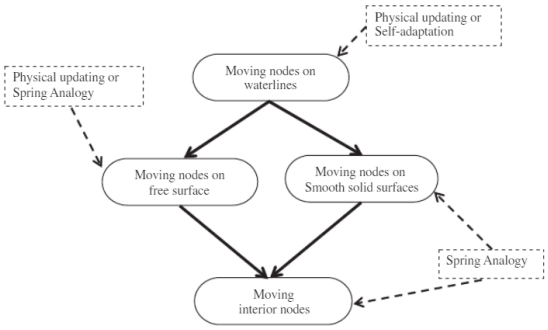

Figure 2.9: Methodology for moving mesh as used by Ma and Yan[13]

In the end Ma and Yan conclude that the natural frequencies and incident angles have a large influence on the transient behaviour of floating bodies. Furthermore, the waves can become short-crested due to a large bump on the seabed even if the initial wave was long crested. As a last conclusion they state that the interaction between multiple vessels should be investigated using fully non-linear methods. The main aspect of the study from Ma and Yan is showing the technique on how to deal with 3D non-linear wave body interactions. The numerical tool is validated by comparing the numerical predictions with experimental data [13].

2.2.3 Conclusion

From the literature it can be concluded that there are multiple suitable ways to model the different structures. Some model the structure analytically, others use a numerical approach to model the structure and its environment. There are multiple methods used to model numerically, such methods include using potential flow theory to calculate the pressure and forces on the structure and the movement of the structure. Potential flow methods that are widely used are the Boundary Element Method (BEM) and Finite Element Method (FEM). Others use more computationally extensive numerical models such as Computation Fluid Dynamics (CFD). In section 3.1 the computational methods are further elaborated. From the literature it can concluded that a potential flow method is a widely used and suitable method to model wave-structure interaction for floating structures without being to computationally extensive.

2.3 Environmental Conditions

The different concept choices and their respective motions and connection forces will be investigated for the Dutch offshore waters. As said earlier, for the Dutch offshore waters of wind energy park Hollandse Kust Noord. So each of the concepts will be evaluated for the wind and wave conditions occuring at that site. In this chapter the wave and wind conditions that are occuring in Hollandse Kust Noord will be discussed shortly.

2.3.1 Wind

From April 2017 till April 2019 Fugro and Deltares have done a field measurement campaign at the site of Hollandse Kust Noord. They have measured both wave heights and wave periods as well as wind speeds for both swell and wind generated waves. For Hollandse Kust Noord they have created scatter diagram for the wind speeds occuring at Hollandse Kust Noord for several direction bins as can be seen in figure 2.10 [14].

	338-23	23-68	68-113	113-158	158-203	203-248	248-293	293-338	
>32.6								0.00	0.00
28.4-32.6						0.00	0.03	0.01	0.04
24.4-28.4					0.02	0.05	0.07	0.01	0.14
20.7-24.4	0.03		0.06	0.00	0.29	0.44	0.35	0.16	1.33
17.1-20.7	0.25	0.01	0.35	0.04	0.87	1.71	1.22	0.49	4.94
13.8-17.1	0.78	0.38	0.60	0.36	1.65	3.41	2.84	1.59	11.62
10.7-13.8	1.53	1.46	1.83	0.77	2.21	5.55	4.14	2.51	20.00
7.9-10.7	2.46	1.73	2.43	1.48	2.55	5.23	4.40	2.87	23.16
5.4-7.9	2.78	2.03	2.06	1.51	2.03	3.34	3.16	2.42	19.32
3.3-5.4	2.03	1.45	0.94	1.07	1.20	1.72	1.85	1.89	12.15
1.5-3.3	0.98	0.96	0.59	0.57	0.67	0.80	0.80	0.81	6.18
0.0-1.5	0.16	0.17	0.12	0.09	0.12	0.14	0.13	0.19	1.12
	11.01	8.19	8.97	5.91	11.61	22.39	18.97	12.95	100.00
HKN Dir (° N) versus U_{100} (m/s)									Total

Figure 2.10: Wind speed and direction occurrence scatter table at a height of 100m [14]

In the figure it can be seen that the highest occurrence, 86,25 %, of wind speeds is between 3.3 $\mathrm{m\,s^{-1}}$ and 17.1 $\mathrm{m\,s^{-1}}$ at a height of 100m above sea level. The wind speed variation with height is calculated by fitting a power profile of the form:

$$U_z = U_{30}(\frac{z}{4})^{\alpha} \qquad [\mathrm{m/s}] \quad (2.2)$$

with U_{30} the wind speed at 30m above the surface and α the power-law constant. However, in the report it is mentioned that there is a large spread in the estimates of alpha and in the profiles. In figure 2.11 it can be seen that there is a large variety in the wind profiles observed and therefore there is also a large variety in α estimates [14]. The mean power profile of $\alpha = 0.11$ is suitable for this research.

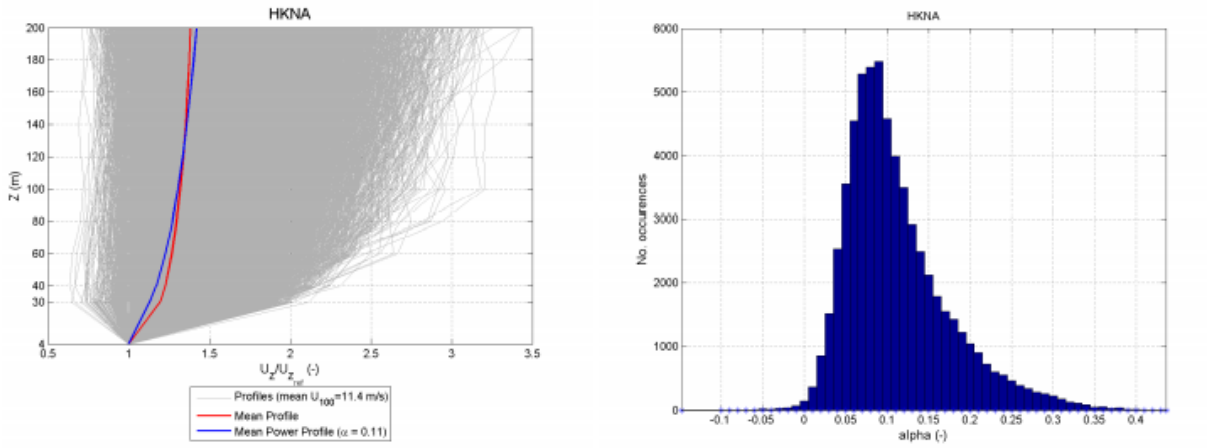

Figure 2.11: Left: observed wind profiles. Right: Historgram of α estimates [14]

2.3.2 Waves

As mentioned in the previous subsection, Deltares and Fugro have also measured wave data at Hollandse Kust Noord. In figure 2.12 the waveheight vs. peak wave period is put into a table with their respective percentage of occurrence. As can be seen, most of the waveheights occurring at Hollandse Kust Noord is below 3m [15].

Hs (m) \ Tp (s)	0-2	2-4	4-6	6-8	8-10	10-12	12-14	>14	
>4.5				0.01	0.26	0.16	0.05	0.01	0.49
4.0-4.5				0.04	0.44	0.09	0.02	0.00	0.59
3.5-4.0				0.24	0.83	0.13	0.01	0.01	1.21
3.0-3.5			0.00	1.18	1.15	0.16	0.01	0.03	2.53
2.5-3.0			0.13	3.44	1.06	0.13	0.01	0.04	4.81
2.0-2.5			1.00	5.92	0.91	0.13	0.02	0.01	7.99
1.5-2.0		0.00	4.48	7.88	1.29	0.16	0.03	0.01	13.85
1.0-1.5		0.57	11.62	7.58	1.29	0.11	0.03	0.00	21.21
0.5-1.0		6.64	15.27	8.46	1.61	0.26	0.03		32.27
0.0-0.5	0.01	5.01	5.23	2.22	2.33	0.21	0.04	0.01	15.06
	0.01	12.23	37.73	36.95	11.17	1.55	0.24	0.12	100.00
HKNA									Total

Figure 2.12: Wavescatter table of waveheight vs. peak wave period at Hollandse Kust Noord [15]

During the campaign, the wave direction is also measured. In figure 2.13 the wave direction roses for the wave height and peak wave period are shown. As can be seen from the figure, most of the waves come from North-West or South-West direction [15].

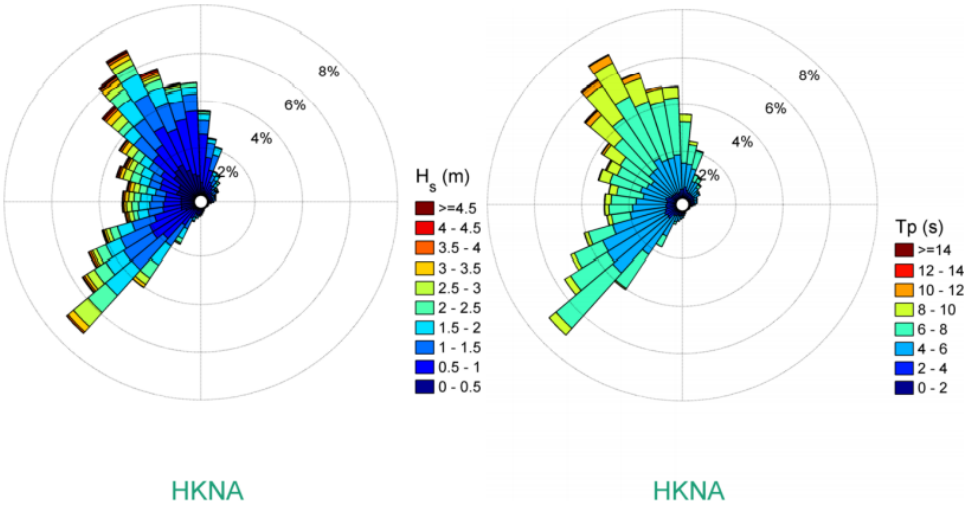

Figure 2.13: Wave direction roses of significant wave height (left) and peak wave period (right) [15]

2.4 Wind Loads

The last important modelling aspect is modelling the wind forces acting on the structure. When using a concept such as oceans of energy [3] or as SUNdy [4], the wind loads on the structure will be rather small. However, when using concepts like the Moss-maritime [5] or SolarDuck [8] the wind loads will be significantly larger and will have to be taken into account. There are multiple ways to incorporate the wind loads. As can be seen in section 2.2, Lee et al. used CFD software to calculate the wind loads on the structure.

A much faster way to calculate the wind loads on a structure is to use an analytical method. Ikhennicheu et al. [38] proposed an analytical method to calculate the wind loads (and wave and current loads) for three different applications of floating solar. Application in a small lake, a large lake and offshore. For the offshore application they used sea states and wind conditions as can be found in the Mediterranean sea. These are relatively calm waters. To calculate the wind loads they used the 3 seconds average wind gust speed. Furthermore they assume that the wind and waves are always aligned for every direction. They used the formula as described in DNVGL-RP-C205 to calculate the wind load.[39]

$$F_{wind} = \frac{1}{2}\rho V^2 A C_d C_s \qquad \text{[N]} \quad (2.3)$$

with ρ the fluid density, V the flow velocity, A the area exposed to the wind and C_d and C_s the drag coefficient and sheltering coefficient respectively. These last two depend on the shape and surface roughness of the structure and the Reynolds number.

Chapter 3 Methodology

In this chapter the modelling method that will be used in the rest of the thesis will be elaborated. This modelling method is chosen in order to answer the research questions as stated in section 1.4. This chapter goes into further detail on the modelling choices and the reasoning behind it.

3.1 General Computational Model

First the hydrodynamical model will be selected and discussed in section 3.1.1. In section 3.1.2 the calculation domain will be discussed. In section 3.1.4 the structural model will be discussed. Section 3.1.5 elaborates the dynamical behavior using the equation of motion. In section 3.1.6 the modelling of the wavespectrum will be elaborated after which the full modelling approach of this work is summarized in section 3.1.7.

3.1.1 Hydrodynamical model

There are multiple ways to model the forces of a floating body in water. Feys used the Morison equation to calculate the drag and inertial forces [12]. Dombre et al. used a more extensive method to calculate loads and motions on the structure using potential theory [36]. Another common way to model the structural dynamics has been done by Lee et al.. Lee et al. used ANSYS AQWA software to make a CFD model based on the Reynolds averaged Navier-Stokes equation[10]. The advantages and disadvantages of each of the modelling choices will be discussed, after which a suitable modelling approach for this work is selected.

First of all, the Morison equation is the fastest and easiest way to calculate the forces on the structure. However, the Morison equation approach is only valid for slender bodies compared to the wavelengths of the waves acting on the body. As can be seen in figure 3.1. As in this research there will be different sizes of structures and mostly structures not slender compared to the wavelength, this is not a suitable modelling approach.

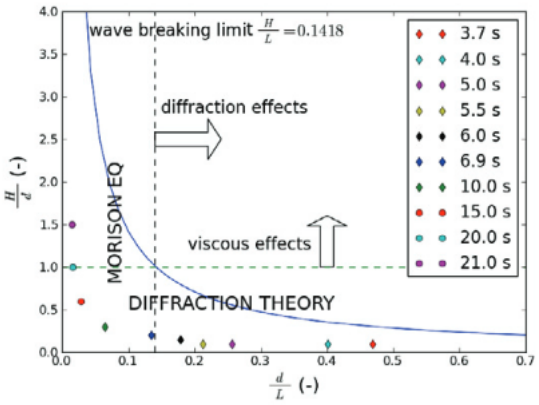

Figure 3.1: Potential theory and Morison equation validity regions for fixed bodies [16]

Then potential flow theory and CFD remain. Both with their respective advantages and disadvantages. First the advantages, disadvantages and assumptions of the potential flow theory will be discussed after which the same will be discussed for CFD.

Potential flow

The most commonly used potential flow model is the Boundary element method (BEM). The potential flow methods make use of the following assumptions [40]:

- Inviscid fluid
- Irrotational flow. The velocity can be derived everywhere in the fluid domain: $\overrightarrow{V}(M,t) = \overrightarrow{\nabla}\phi(M,t)$ because there exits a velocity potential $\phi(M,t)$.

- Incompressible flow. This assumptions gives the Laplace equation because of mass conservation: $\Delta\phi(M,t) = 0$

Using these assumptions, a set of boundary conditions can be formulated that satisfy the Laplace equation. This results in a non-linear boundary value problem. Usually the problem is simplified further by being linearised. There are two additional assumptions that come with linearisation [40]:

- The wave height to wavelength ratio (wave steepness) and wave height to water depth ratio are both much smaller than 1.

- The ratio of the typical amplitude of motion to the typical dimension of the body has to be much smaller than 1. i.e. the motion of the body are small.

The linearized boundary value problem is then discretised and solved numerically in the frequency domain [40].

Because of the linearity assumptions, the potential flow method shows significant discrepancies with experiments for larger sea states (rougher seas). In this case a CFD method will be more accurate. However, CFD models require usually a much larger computational time compared to a potential flow method such as the BEM. However, when the number of unknowns in a BEM model increase, the computational time increases proportionally with the square of the unknowns [40].

BEM models are widely used in all different kinds of research. Especially in contact problems, because no interior elements are needed when using a BEM method. This reduces the dimension of the problem significantly and therefore the computational time. Furthermore, the BEM automatically satisfies the boundary conditions for infinite and semi-infinite domains. The BEM is used for a large number of applications. Such applications include, but are not limited to, the modelling of wing structures of an aircraft, the modelling of a bone structure or for a crack growth simulation [41].

CFD models

Computational fluid dynamics (CFD) models are seeking to resolve the Navier-stokes equations. In the Navier-Stokes equations both the viscous effects as well as turbulence are present. CFD is much more suitable in cases of extreme wave loading and breaking waves compared to potential flow models. Furthermore, the non-linear hydrodynamics are fully retained when using a CFD approach. Together with the disadvantage of being computationally highly intensive, CFD models are prone to internal dissipation [40].

In this study the main goal is to obtain and compare the forces within the offshore floating solar structure. For this purpose, the hydrodynamical model has to be accurate enough to obtain the excitation forces on the structure with reasonable accuracy. Thus the radiation and diffraction has to be taken into account. So a potential flow model or CFD model would be applicable for the problem. However, for this purpose a CFD model will be computationally too extensive and this level of accuracy is not needed. Therefore in this study a potential flow model will be used as this gives accurate results that match the real world well without too much computational effort. More specifically, a boundary element method (BEM) model will be used.

3.1.2 Domain

When using a potential flow theory model there are two possibilities for the domain in which the motion and forces can be computed:

- Time domain (TD)
- Frequency domain (FD)

The time domain potential flow models use the same assumptions for small wave steepness and small body motions as frequency domain models. However it is possible to include nonlinear external forces in the time domain simulation such as viscous damping and mooring. Frequency domain potential flow models can not cope with the non-linear terms. However, time domain computations require higher computational effort than frequency domain calculations [40].

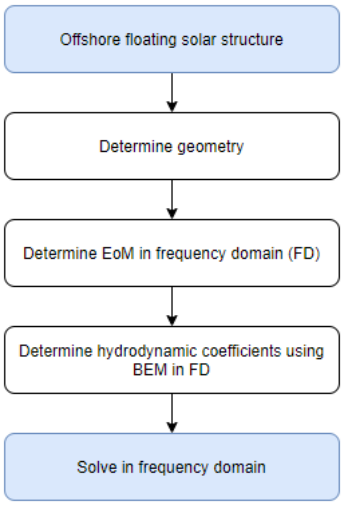

Figure 3.2: Overview model approach frequency domain BEM

In this study, a initial comparison is made between the forces on the structure for different structure configurations. Therefore a time domain model including non-linearities is not necessary for the initial comparison of the forces within the structure. The most suitable and quickest method will be a frequency domain boundary element method as this gives suitable accurate results without requiring high computational time. An overview of the modelling approach for this time domain model can be seen in figure 3.2

3.1.3 Software

The software that will be used to calculate the hydrodynamic coefficients, such as added mass, radiation damping and diffraction forces, is the open source boundary element software NEMOH. In this study NEMOH software is used because it is open source. NEMOH has been developed by Ecole Centrale de Nantes. It consists of three programs. A pre-processor where the mesh and initial conditions are set, a solver, that calculates the pressure field, hydrodynamic coefficients, far field coefficients and wave elevation and a post-processor, that can be used the calculate RAOs and plot the free surface wave elevation. It also includes meshing tools to create the mesh around the structure [42]. A mesh is needed to discretize the calculation domain in a number of panels for which the radiation potential ϕ_r, the undisturbed wave potential ϕ_0 and the diffraction potential ϕ_7 can be obtained. In figure 3.3 the mesh created by NEMOH for a simple rectangular barge is shown. In the figure, only half the structure is shown as the structure is symmetrical accros the X axis, this is done to reduce the computational time. Using the potential flow theory the software can calculate the added mass, hydrodynamic damping and wave excitation force and phase shift with respect to the incoming wave.

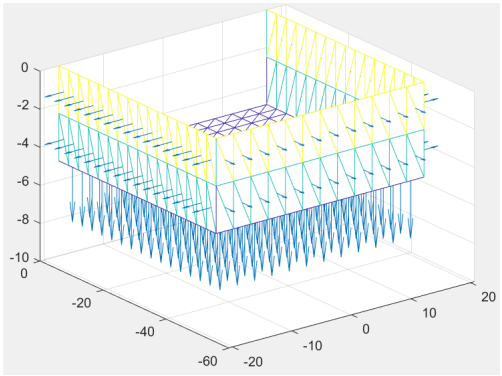

Figure 3.3: Example of the mesh created by NEMOH with about 300 panels

Added mass and damping

This section describes in short how the added mass and damping is obtained. It is based on the theory described by Journée and Massie [43].

The total potential can be described as:

$$\Phi = \sum_{j=1}^{6} \Phi_{r,j} + \Phi_0 + \Phi_7 \qquad [-] \quad (3.1)$$

with $\Phi_{r,j}$ the radiation potential, Φ_0 the undisturbed wave potential and Φ_7 the diffraction potential.

The radiation potential Φ_r can be written in terms of $\phi_{r,j}$ for all 6 degrees of freedom as:

$$\Phi_r(x, y, z, t) = \sum_{j=1}^{6} \phi_{r,j}(x, y, z) v_j(t) \qquad [-] \quad (3.2)$$

The space and time dependent potential term is now separated in a space dependent term $\phi_{r,j}$ multiplied by a velocity v_j. The normal velocity on the surface of the body can now be written as:

$$\frac{\partial \Phi_r}{\partial n} = \sum_{j=1}^{6} \frac{\partial \phi_{r,j}}{\partial n} v_j \qquad [-] \quad (3.3)$$

Using this the radiation forces and moments on the structure can be calculated by calculating the radiation pressure integrated over the body surface.

$$\overrightarrow{F_r} = \rho \iint_S \left(\frac{\partial}{\partial n} \sum_{j=1}^{6} \phi_{r,j} v_j \right) \overrightarrow{n} dS \quad (3.4)$$

$$\overrightarrow{M_r} = \rho \iint_S \left(\frac{\partial}{\partial n} \sum_{j=1}^{6} \phi_{r,j} v_j \right) (\overrightarrow{r} \times \overrightarrow{n}) dS \quad (3.5)$$

The force and moment vector can be also written in a part relative to the velocity and relative to the acceleration. For the force in DOF j on panel i this becomes:

$$F_{r,i,j} = -a_{i,j} \Re[(-i\omega)^2 \hat{u_j} e^{i\omega t}] - b_{i,j} \Re[(-i\omega) \hat{u_j} e^{i\omega t}] \quad (3.6)$$

By setting equation 3.4 and 3.6 equal to eachother and eliminating the time dependent part, added mass and damping coefficients can be found as:

$$a_{i,j} = \Re\left[\iint_S \rho\phi_{r,j} n_i dS\right] \tag{3.7}$$

$$b_{i,j} = \Im\left[\iint_S \rho\phi_{r,j}\omega n_i dS\right] \tag{3.8}$$

3.1.4 Structural model

In this section, the considered system is discussed as well as the modelling approach to model the structure.

Geometry structure

An overview of the structural geometrie used for this study is given in figure 3.4, with rectangular floaters with 2 connections at the edges. One rectangular floater has a length L, width B, height H and a draft T. The center of gravity is located at a distance l from the short side and a distance b from the left side. The local axis system for each floater is located in the center of gravity. The connections between the floaters are modelled as a set of three linear translational springs and three linear rotational springs with spring stiffness k. Waves traveling in the positive x direction are denoted as $\mu = 0°$ (Beam waves) incoming wave angle. The rectangular floaters will be analysed as rigid structure. The stiffness of the springs will be varied in different directions to investigate the influence of connection compliance on the forces within the connections. Furthermore, the dimensions of the floater will be varied. As mentioned earlier, due to time constraints, the flexibility of the floater will not be analysed further in this research.

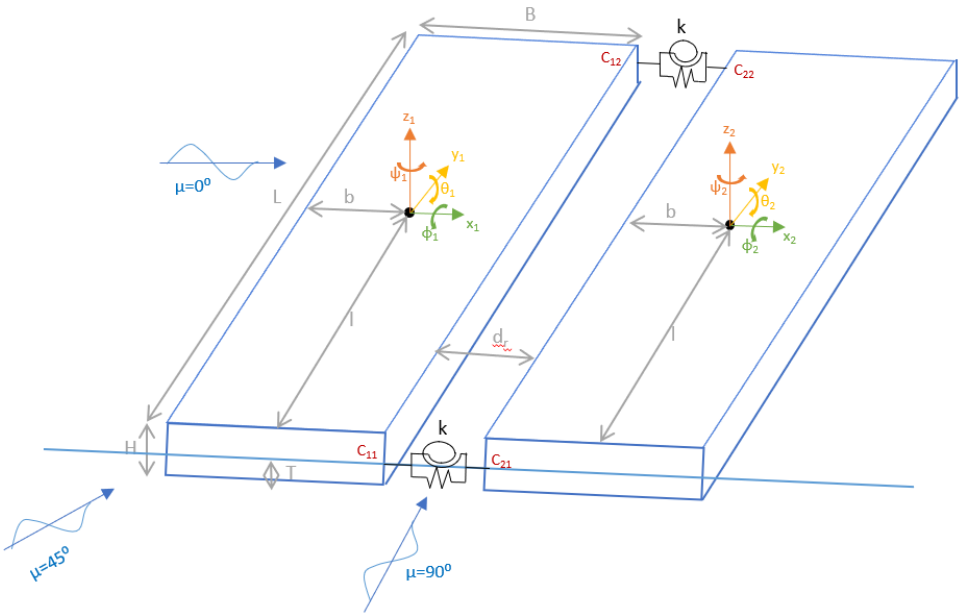

Figure 3.4: Overview of geometry of the structure using rectangular floaters with 2 connections at the edges

The motion of the structure will be described with respect to the center of gravity. Rotational motions are denoted using ϕ, θ and ψ. Translational motions are denoted using x, y and z. To separate motions of the individual floaters the subscripts 1 and 2 are used for the first and second floater respectively. The convention for the models motions are summarized in table 3.1.

Table 3.1: convention for the motions of the structure

Motion	sign
Surge	x
Sway	y
Heave	z
Roll	ϕ
Pitch	θ
Yaw	ψ

Using the equation of motion and the calculated hydrodynamical, hydrostatic and mechanical coefficients the motion response of the structure can be computed. From the motion and forces on the structure the internal forces in the structure can be computed.

3.1.5 Equations of motion

In order to obtain the motion response of the structure, the equations of motion of the structure has to be derived. In this section the equation of motion of a single rigid body is derived after which this is extended to multiple bodies that are connected using the combination of springs in all degrees of freedom.

Single body in water

The equation of motion of a single body around it's center of gravity (COG) in water can be derived from Newton's second law. The equations for translations of and the rotations about the centre of gravity are given by [43]:

$$\overrightarrow{F} = \frac{d}{dt}(m\overrightarrow{U}) \qquad and \qquad \overrightarrow{M} = \frac{d}{dt}(\overrightarrow{H}) \qquad [\text{-}] \quad (3.9)$$

with:

- $\overrightarrow{F}$ = external force acting in the centre of gravity (N)
- m = mass of the rigid body (kg)
- $\overrightarrow{U}$ = Instantaneous velocity of the centre of gravity (m/s)
- $\overrightarrow{M}$ = External moment acting about the centre of gravity (nM)
- $\overrightarrow{H}$ = Instantaneous angular momentum about the centre of gravity (Nms)
- t = time (s)

The total mass is considered constant as well as the mass distribution over the body.

Since the system is linear, the resulting motion can be seen as a superposition of the motion of the body in still water and the forces on a restrained body in waves [43]. This results in

the hydromechanical forces and moments that are induced by the harmonic oscillations of the body moving in still water and the wave exciting forces and moments produced by waves on the restrained body [43].

The hydromechanical forces that are induced by the harmonic oscillations in water can be separated in a hydrostatic part and a hydrodynamic part. The hydrostatic part is the force acting on a displaced body and can be written as:

$$\widetilde{F}_{static} = -c\widetilde{u}(\omega) \qquad \text{[N]} \quad (3.10)$$

with c the hydrostatic stiffness matrix that results from the buoyancy of the body and $\widetilde{u}$ the displacement of the body. For a six DOF motion the hydrostatic stiffness matrix will be a (6x6) matrix that can be written as:

$$C = \begin{bmatrix} 0 & & & & & \\ & 0 & & & & \\ & & c_{33} & & & \\ & & & c_{44} & & \\ & & & & c_{55} & \\ & & & & & 0 \end{bmatrix} \qquad \text{[-]} \quad (3.11)$$

For a vertical walled structure that is symmetrical in x and y axis the stiffness components only act in the heave, roll and pitch motion.

The hydrodynamic force is a result of the body motion in water also known as the radiation force. As can be seen in equation 3.6 this force can be written as:

$$\widetilde{F}_{dyn} = \omega^2 a\widetilde{u} - i\omega b\widetilde{u} \qquad \text{[N]} \quad (3.12)$$

with a the added mass, ω the excitation frequency, $\widetilde{u}$ the body motion and b the hydrodynamic damping coefficient.

For a 6 DOF system the added mass and damping matrices will result in a (6x6) matrices for each frequency. The added mass matrix can be written as:

$$A(\omega) = \begin{bmatrix} a_{1,1}(\omega) & \cdots & a_{1,6}(\omega) \\ \vdots & \ddots & \vdots \\ a_{6,1}(\omega) & \cdots & a_{6,6}(\omega) \end{bmatrix} \qquad \text{[-]} \quad (3.13)$$

and the hydrodynamic damping matrix can be written as:

$$B(\omega) = \begin{bmatrix} b_{1,1}(\omega) & \cdots & b_{1,6}(\omega) \\ \vdots & \ddots & \vdots \\ b_{6,1}(\omega) & \cdots & b_{6,6}(\omega) \end{bmatrix} \qquad \text{[-]} \quad (3.14)$$

The wave exciting forces and moments produced by waves on the restrained body can also be split into two parts. The Froude-Krilov force and a diffraction force.

$$\widetilde{F}_w = \widetilde{F}_{FK} + \widetilde{F}_d \qquad \text{[N]} \quad (3.15)$$

The Froude-Krilov force is the force resulting from the pressure of the waves acting on the body's surface. The force can be calculated by integrating the hydrodynamic pressure over the body's surface. A part of the wave will be diffracted by the body, therefore the Froude-Krilov force requires a correction, the diffraction force.

This results in the following equation of motion for multiple DOFs for a single body floating in water in the frequency domain for a frequency ω:

$$\widetilde{u}(\omega)(-\omega^2(M + A(\omega)) + i\omega B(\omega) + C) = \widetilde{F}_w(\omega) \qquad \text{[N]} \quad (3.16)$$

with

- $\widetilde{u}$ = Complex motion vector
- M = Mass matrix
- A = added mass matrix
- B = hydrodynamic damping matrix
- C = stiffness matrix
- $\widetilde{F}_w$ = complex wave exciting force and moment vector.

The complex motion vector $\widetilde{u}$ will be written as

$$\widetilde{u}(\omega) = \begin{bmatrix} \widetilde{x} & \widetilde{y} & \widetilde{z} & \widetilde{\phi} & \widetilde{\theta} & \widetilde{\psi} \end{bmatrix}^T \qquad \text{[-]} \quad (3.17)$$

Two bodies with connections

The above equation of motion for a single body can be extended to a system of 2 bodies as described in section 3.1.4. This extension of the equation of motion is similar as the study by Sun and Choo [44]. The joint connection of the bodies will be introduced in the equation of motion as a joint stiffness matrix. Thus equation 3.16 will be adjusted to:

$$\widetilde{u}(\omega)(-\omega^2(M + A(\omega)) + i\omega B(\omega) + C + K_{joint}) = \widetilde{F}_w(\omega) \qquad \text{[N]} \quad (3.18)$$

with

- $\widetilde{u}$ = Complex motion vector
- M = Mass matrix
- A = added mass matrix (12x12)

- B = hydrodynamic damping matrix (12x12)
- C = stiffness matrix (12x12)
- $\widetilde{F}_w$ = complex wave exciting force and moment vector.
- K_{joint} = joint stiffness matrix (12x12)

The joint stiffness matrix K_{joint} describes the forces in the joints in a linear way as follows:

$$F_{joint}(u(t)) = -K_{joint}u(t) \tag{3.19}$$

The joint stiffness matrix for a two body system is a 12x12 matrix that relates the motion of the floater to the joint forces with respect to the centers of gravity of the two floaters. The joint is modelled as a set of linear springs and rotational springs in all 6 degrees of freedom. The connection stiffness matrix is obtained using the Euler-Lagrange equation by using the potential energy of all the springs. The joint force can then be described by:

$$F_{joint}(u_j) = \frac{-\partial V}{\partial u_j} \tag{3.20}$$

with V the potential energy of the springs and j the degree of freedom. The potential energy of a connection joint can be written as:

$$V = \frac{1}{2}(k_x(\Delta x_c)^2 + k_y(\Delta y_c)^2 + k_z(\Delta z_c)^2 + k_\phi(\Delta \phi_c)^2 + k_\theta(\Delta \theta_c)^2 + k_\psi(\Delta \psi_c)^2) \tag{3.21}$$

with k the joint stiffness in each degree of freedom. The subtext c denotes the connection point.

As can be seen in equation 3.21 the potential energy is dependent on the relative distance and rotations of each of the connection points. A single joint is connected to barge 1 on location c_1 from the COG of barge 1 and to barge 2 on location c_2 from the COG of barge 2. c_1 and c_2 can be written as:

$$c_1 = \begin{bmatrix} c_{1,x} & c_{1,y} & c_{1,z} & \phi & \theta & \psi \end{bmatrix}^T \tag{3.22}$$

$$c_2 = \begin{bmatrix} c_{2,x} & c_{2,y} & c_{2,z} & \phi & \theta & \psi \end{bmatrix}^T \tag{3.23}$$

The relative displacement can then be written as:

$$u_{joint} = c_1 - c_2 \tag{3.24}$$

with:

$$u_{joint} = \begin{bmatrix} \Delta x_c & \Delta y_c & \Delta z_c & \Delta \phi_c & \Delta \theta_c & \Delta \psi_c \end{bmatrix}^T \tag{3.25}$$

The resulting force in the joint F_{joint} is now a function of the displacement vector of the joint u_{joint} and the stiffness vector k. Using this, the spring stiffness matrix can be calculated and must be linearized in order to be applied in the frequency domain.

This procedure can be repeated in order to account for multiple connections between the 2 barges.

Multiple bodies with connections

The above procedure of extending the single body system to a 2 body system that is connected can be extended in order to account for more than 2 bodies. In the case of multiple bodies the matrices and vectors will become larger as the number of bodies increases. Furthermore, the joint stiffness matrix will also become larger and more extensive. When calculating multiple bodies the computational time will increase significantly as a more complex system of equations has to be solved. In this thesis, first a model consisting of two bodies connected will be analysed. In a later stage this can be extended to more bodies connected to each other.

Flexible floating bodies

To obtain the equation of motion of a flexible floating body another approach has to be used. The flexible floating body can be modelled using a finite element method (FEM). The finite element method creates a mesh of the structural model. Using this mesh the dry flexible mode shapes can be calculated. These mode shapes can then be used to calculate the structural response of the system.

Because of time constraints, this part is left out of this research. The influence of flexibility of the floater should be further investigated in later research.

3.1.6 Wave model

Ocean waves can be modelled by superposition of regular waves as can be seen in figure 3.5. This can be modelled by a wave spectrum. In section 2.3.2 the wave climate is shortly discussed. In this research a JONSWAP-spectrum will be used to model the waves. The JONSWAP spectrum is most representative of the waves occuring at the North Sea [17]. The JONSWAP spectrum describes the waves using the significant wave height (H_s) and peak period (T_p) in following form:

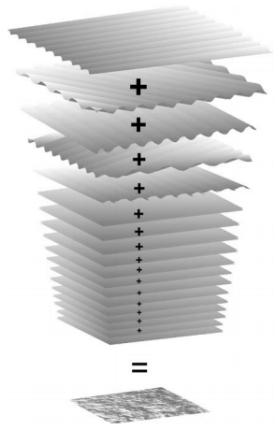

Figure 3.5: Sum of large number of harmonic wave components differing in period, directions, amplitudes and phases [17]

$$S_j(\omega) = A_\gamma S_{PM}(\omega)\gamma^{exp\left(-0.5\left(\frac{\omega-\omega_p}{\sigma\omega_p}\right)^2\right)} \quad [-] \quad (3.26)$$

with $S_{PM}(\omega)$ being the Pierson-Moskowitz spectrum:

$$S_{PM}(\omega) = \frac{5}{16}H_s^2\omega_p^4\omega^{-5}exp\left(-\frac{5}{4}\left(\frac{\omega}{\omega_p}\right)^4\right) \quad [-] \quad (3.27)$$

and γ the non dimensional peak shape parameter, σ the spectral width parameter, $\sigma = \sigma_a$ for $\omega \leq \omega_p$ and $\sigma = \sigma_b$ for $\omega > \omega_p$, $A_\gamma = 1 - 0.287\ln(\gamma)$ and $\omega_p = \frac{2\pi}{T_p}$. This JONSWAP function together with the wave data from section 2.3.2 give the wave spectrum.

From the wavescatter from section 2.3.2, the design significant wave height and period can be computed. For this thesis the Ultimate Limit State (ULS) significant wave height will be used. This is done to compare the difference in forces for for different sizes and flexibilities more easily. The ULS wave is defined as the wave with a return period of 50 years. This leads the following values for the significant wave height and peak wave period for the location Hollandse Kust Noord in the Dutch offshore water [45]:

- $H_s = 7.3m$
- $T_p = 11.5s$

For average values for JONSWAP experiment data of $\gamma = 3.3$, $\sigma_a = 0.07$ and $\sigma_b = 0.09$ [39] this leads to the spectrum as can be seen in figure 3.6:

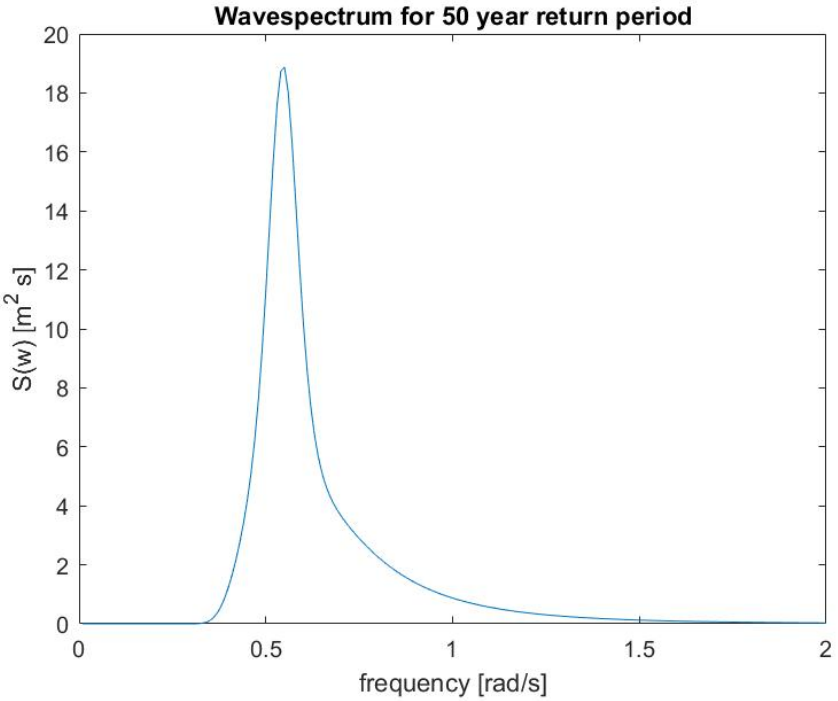

Figure 3.6: The used JONSWAP spectrum for $H_s = 7.3$ and $T_p = 11.5s$

3.1.7 Full model

In figure 3.7 the full model approach overview is shown. As input parameters the wavedata and geometry of the structure is needed. The available wavedata together with the wavemodel give a frequency domain wave spectrum. From the geometry a structural model is made. From this model a mesh can be made that can be included in the hydrodynamical model. The structural model also determines the mechanical coefficients for the equation of motion. From the hydrodynamical model the hydrodynamic and hydrostatic coefficients can be computed as well as the wave force response function, which expresses the wave force as function of the amplitude of the wave. All these coefficients can then be used to calculate the full equation of motion and together with the wavespectrum the motion response and internal forces within the structure can be computed.

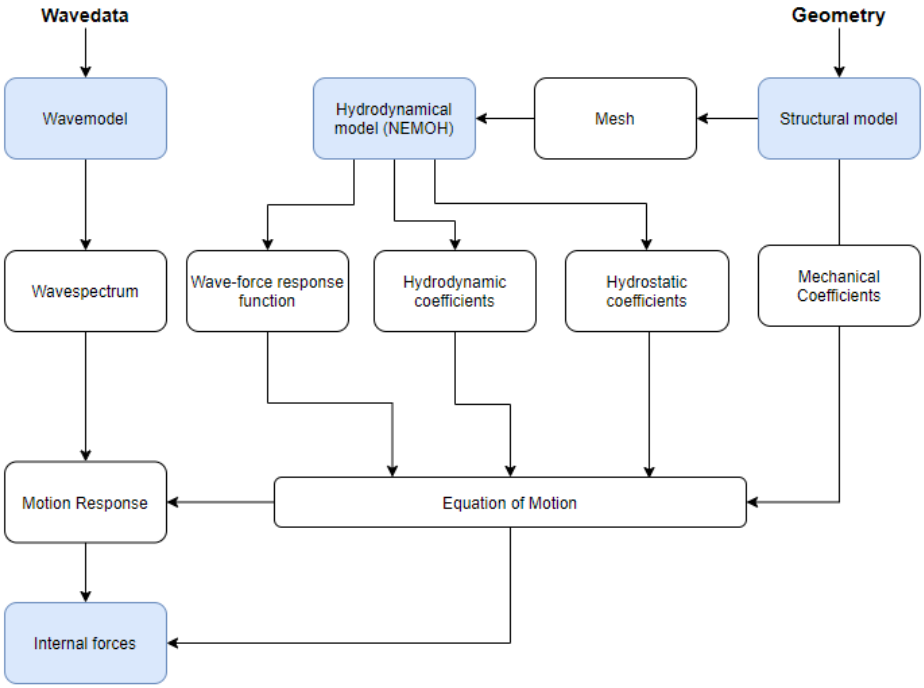

Figure 3.7: Overview of frequency domain modelling approach

3.1.8 Model validation

In order to determine if the created model is correct, validation is needed. The model will be validated using data from an earlier study done by Sun, Eatock and Taylor from 2010 [18]. In the research they study the wave diffraction for two parallel rectangular barges. A comparison is done between the floater forces for two rectangular barges next to each other and a single floating barge. This study will be used to verify the calculated hydrodynamic coefficients, wave excitation forces and the resulting calculated motions of the floater.

The model with connections will be assessed using results from an earlier study done by Sun et al.[44] and Newmann[46]. In these studies the motion response of hinged barges is examined as well as barges with a rigid connection. These results can be used to validate the rigid body motion of the connected floater resulting from the model by implementing the same structural properties and dimensions as done by Newmann and Sun et al.. The results are described in chapter 5.

Chapter 4 The Model

In this chapter the rigid body model will be further elaborated. First the boundary element method and usage of NEMOH will be elaborated. After which the further build up of the model is explained.

4.1 BEM Software

In order to calculate the motions and forces on the floating structure, the hydrodynamic coefficients and forces on the structure have to be obtained. This is done using the boundary element method as explained in section 3.1.1. More of the theory and assumptions behind BEM solvers will be explained in this section. Furthermore, it will go further into the used BEM software NEMOH.

4.1.1 Boundary Element Method

To solve the equation of motion from equation 3.18, the added mass matrix A and hydrodynamic damping matrix B have to be obtained. This is achieved using the boundary element method. As described in section 3.1.1, the boundary element method uses a potential flow model to calculate the added mass and hydrodynamic damping. The formulas for calculating the added mass and damping using the potential is also explained earlier in section 3.1.3. To get the full added mass and damping matrix, this method is performed for each degree of freedom for each of the 2 bodies. Therefore, the added mass and hydrodynamic damping matrix becomes a 12x12 matrix, with the 6 degrees of freedom for each body in the top left and bottom right part of the matrix and the coupling between bodies described on the bottom left and top right part of the matrix.

Equations 3.7 and 3.8 are then solved numerically by dividing the structure into small elements at the boundary of the structure, the mesh. The equations are solved for each element of the mesh and for each wave frequency. This gives an added mass and damping matrix for each wave frequency, which can be used to solve the equation of motion of the structure.

To solve the velocity potential for each panel, equation 4.1 is used. The velocity potential is calculated using the source technique. A source is a point from which fluid flows out uniformly in all directions. The theory for using the source technique for solving the potential is explained more extensively by Faltinsen, 1990[47]. When using a mesh, each panel is assumed to have its own source, usually chosen at the center of each panel. The potential on that panel is then calculated using the Green function that describes the flow at that location due to a source of unit strength and the source strength. This results in equation 4.1 for the structure.

$$\phi(\overrightarrow{x}) = \frac{1}{4\pi} \int_{S_b} G(\overrightarrow{x}, \overrightarrow{x}_s)\sigma(\overrightarrow{x}_s)dS \qquad [-] \quad (4.1)$$

with:

- $\overrightarrow{x}$ is the source location on the surface of the structure.
- S_b is the mean wetted surface
- $G(\overrightarrow{x}, \overrightarrow{x}_s)$ is the Green function

- $\sigma(\overrightarrow{x}_s)$ is the strength of the source at $\overrightarrow{x}$

The Green function satisfies all the boundary conditions except the normal velocity boundary condition on the surface of the structure, stated as:

$$\frac{\partial\phi(\overrightarrow{x})}{\partial n} = v_n(\overrightarrow{x}) \quad [-] \quad (4.2)$$

with v_n the normal velocity of the flow on the surface of the structure.

The source strength can be solved using the boundary condition by satisfying equation

$$-\frac{1}{2}\phi(\overrightarrow{x}) + \frac{1}{4\pi}\int_{S_b} \frac{G(\overrightarrow{x}, \overrightarrow{x}_s)}{n_{\overrightarrow{x}}}\phi(\overrightarrow{x})dS = v_n(\overrightarrow{x}) \quad [-] \quad (4.3)$$

This equation can then be discretized and solved for each panel of the mesh, resulting in velocity potential for each panel of the mesh.

4.1.2 NEMOH

The previously explained theory can be applied to structures using the open source software NEMOH. NEMOH solves the first order hydrodynamic coefficients in the frequency domain. It has been developed by Ecole Centrale de Nantes for 30 years. It solves the linear boundary value problem (BVP) in the frequency domain. It uses the linear free surface potential flow theory. Green's second identity and the Green function is applied. The linear BVP is solved using a mesh that is created by the user. NEMOH itself consists of 3 parts [42]:

- Preprocessor, Read and prepare the mesh and calculation cases (set of body conditions)
- Solver, For each body condition, solve the linear BVP for the potential and calculate pressure field, hydrodynamic coefficients, far field coefficients and wave elevation
- Postprocessor, Postprocess the results

NEMOH has the following outputs:

- Radiation coefficients (added mass and damping coefficients)
- Excitation force coefficients
- Diffraction force coefficients
- Impulse response force and infinite frequency added mass
- Froude Krilov force

NEMOH also comes with a Matlab wrapper and mesh generation tool to help the user and make it more user friendly. A small overview of the input and output of NEMOH can be found in figure 4.1.

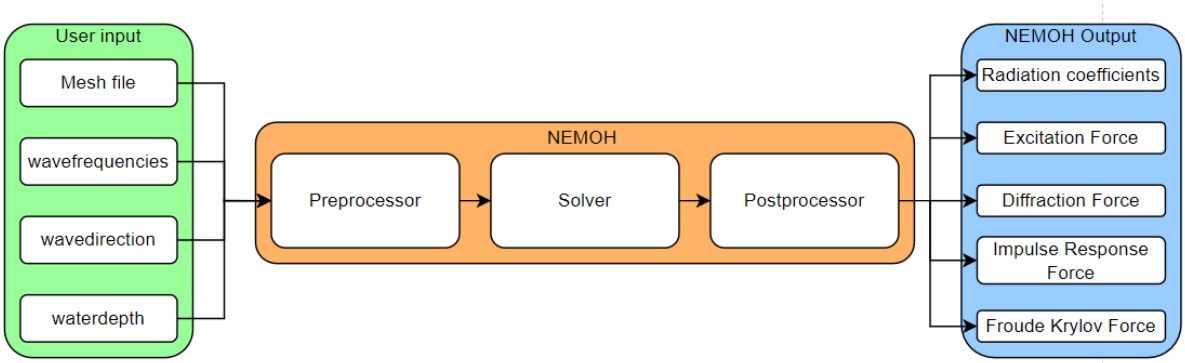

Figure 4.1: Overview of NEMOH input, programms and output.

4.1.3 Number of panels

In order to reduce the computational time but maintain accurate results, the number of panels for each mesh should be picked carefully. The number of panels relates to the wavelengths that are taken into account. For this study wavefrequencies between 0 and $2rad/s$ are used. The wave length corresponds to the wave frequency via the dispersion relation. For a deep water case, as is used in this study, the wavelength corresponds to the frequency using the following formula:

$$\lambda = \frac{2\pi g}{\omega^2} \qquad [\text{m}] \quad (4.4)$$

As a rule of thumb, the number of panels for fluid-structure interactions are at least 6 elements per wavelength to get reasonable accuracy [48]. So the minimal number of panels can be calculated using the wetted surface area as follows:

$$N_{panels} = \frac{A_{wetted}}{(\lambda/6)^2} \qquad [\text{-}] \quad (4.5)$$

For each of the the different sizes that will be tested in the model, this will give a different number of panels. The Mesh tool in NEMOH considers symmetry in the x-axis, so the number of panels used in the mesh is half of the number of panels that is required. The number of panels used for each model are further elaborated in each separate case.

4.1.4 Irregular Frequencies

The used mathematical theory when solved numerically by a computer can result in a complication for some frequencies. This complication is called irregular frequencies. When the Green formula is used to compute the source strength there might be frequencies where a solution may not exist. Faltinsen [47] explains that "for a surface piercing body there exist an infinte number of discrete frequencies (irregular frequencies) that cause the three-dimensional source technique to break down." Irregular frequencies are not a physical phenomenon. As further explained by Faltinsen, irregular frequencies represent eigenfrequencies for a fictitious fluid motion inside the body with the same free-surface condition as outside the body and the body boundary condition $\phi = 0$. Mathematically this means that, for the unknown source densities at the irregular frequency, the determinant of the coefficient matrix goes to zero when the number of unknowns goes to infinity. This causes amplitude peaks in the calculated added mass, damping and force coefficients.

Unfortunately, NEMOH doesn't have a tool to remove the irregular frequencies from the calculation. Thus, these irregular frequencies have to be removed in post processing after running NEMOH to avoid discrepancies in the calculation of internal forces and motion of the structure.

One relatively easy approach to remove irregular frequencies is presented by Inglis and Price [49]. They simply remove the irregular frequencies by interpolating the hydrodynamic coefficients in the affected regions. The affected regions can be identified in the hydrodynamic coefficients. The irregular frequencies are determined by the body geometry. Inglis and Price also give a formula to find the irregular frequencies for a box of length L, width B and draft T. The irregular frequency $\hat{\omega}$ can be found using equation 4.6 [49].

$$\hat{\omega}_{\alpha\beta} = \sqrt{g\gamma \coth \gamma T} \qquad \text{[rad/s]} \quad (4.6)$$

for

$$\gamma^2 = \left(\frac{\alpha\pi}{L}\right)^2 + \left(\frac{\beta\pi}{B}\right)^2 \qquad \begin{matrix} \alpha = 1, 2, 3... \\ \beta = 1, 2, 3... \end{matrix}$$

There are an infinite number of solutions for this equation, however the lowest frequency, $\hat{\omega}_{11}$, is of most importance, because below this frequency, no irregular frequencies occur. In this research, the irregular frequencies are removed using the method from Inglis and Price. First the area where resonant frequencies occur are identified using equation 4.6, after which this part is cut out and interpolated. The interpolation is done using the fitting tool from MATLAB. This is done by using the smoothingspline fitting option on MATLAB and excluding the data in the affected regions. The smoothingspline option from MATLAB uses a smoothing parameter p and specified weight w_i. For this study the best results are obtained using weight 1 for all data points and using the automatically selected smoothing parameter from MATLAB. This is often automatically selected by MATLAB in the 'interesting range' of p near $1/(1 + h^3/6)$ with h the spacing between data points [50]. By using this method, only the data in the range that has to be excluded is not used. Furthermore the fitted data has no sharp edges at the interpolation corners.

As an example, for a set of floaters of length $L = 50m$, width $B = 35m$, draft $T = 5m$ and a gap between the floaters of $d = 3.5m$ the irregular frequencies from table 4.1 are calculated using the formula from Inglis and Price. The irregular frequencies can be found in the calculated hydrodynamic coefficients and calculated forces on the floaters. In figures 4.2 and 4.3 the irregular frequencies are shown as small peaks in the added mass in heave direction of floater 1 and small peaks in the heave force for floater 1 in blue. Furthermore, gap resonance occurring in the gap between the barges is also shown for a frequency between 1 and $1.2rad/s$. The gap resonance is further discussed in the next section, section 4.1.5. As can be seen in the figures, a small peak occurs at a wave frequency of $\omega = 1.47rad/s$, furthermore at $\omega = 1.59$, $\omega = 1.62$, $\omega = 1.75$ and at $\omega = 1.86$. These are some of the frequencies that are also calculated by the equation from Inglis and Price as shown in table 4.1. In figures 4.2 and 4.3 the added mass and damping is also shown after removal of the irregular frequencies by the removal method as described earlier. It can be seen that this removal method gives smooth results that remove the peaks occurring at the irregular frequency intervals.

Table 4.1: Irregular frequencies calculated using equation 4.6 for floater of $50mx35mx5m$

α/β	1	2	3
1	1.468	1.588	1.754
2	1.529	1.640	1.797
3	1.621	1.721	1.864

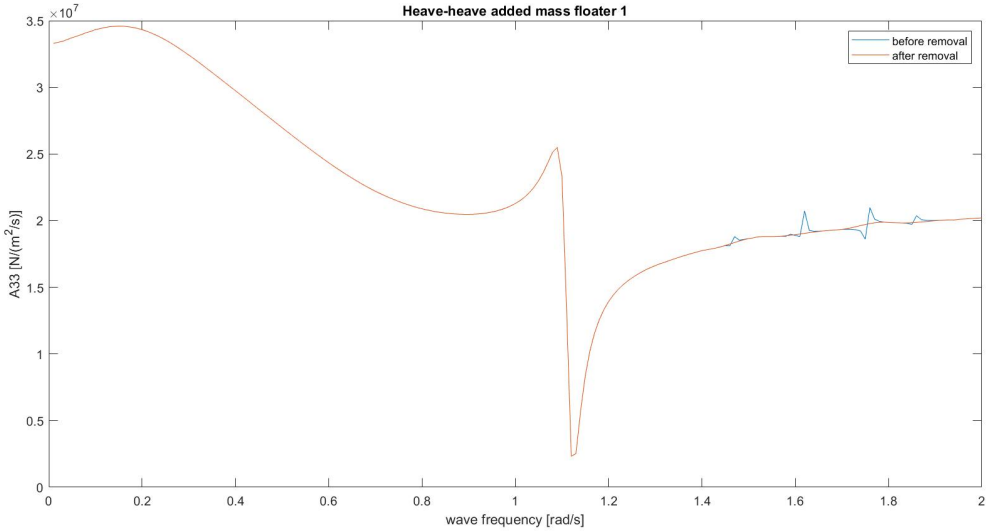

Figure 4.2: Added mass for floater 1 calculated by NEMOH

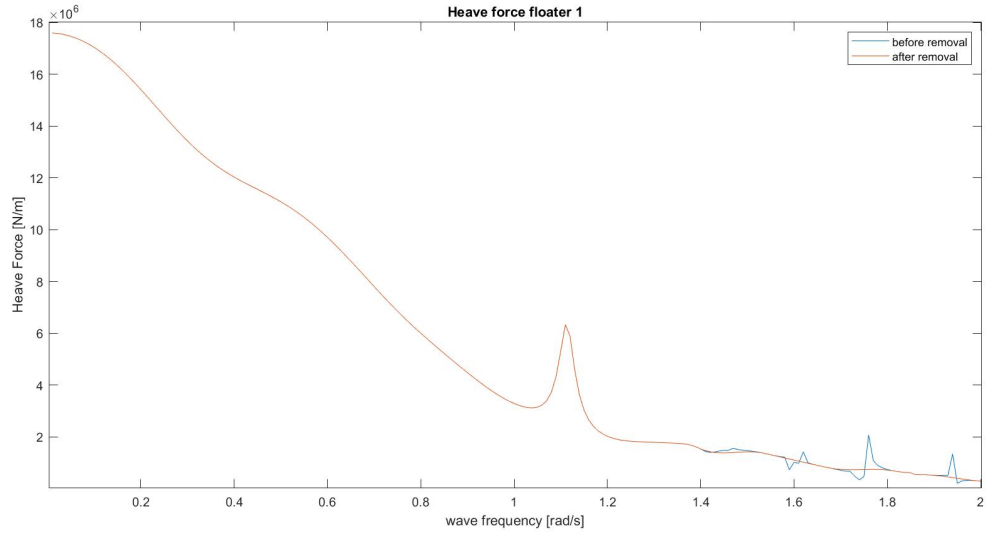

Figure 4.3: Heave force for floater 1 calculated by NEMOH

4.1.5 Gap Resonance

Another phenomenon that occurs when calculating excitation forces and hydrodynamic coefficients for adjacent floaters using a boundary element method is gap resonance. When using NEMOH to mesh the bodies, the part of the floater above the water line is neglected, only the part under the waterline is meshed. The part above the water line is assumed infinitely high.

Furthermore, when using potential theory, no wave breaking or overtopping of water over the floaters is taken into account. Therefore, a resonance peak will occur at some frequencies that gives unrealistically high wave elevations in the gap [51]. Molin et al. did an experimental and numerical study of the gap resonance in-between two rectangular barges [52]. In this study an estimate of the gap resonance frequencies are given, based on moonpool resonance in ships. The frequencies at which gap resonance occurs can then be calculated using equation 4.7.

$$\omega_n^2 \simeq g\lambda_n \frac{1 + J_n \tanh \lambda_n h}{J_n + \tanh \lambda_n h} \qquad \text{[rad/s]} \quad (4.7)$$

where

$$J_n = \frac{2}{n\pi^2 r}\left(\int_0^1 \frac{r^2}{u^2\sqrt{u^2+r^2}}\left[1 + 2u + (u-1)\cos(n\pi u) - \frac{3}{n\pi}\sin(n\pi u)\right] du - \frac{1}{sin(\theta_0)} + 1 + 2r\ln\frac{1+\cos\theta_0}{1-\cos\theta_0}\right) \quad (4.8)$$

with $\lambda_n = n\pi/l$, $r = b/l$ and $\tan(\theta_0) = r^{-1}$ and l the length of the gap, b the width of the gap and h the draft of the gap.

As can be seen from the equation, the frequencies at which gap resonance occurs will be different for different lengths, widths and draft of the gap. Thus, when varying the dimensions of the floater, the gap resonance frequency will change.

In order to obtain realistic values for the motion of the floaters and the forces in the connections between the floaters, these resonance peaks must be suppressed. As can be seen in figure 4.2 at the gap resonance frequency there is a change in added mass, furthermore a peak in wave force occurs as can be seen in figure 4.3. Also, large phase shifts occur at the resonance frequencies.

Ekerhovd et al. also studied gap resonance for side-by-side offloading [53]. In the studies it is discovered that for non-fixed vessels the first gap resonance frequency that occurs has no influence on the motions of both vessels. This is explained by the fact that the disappearance of this mode is caused by the combination of the heave and sway motion to remove the first mode response in the gap. Furthermore, it is stated that in the studies the heave and sway damping have peaks in the odd gap mode frequencies and the pitch and yaw have peaks in the even gap mode frequencies [53]. So for this studies, the first gap resonance mode can be neglected as well, as this doesn't influence the motion and forces. Furthermore, this means that for this study and the conventions used, the odd gap resonance only appear in surge, heave and pitch and the even gap resonance frequencies appear in sway, roll and yaw.

The gap resonance peaks are suppressed by calculating the frequencies at which resonance occurs using equation 4.7, after which around these frequencies the exact frequency at which the peak occurs is found for the relevant degree of freedom. The resonance peaks are then suppressed by excluding the peak point of the graph and then using linear interpolation where the gap resonance frequencies are excluded from the fit, after which the graph is also smoothened to avoid sharp edges after the linear interpolation. However, as the first resonance frequency has no influence on the motion, this resonance frequency is not suppressed. The gap resonance is

suppressed for added mass, damping and wave excitation force. An example of the gap resonance suppression for the sway excitation force can be found in figure 4.4. In this figure it can be seen that part of the resonance peak is removed. In this case the peak and the 2 nearest data points from the peak are excluded from the fit. The results also show the removal of an irregular frequency at $\omega = 1.43 rad/s$. This irregular frequency peak is removed. Furthermore, it shows the suppression of the gap resonance peak in the phase angle as well.

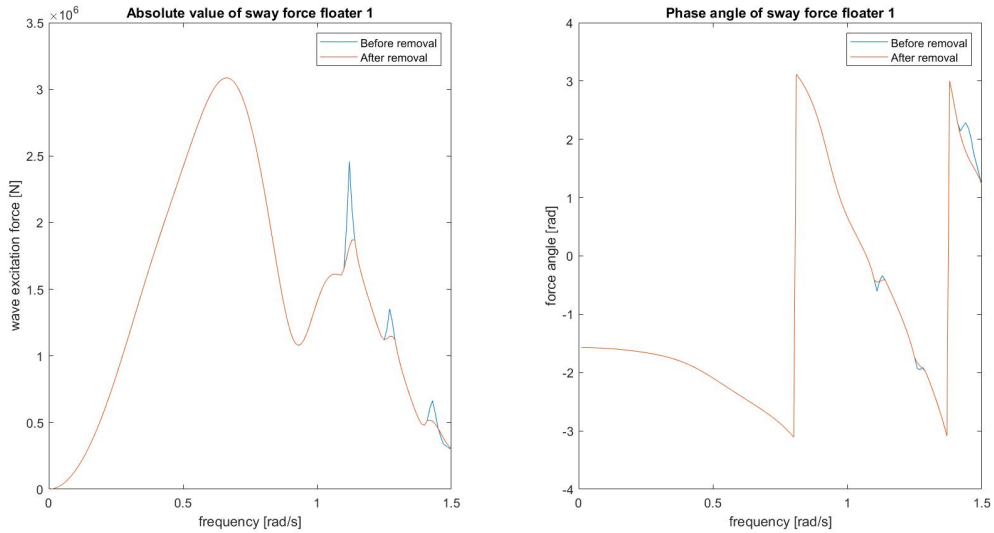

Figure 4.4: Example gap resonance suppression for sway excitation force

4.1.6 Gap Resonance Sensitivity

To analyze what the influence of the gap resonance suppression is on the calculated motions and forces, a sensitivity analysis is done. The gap resonance sensitivity analysis is done for the floater parameters of case 1.2. The parameters can be found in table 4.2. For these parameters the gap resonance frequencies are found and are then suppressed as described previously. In the sensitivity analysis the number of data points that are excluded from the fit are increased and the force in the connection and motion of the floater is then calculated for each new fit. The results are shown in figure 4.5 for no suppression (0 excl) and exclusion of different number of points. $2excl$ means there is 1 point on either side of the peak excluded as well as the peak point itself. $4excl$ means 2 points on either side are excluded and $6excl$ means 3 points on either side are excluded from the graph. The first gap resonance frequency that influenced the motion was at $\omega = 1.19 rad/s$, the peak at $\omega = 1.15 rad/s$ is due to an eigenfrequency of the system with the used parameters. As is shown in the graphs, the resonance peak slowly disappears in the phase for increasing exclusion points. By excluding more points, the gap resonance dissapears. However, as can be seen it is also interfering with the eigenfrequency when excluding 6 points, so this needs to be accounted for.

Table 4.2: Gap resonance sensitivity parameters

Parameter	Value	Unit
L	100	m
B	35	m
T	5	m
H	15	m
d	3.5	m
k_{axial}	10E15	N/m
k_{shear}	10E15	N/m
$k_{bending}$	0	Nm/rad
$k_{torsion}$	0	Nm/rad
μ	0	degrees

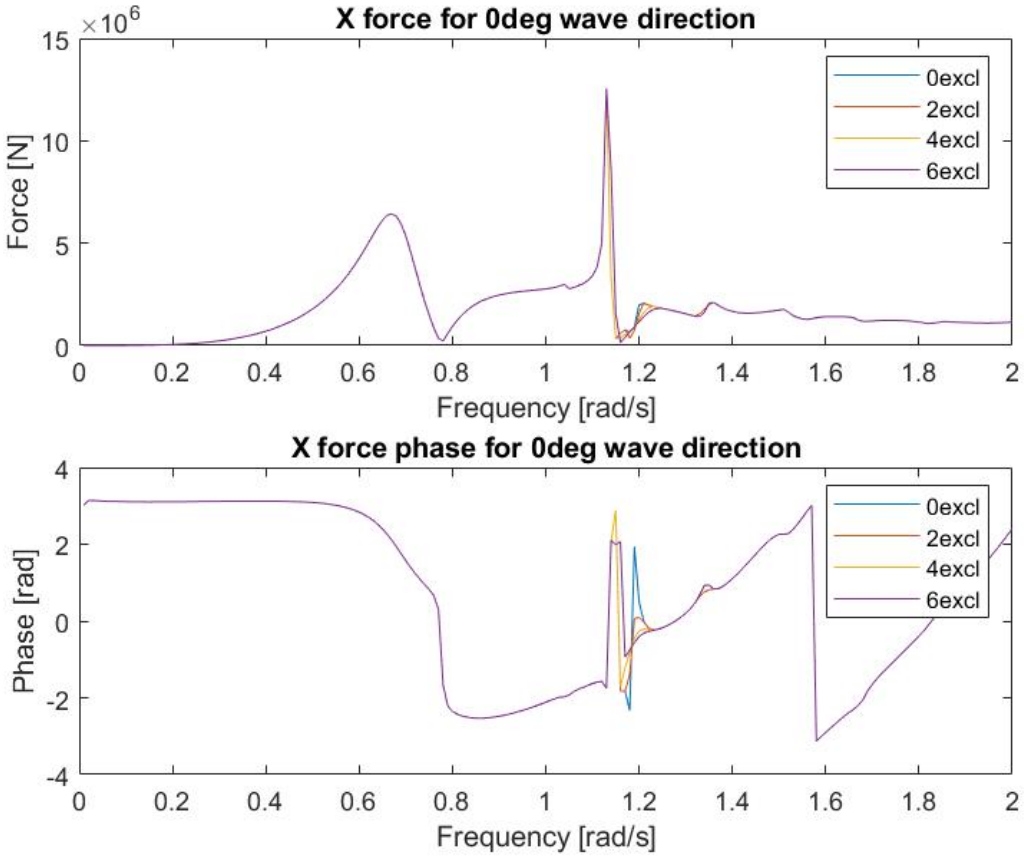

Figure 4.5: Vertical connection force for different gap resonance suppression

After more analysis on the sensitivity of gap resonance it was found that for different dimensions of the floater, the gap resonance peaks become smaller or wider. This means that not one parameter for excluding points from the graph can be chosen for all different cases that will be studied later. Furthermore, full suppression of the gap resonance peaks is means that the results will not represent the real world accurately, as some resonance still occurs in the real world. Therefore, it is chosen to select the number of points to exclude for the gap resonance suppression for each case separately. The number of points is chosen so that only the sharp peak

in the hydrodynamic coefficients and wave excitation forces is suppressed, but the resonance still remains. This will mostly mean that only the peak frequency and 1 point before and after the frequency are excluded from the fit, but this is dependent on the individual case.

4.2 Full Model

The full rigid body model consists of the potential flow solver NEMOH as described in section 4.1.2, after which the results from NEMOH are post processed by removing the irregular frequencies as described in section 4.1.4. Next, the gap resonance is suppressed in the hydrodynamic coefficients and wave excitation force, as described in section 4.1.5. After this post processing the correct input parameters for added mass $A(\omega)$, hydrodynamic damping $B(\omega)$ and complex wave excitation force $\widetilde{F}_w(\omega)$ are available. As well as the mass matrix M and the stiffness matrix C.

As shown in section 3.1.5, equation 3.18, the full equation of motion for a system of 2 bodies with connections is:

$$\widetilde{u}(\omega)(-\omega^2(M + A(\omega)) + i\omega B(\omega) + C + K_{joint}) = \widetilde{F}_w(\omega) \qquad \text{[N]} \quad (4.9)$$

To solve this equation of motion, only the joint stiffness matrix has to be computed for the model.

4.2.1 Joint Stiffness Matrix

The joint stiffness matrix is calculated using the method described in section 3.1.5. The joint is modelled as a set of 6 springs for each degree of freedom. For each of the springs the force F_{joint} is calculated as a function of the displacement vector of the joint u_{joint} and the stiffness k. For the current model, using 2 bodies with 2 connections at each end of the floaters, the joint stiffness matrix K_{joint} will be a linear 12x12 matrix that couples the relative motion between the floaters connection points to the stiffness of the joint.

First, the position of each connection point on both floaters have to be determined. The position can be described using a vector from the center of gravity of each floater. For floater 1 this gives the connection point vectors from equation 4.10, for floater 2 this gives the connection point vectors from equation 4.11 with $b = \frac{1}{2}B$ and $l = \frac{1}{2}L$. For this case it is assumed that the height of the connection point is at the height of the center of gravity of the structure.

$$\begin{bmatrix} x1_{c1} \\ y1_{c1} \\ z1_{c1} \end{bmatrix} = \begin{bmatrix} b \\ -l \\ 0 \end{bmatrix} \qquad \begin{bmatrix} x1_{c2} \\ y1_{c2} \\ z1_{c2} \end{bmatrix} = \begin{bmatrix} b \\ l \\ 0 \end{bmatrix} \qquad \text{[m]} \quad (4.10)$$

$$\begin{bmatrix} x2_{c1} \\ y2_{c1} \\ z2_{c1} \end{bmatrix} = \begin{bmatrix} -b \\ -l \\ 0 \end{bmatrix} \qquad \begin{bmatrix} x2_{c2} \\ y2_{c2} \\ z2_{c2} \end{bmatrix} = \begin{bmatrix} -b \\ l \\ 0 \end{bmatrix} \qquad \text{[m]} \quad (4.11)$$

Using these locations and rotation matrices for both bodies the new position and thus the relative displacement of each connection point after a rotation and translation of each of the floaters can

be described as:

$$u_{c,i,j} = \begin{bmatrix} x_{c,i,j} \\ y_{c,i,j} \\ z_{c,i,j} \\ \phi_{c,i,j} \\ \theta_{c,i,j} \\ \psi_{c,i,j} \end{bmatrix} = \begin{bmatrix} x_i \\ y_i \\ z_i \\ \phi_i \\ \theta_i \\ \psi_i \end{bmatrix} + R_{\phi,\theta,\psi} \begin{bmatrix} xi_{cj} \\ yi_{cj} \\ zi_{cj} \end{bmatrix} - \begin{bmatrix} xi_{cj} \\ yi_{cj} \\ zi_{cj} \end{bmatrix} \quad [\text{-}] \quad (4.12)$$

with i the floater number (1 or 2), j the connection number (1 or 2) and R the rotation matrices for rotaion ϕ, θ and ψ. The relative displacement can then be used to calculate the joint stiffness matrix for the equation of motion using the Laplace equation. The Laplace equation requires the potential energy of the springs. The potential energy in the connection can then be calculated by the relative displacement between the connection points on each of the floaters. The total potential energy of the springs can then be written as:

$$\begin{aligned} V = \frac{1}{2}(k_{x1}(\Delta x_{c1})^2 + k_{y1}(\Delta y_{c1})^2 + k_{z1}(\Delta z_{c1})^2 + k_{\phi 1}(\Delta \phi_{c1})^2 + k_{\theta 1}(\Delta \theta_{c1})^2 + k_{\psi 1}(\Delta \psi_{c1})^2) + \\ \frac{1}{2}(k_{x2}(\Delta x_{c2})^2 + k_{y2}(\Delta y_{c2})^2 + k_{z2}(\Delta z_{c2})^2 + k_{\phi 2}(\Delta \phi_{c2})^2 + k_{\theta 2}(\Delta \theta_{c2})^2 + k_{\psi 2}(\Delta \psi_{c2})^2) \end{aligned} \quad (4.13)$$

Using the total potential energy V, the total joint force for each degree of freedom can be calculated by taking the partial differential of the potential energy equation for each degree of freedom as described in equation 3.19. These joint forces are then linearized in order to use them in the equation of motion in the frequency domain. The linearisation is done using the small angle approximation:

$$\sin(\theta) = \theta \qquad and \qquad \cos(\theta) = 1 \quad [\text{rad}] \quad (4.14)$$

Furthermore, quadratic rotational degree of freedom terms in the joint forces are set to zero. As well as multiplications of different of the form $a\sin(b)$ with a being a degree of freedom of the system. After this linearization, the joint stiffness matrix can be computed taking the partial differential of the linearised joint force for the degrees of freedom of the system. This results in the following joint stiffness matrix K_{joint}

$$K_{joint} = 2 \cdot \begin{bmatrix} k_x & 0 & 0 & 0 & 0 & 0 & -k_x & 0 & 0 & 0 & 0 & 0 \\ 0 & k_y & 0 & 0 & 0 & k_y b & 0 & -k_y & 0 & 0 & 0 & k_y b \\ 0 & 0 & k_z & 0 & -k_z b & 0 & 0 & 0 & -k_z & 0 & -k_z b & 0 \\ 0 & 0 & 0 & k_z l^2 + k_\phi & 0 & 0 & 0 & 0 & 0 & -k_z l^2 - k_\phi & 0 & 0 \\ 0 & 0 & -k_z b & 0 & k_\theta + k_z b^2 & 0 & 0 & 0 & k_z b & 0 & -k_\theta + k_z b^2 & 0 \\ 0 & k_y b & 0 & 0 & 0 & k_\psi + k_y b^2 + k_x l^2 & 0 & -k_y b & 0 & 0 & 0 & -k_\psi + k_y b^2 - k_x l^2 \\ -k_x & 0 & 0 & 0 & 0 & 0 & k_x & 0 & 0 & 0 & 0 & 0 \\ 0 & -k_y & 0 & 0 & 0 & k_y b & 0 & k_y & 0 & 0 & 0 & -k_y b \\ 0 & 0 & -k_z & 0 & -k_z b & 0 & 0 & 0 & k_z & 0 & -k_z b & 0 \\ 0 & 0 & 0 & -k_z l^2 - k_\phi & 0 & 0 & 0 & 0 & 0 & k_z l^2 + k_\phi & 0 & 0 \\ 0 & 0 & -k_z b & 0 & -k_\theta + k_z b^2 & 0 & 0 & 0 & k_z b & 0 & k_\theta + k_z b^2 & 0 \\ 0 & k_y b & 0 & 0 & 0 & -k_\psi + k_y b^2 - k_x l^2 & 0 & -k_y b & 0 & 0 & 0 & k_\psi + k_y b^2 + k_x l^2 \end{bmatrix}$$

4.2.2 Response Amplitude Operator

Using the equation of motion 4.9, the response amplitude operator (RAO) and phase can be computed. The RAO of the structure describes the amplitude of the motions of the structure per meter amplitude of a regular wave for different wave frequencies. For this study the wave frequency range is chosen between 0 and $2rad/s$ as there is not much energy in the wave spectrum above $2rad/s$ in the sea state that is investigated. The RAO can be computed as function of ω by equation 4.15, the phase shift can be be calculated using equation 4.16, with ζ_w the wave elevation.

$$RAO(\omega) = \left|\frac{\widetilde{u}}{\zeta_w}\right| = \left|\frac{\widetilde{F}_w(\omega)}{(-\omega^2(M + A(\omega)) + i\omega B(\omega) + C + K_{joint})}\right| \quad [\text{m/m}] \quad (4.15)$$

$$\epsilon(\omega) = arg\left(\frac{\widetilde{u}}{\zeta_w}\right) = arg\left(\frac{\widetilde{F}_w(\omega)}{(-\omega^2(M + A(\omega)) + i\omega B(\omega) + C + K_{joint})}\right)[\text{rad}] \quad (4.16)$$

4.2.3 Joint Reaction Forces

From the complex response of the structure, consisting of the magnitude and phase response. The complex joint reaction forces can be computed. The reaction force of the response is a function of the response of the both floaters, which is a function of the wave frequency, thus the reaction force of the joints can be computed as a complex function of the wave frequency as well. There are 2 joints, one on the left and one on the right as seen from the 0° wave direction. The connection on the right is denoted as connection 1 and the connection on the left is denoted as connection 2. As seen in the computation of the joint stiffness matrix in section 4.2.1, the joint reaction force can be computed by taking the derivative of the potential energy in each degree of freedom for each of the joints. The potential energy for each of the joints is dependent on the complex motion of the structure. By calculating the joint reaction forces using the amplitude and phase of the response of each floater, the calculated potential energy and the calculated joint reaction force will also be a complex value consisting of an amplitude and phase angle. The complex joint force for connection 1 for all 6 degrees of freedom is described in equation 4.17, the complex joint force for connection 2 is described in equation 4.18. With for the motions subscript 1 being the motion of the first floater and subscript 2 the second floater as seen from the 0° incoming wave direction.

$$\widetilde{F}_{joint1}(\omega) = \begin{bmatrix} k_x(l\psi_1 - l\psi_2 + x_1 - x_2) \\ k_y(b\psi_1 + b\psi_2 + y_1 - y_2) \\ k_z(-b\theta_1 - b\theta_2 - l\phi_1 + l\phi_2 + z_1 - z_2) \\ k_\phi(\phi_1 - \phi_2) \\ k_\theta(\theta_1 - \theta_2) \\ k_\psi(\psi_1 - \psi_2) \end{bmatrix} \quad (4.17)$$

$$\widetilde{F}_{joint2}(\omega) = \begin{bmatrix} k_x(-l\psi_1 + l\psi_2 + x_1 - x_2) \\ k_y(b\psi_1 + b\psi_2 + y_1 - y_2) \\ k_z(-b\theta_1 - b\theta_2 + l\phi_1 - l\phi_2 + z_1 - z_2) \\ k_\phi(\phi_1 - \phi_2) \\ k_\theta(\theta_1 - \theta_2) \\ k_\psi(\psi_1 - \psi_2) \end{bmatrix} \quad (4.18)$$

4.2.4 Spectral analysis

After computing the joint reaction forces as function of the wave frequency, the joint force spectrum can be computed for the occurring wave energy density spectrum in the North sea with a 50 year return period. This force energy density spectrum can be calculated using equation 4.19.

$$S_f(\omega) = \left|\widetilde{F}_{joint}(\omega)\right|^2 S_j(\omega) \qquad [N^2 s] \quad (4.19)$$

In order to give insight in the forces in the joints, the significant joint force can be computed from this force energy density spectrum. By calculating the zeroth order moment area of the spectrum using equation 4.20 and then taking the variance of the spectrum using equation 4.21. The significant force is than calculated using equation 4.22.

$$m_0 = \int_0^\infty S_f(\omega)\, d\omega \quad (4.20)$$

$$\sigma_f = \sqrt{m_0} \quad (4.21)$$

$$F_{sig} = 4\sigma_f = 4\sqrt{m_0} \quad (4.22)$$

Chapter 5 Model validation

In this chapter, the numerical model will be validated. This will be done using numerical and analytical studies previously done by others. The validation is done in 3 steps. First validation is done for a model for a single floater in waves, after which validation for 2 floaters next to each other is done, in the end, validation for 2 floaters connected to each other will be done. In the latter case, the vertical forces in the joints are also checked with the study.

5.1 Single floater validation

The validation for a single floater is done using a study from Sun, Eatock Taylor and Taylor from 2010 [18]. They study water wave diffraction for two parallel rectangular barges. They also compare those results to a single box model. This single box model will be used for validation of the single floater model. It will verify that the calculated hydrodynamic coefficients and forces are correct. Furthermore, it will verify the calculated resulting motions of the single floater.

5.1.1 Wave forces single floater

Sun et al. also use a boundary element method to calculate the hydrodynamic coefficients and forces on the structure. The program DIFFRACT computes the first- and second-order hydrodynamic quantities. The mesh is a quadratic boundary element mesh that is needed for the linear analysis of the DIFFRACT software. To avoid the irregular frequencies, some interior nodes are used, this is done based on their previously done study in 2008 about removing irregular frequencies [54]. A figure of the used mesh can be found in figure 5.1. The conventions for both the 2 box and single box configuration can be found in figure 5.2. The waves propagate in positive y direction. Furthermore, a water depth of 50m is used. In table 5.1 the dimensions of the calculated box can be found [18].

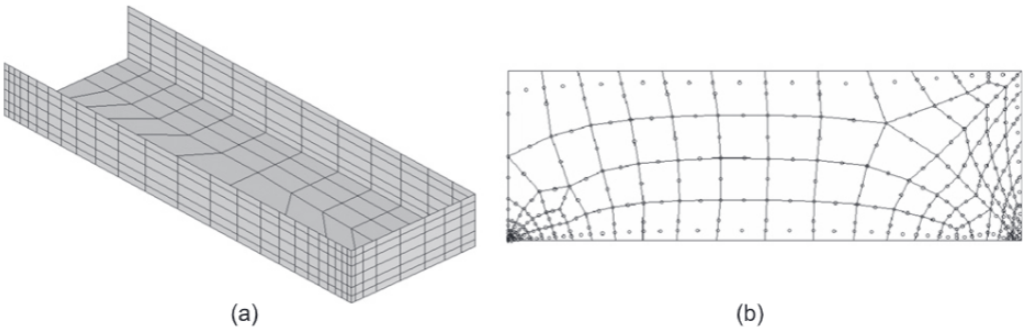

Figure 5.1: Mesh used by Sun et al. (a) body surface mesh, (b) inner free surface mesh [18]

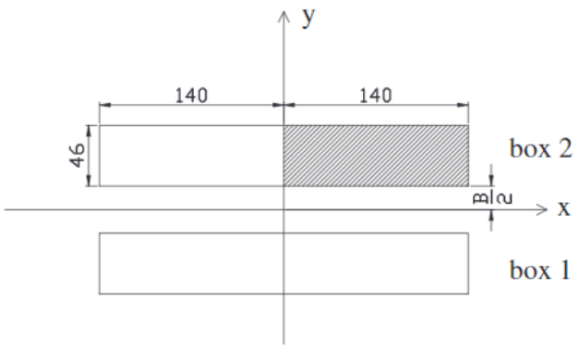

Figure 5.2: General arrangement used by Sun et al. for two boxes.[18]

Table 5.1: Properties of box used by Sun et al.

Parameter	Value [m]
Length	280
Width	46
Draft	16.5
Vertical centre of gravity	16.5
Gap	18

These properties are adapted in the NEMOH based model to verify the calculated forces and motion of the barge. Sun et al. [18] show the sway and heave force and roll moment for a single barge as well as for the double barge configuration as in figure 5.2, for now only the single barge configuration is used. The calculation in the NEMOH based model was done using a mesh of about 300 panels. As discussed in section 4.1.4, some irregular frequencies occurred. The method for removing these using interpolation has has been applied in the shown results. In figures 5.3, 5.4 and 5.5 the comparison between the NEMOH model and the model from Sun et al.[18] is made for the sway force, heave force and roll moment respectively. The force is normalized by $\rho g A$, with A the incident wave amplitude, ρ the density of water and g the gravitational acceleration.

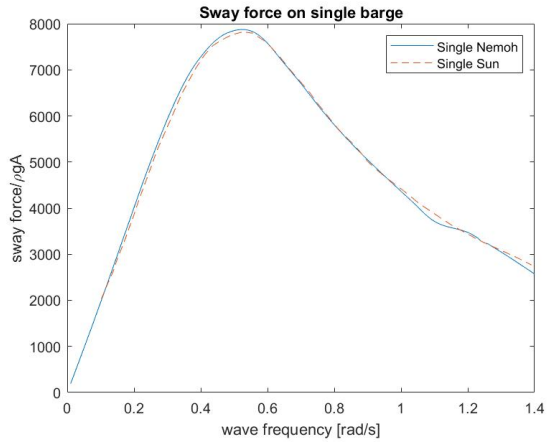

Figure 5.3: Comparison of calculated normalized sway force for a single floater

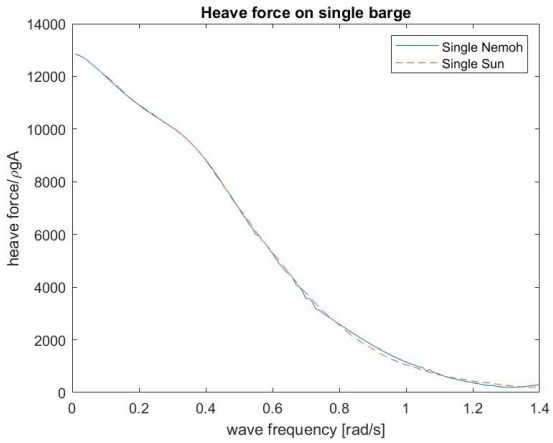

Figure 5.4: Comparison of calculated normalized heave force for a single floater

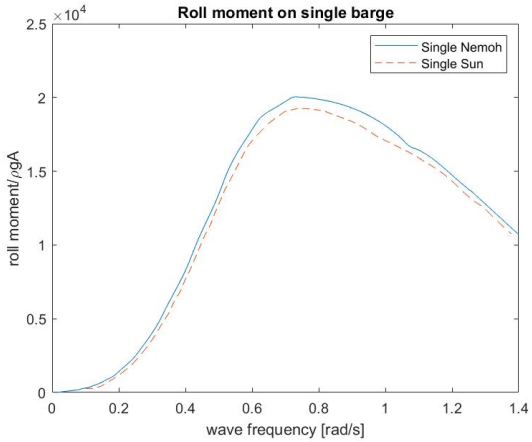

Figure 5.5: Comparison of calculated normalized roll moment for a single floater

As can be seen in the figures, the calculated forces match quite well. Only in roll there is quite larger calculated force. However, because Sun et al. don't show the roll motion of the barge in their article, so it is not possible to see what this does to the roll motion of the NEMOH model in comparison to the model of Sun et al.

5.1.2 Motions single floater

Next, the computed response amplitude operator (RAO) are compared to the results from Sun et al.. In figure 5.6 and 5.7 the comparison of motions in sway and heave direction for the single box are shown. As can be seen, the calculated motions with the hydrodynamic coefficients and forces generated by NEMOH match very well with the motions calculated by Sun et al. There is only a slight deviation in the sway motion at around 0.21 rad/s. This is probably due to a small irregular frequency at that point that is not clearly seen in the hydrodynamic coefficients.

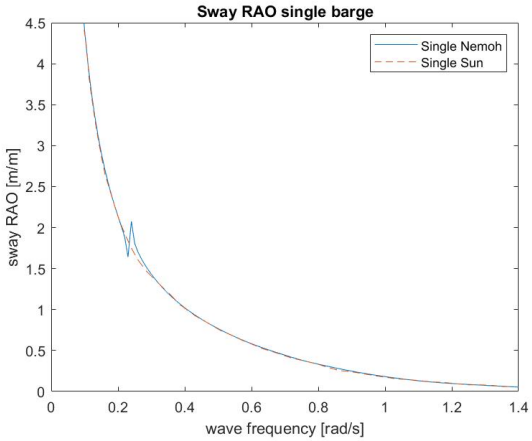

Figure 5.6: Comparison of sway RAO of single floater

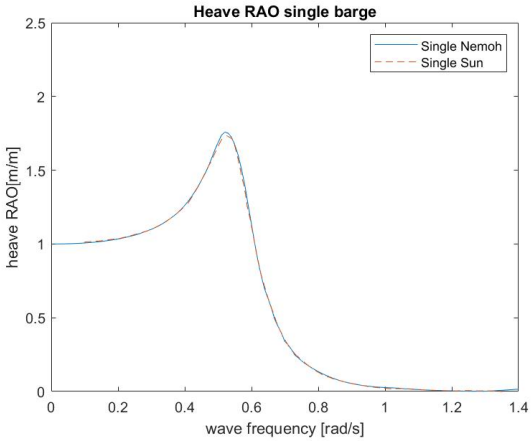

Figure 5.7: Comparison of heave RAO of single floater

5.1.3 Convergence study single floater

A convergence study for the number of panels is done for the single floater configuration. As can be seen in figure 5.8, when increasing the number of panels, the roll excitation force converges towards the model from Sun et al. However, it never reaches the model from Sun et al.. Which indicates an overestimation of the roll excitation force. The calculation for the number of panels from section 4.1.3 indicates that at least 3584 panels should be used. Because the NEMOH model considers symmetry in the x-axis, this number of panels should be half, which indicates about 1800 panels. As can be seen in the figure, the wave excitation force for 1854 panels has almost converged. This indicates that this calculation is sufficient and is used to calculate the number of panels needed for the case studies. When increasing the number of panels, the computational time increases significantly, thus a higher number of panels will give slightly more accurate results, but will increase the computational time significantly, therefore the number of panels as calculated in section 4.1.3 is sufficient for the accuracy needed.

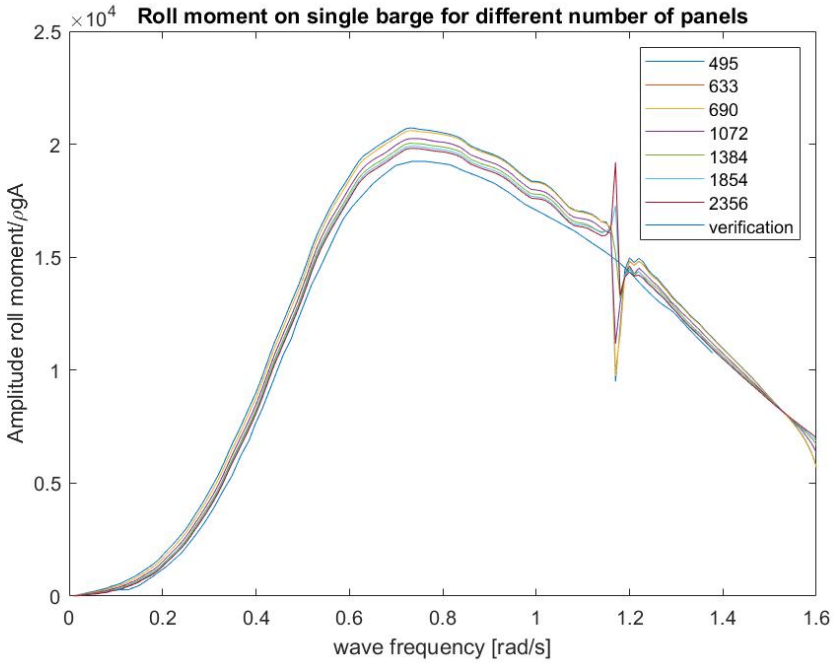

Figure 5.8: Comparison between number of panels for calculated normalized roll moment for a single floater

5.2 Double floater validation

For the 2 adjacent floater validation, the same paper from Sun et al. [18] is used. In this paper a comparison is made between the difference in force and motion of 2 adjacent barges and a single barge. Therefore, the same article can be used to verify the calculated forces on both boxes for 2 separate boxes. The configuration of figure 5.2 is used and the origin of the coordinates is right in between the barges. For this calculation a water depth of 50m is used and the waves propagate again in positive y direction. The boxes that are used have the same properties as stated in table 5.1 with a gap of 18m between the boxes. Due to the effect of radiation and diffraction the forces on the barges will differ a lot from the single box configuration as can be seen later. Also the motion of both barges will differ a lot compared to a single box configuration.

5.2.1 Wave forces

First, the calculated wave forces are validated with the model from Sun et al. [18]. In the figures 5.9, 5.10 and 5.11, the calculated forces for a single floater and the forces on both floaters for a double floater configuration are shown. As can be seen in the figures, the calculated forces using NEMOH match the calculated forces of Sun et al. very well for the double floater configuration. Only in roll are the peaks in the forces slightly higher then the forces calculated by Sun et al..

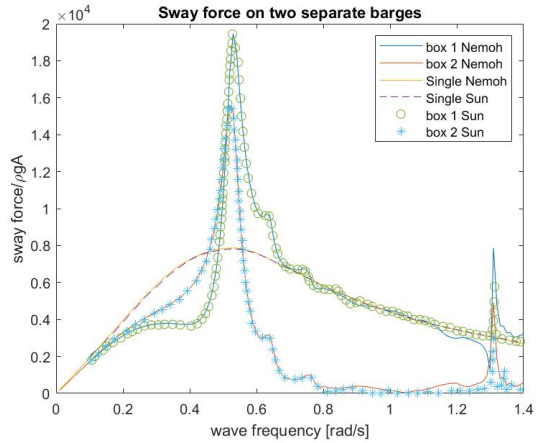

Figure 5.9: Comparison of calculated normalized sway force for double floater configuration

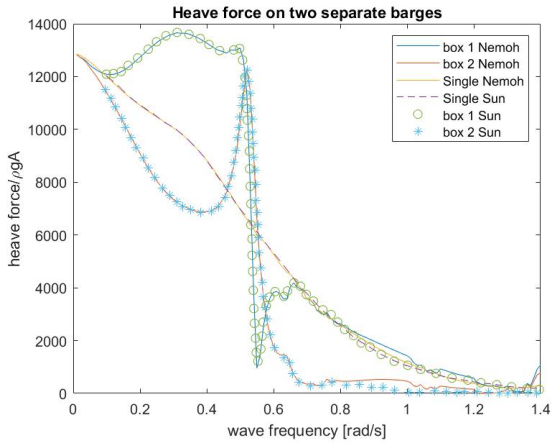

Figure 5.10: Comparison of calculated normalized heave force for double floater configuration

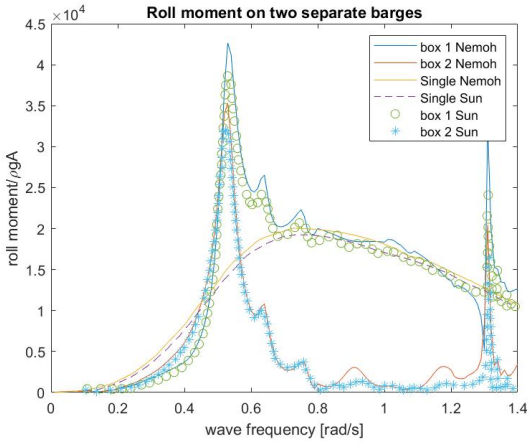

Figure 5.11: Comparison of calculated normalized roll moment for double floater configuration

5.2.2 Motions double floater

Next, the RAO of the motions for the double floater configuration is checked. In the article from Sun et al. there is no RAO available in roll, as was the case for the single floater. So, only the RAO in sway and heave is compared. As can be seen in figure 5.12 and 5.13 the calculated RAO for the double floater configuration match the RAO's calculated by Sun et al. very well. This indicates that the NEMOH based model gives solid results that can be used to compare the forces and motions of 2 floaters next to each other in waves.

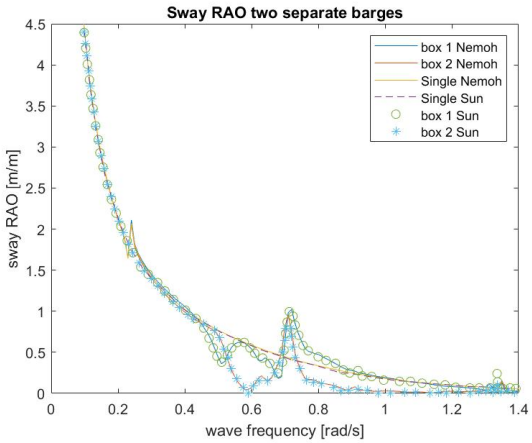

Figure 5.12: Comparison of sway RAO for a double floater

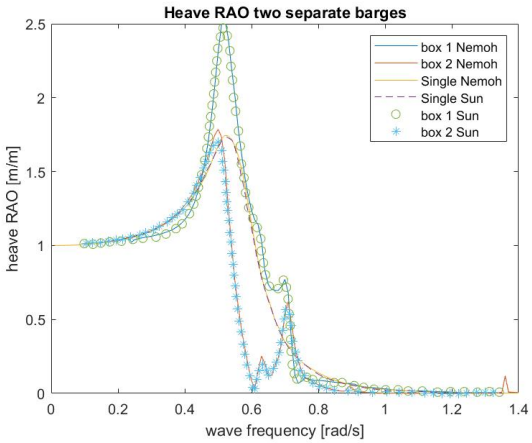

Figure 5.13: Comparison of heave RAO for a double floater

5.3 Connected floaters validation

To verify that the used model for connected floaters also gives accurate results, the calculated motion of connected floaters must also be checked. This is done using calculations by Newmann. In the article 'Wave effects on deformable bodies' the motion of hinged and and rigidly connected floating boxes are calculated [46]. In another article from Sun and Choo the vertical force in the connection is also computed for hinged and rigidly connected floaters [44]. Using these 2 articles the modelling of the connection between the floaters is validated. In the articles the configuration of figure 5.14 is used. The boxes are 40m long with a beam of 10m and a 5m draft. The gap between the barges is 10m with the hinge connection at the center of the gap. The hinge is located at the origin and in the plane of the free surface. The floaters have a uniform mass distribution. Head waves are considered, thus there are motions in surge, heave and pitch.

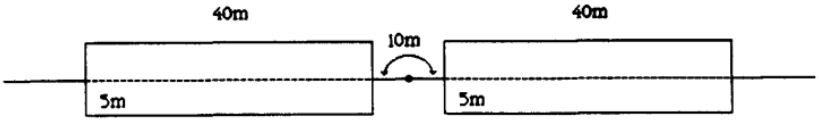

Figure 5.14: Configuration of hinged barges used by Newmann and Sun and Choo

5.3.1 Motions of a rigidly connected floaters

First the connection between the floaters is assumed to be fully rigid. Both floaters are thus assumed to have the same rotation. The vertical motion of the connection point is shown for a wave period between 5 and 12 seconds. The comparison is made between the calculation done by Newmann and the currently used NEMOH based model. As can be seen in figure 5.15 the calculated motion at the center of the connection is a good match for the rigid connection.

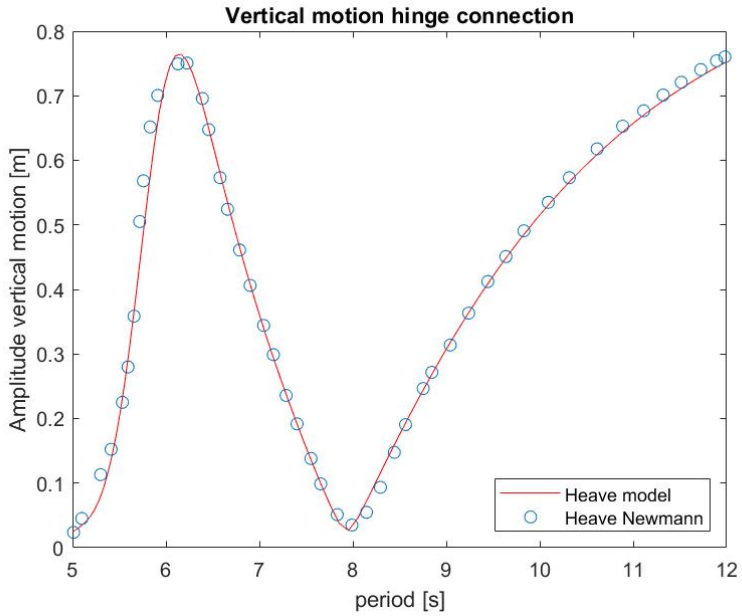

Figure 5.15: Vertical motion at hinge for rigidly connected floaters

5.3.2 Motions of hinged floater

For the hinged connection configuration the stiffness in bending k_θ is set to zero in the joint stiffness matrix. The stiffness in other directions is set as fully rigid. This results in a hinged connection between the floaters. The computed vertical motion of the hinge is then compared to the vertical motion of the hinge in the article from Newmann, furthermore the rotation of the hinge is computed and compared to the calculation done by Newmann for a wave period of 5 to 12 seconds. The rotation of the hinge is non-dimensionalised by $2kA$, with k the wavenumber and A the wave amplitude. This is done to be consistent with the results from Newmann. The results are shown in figure 5.16 and 5.17. As can be seen in the figures, the rotation and therefore the total vertical motion of the hinge are larger for the NEMOH based model than for the model by Newmann. After evaluation it seems that the calculated hydrodynamic stiffness in pitch is too small. The hydrodynamic stiffness is calculated using equations from the book of Journee and Massie [43]. However, when increasing the hydrodynamic stiffness in pitch by 7% the results become far more accurate in comparison to the results from Newmann as can be seen in figure 5.18 and 5.19. It is not clear why there is this difference in pitch rotation for the floaters. In the previously calculated rotational moments from section 5.2 the calculated forces are only slightly higher. One explanation can be that Newmann used extra damping in pitch direction to account for the viscous damping of the water, however this is not mentioned in the article.

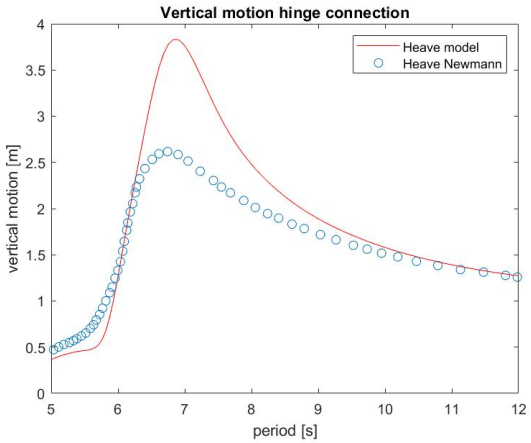

Figure 5.16: Vertical motion of hinge for connected floaters

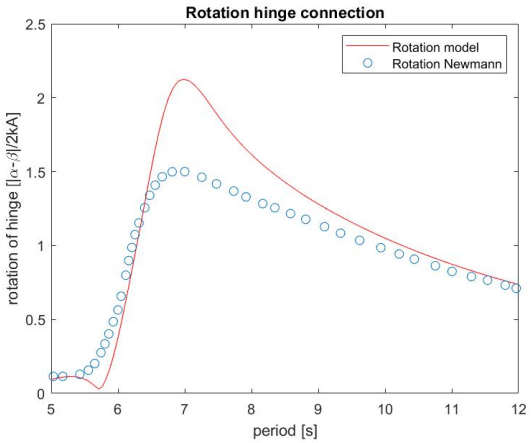

Figure 5.17: Rotation of hinge for connected floaters

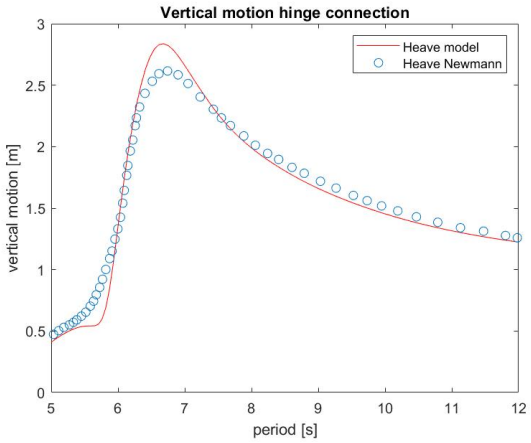

Figure 5.18: Vertical motion of hinge for connected floaters with increased hydrodynamic stiffness in pitch direction

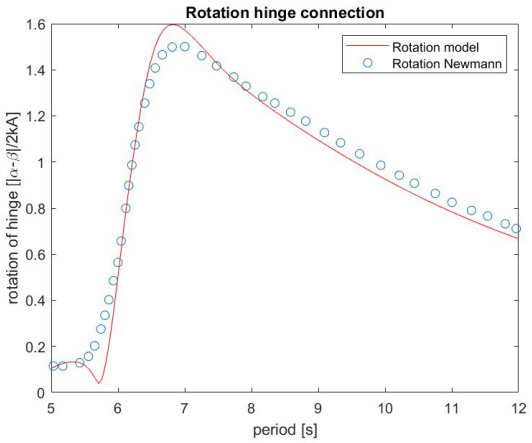

Figure 5.19: Rotation of hinge for connected floaters with increased hydrodynamic stiffness in pitch direction

5.3.3 Connection forces hinged floater

The last validation is done by checking the hinge forces in the connection for the hinged floater configuration. Newmann and Sun and Choo discovered that the vertical force in the connection is the exactly the same for the hinge connection and rigid connection. The hinge does not have an influence on the vertical force in the connection. In figure 5.20 the computed vertical force from the model is compared to the computed force by Newmann. The force is normalized by $\rho g A L B$ with ρ the water density, g the gravitational acceleration, A the wave amplitude, L the length of the floater and B the width of the floater. In figure 5.21 the calculated vertical force with the increase of the hydrodynamic stiffness in pitch of 7% is shown. As can be seen, this increase of stiffness also gives a better match for the calculated vertical force in the hinge.

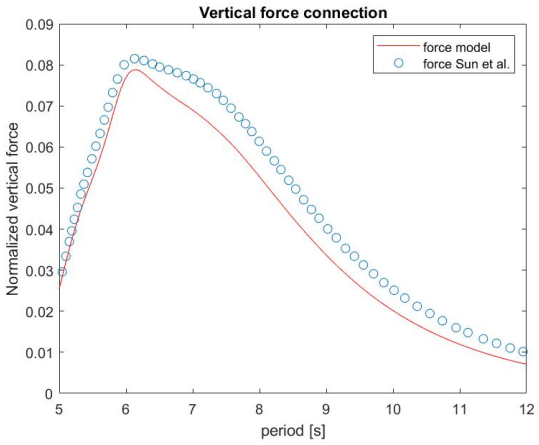

Figure 5.20: Vertical force in the hinge for connected floaters

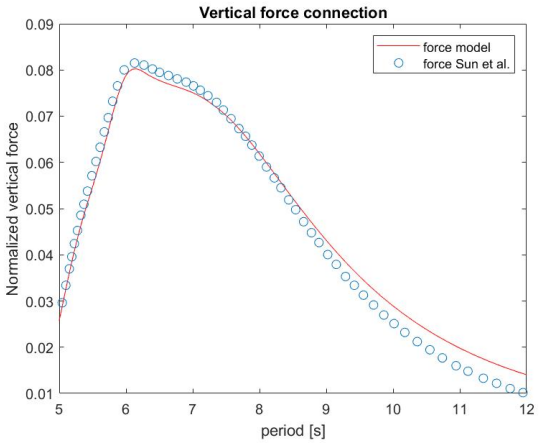

Figure 5.21: Vertical force in the hinge for connected floaters with increased hydrodynamic stiffness in pitch direction

Chapter 6 Case 1: Dimension variation

In this chapter the results of the first case study will be discussed. This is one of two case studies that is done for the model. In the second case the stiffness of the connection between the floaters is varied, described in chapter 7. In the first case study the effect of the size of the floaters on the forces on the connection between the floaters is evaluated. 4 different size parameters are varied: length, width and draft of the floaters and gap between the floaters. In case 1.1 the length will be varied, in case 1.2 several widths are tested, in case 1.3 the draft is varied and in case 1.4 the gap between the floaters is varied. For every sub-case two different wave directions are applied to see the difference in forces and motions for different wave directions. The configuration as shown in figure 6.1 is used for case 1. The 0° wave direction is defined as traveling towards positive x. The x direction is directed in the width of the structure, the y direction is in the length of the structure. Furthermore, in every case the same irregular frequency removal method is applied as explained in section 4.1.4. The gap resonance is also suppressed as explained in 4.1.5. For every floater the target number of bodies for the mesh in NEMOH is set at the number of panels that is just above half of the required number of panels as explained in section 4.1.3. NEMOH then meshes the floaters with a convenient number of panels.

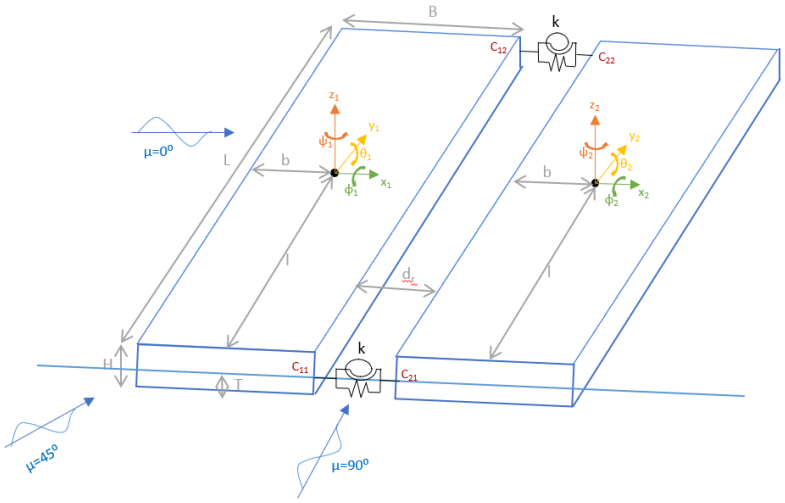

Figure 6.1: Floater configuration used for case 1

6.1 Connection compliance case 1

For all sub-cases the same connection stiffness is set, in order not to introduce another variable effecting the forces. The connection stiffness used in case 1 are based on joints which only allow for rotational movements. The stiffness in x, y and z direction are set at $k = 10E15N/m$. This is the maximum stiffness, so that the joint fully constraints the relative translational motion between the floater and acts as a fully rigid connection in x, y and z direction. The stiffness in rotational directions is set to $0Nm/rad$, so that relative rotational movements are allowed. No damping is applied in the connections. The chosen connection stiffness is inserted into the stiffness matrix K_{joint}. Using the equation of motion from equation 3.18, the motions of the floater as well as the forces in the joints can then be computed. The resulting force spectra are then computed for the occurring wave spectrum as described in section 3.1.6.

6.2 Dimensions

The dimension parameters chosen in both case 1 and case 2 are based on base input parameters provided by TNO. The base case for this study is set a floater of length L of $100m$, a width B of $35m$, a draft T of $5m$ and the gap between the floaters, d, is set at $3.5m$. The dimensions for case 1 are then varied to values lower and higher than this base case. The dimensions for case 2 are set at the values as provided for this base case.

6.3 Case 1.1: Varying the length

In case 1.1 the length of the floater is varied while the rest of the dimensions stay the same. Furthermore, the forces in the joints are analysed for the relevant wave directions. The following subcases are created for case 1.1:

Table 6.1: List of subcases for case 1.1

Casenumber	Length [m]	Width [m]	Draft [m]	Gap [m]	Wave directions [°]	N_{panels}
1.1.1	50	35	5	3.5	[0, 45]	200
1.1.2	100	35	5	3.5	[0, 45]	400
1.1.3	150	35	5	3.5	[0, 45]	550
1.1.4	250	35	5	3.5	[0, 45]	900

The forces occurring in each of the joints for wave frequencies from 0 to $2rad/s$ for each length are then compared. Figure 6.2 shows the results as a force energy density spectrum for the 0° wave direction. The force in y direction is negligible for the 0° direction and therefore not shown. There are no forces in rotational direction, because the stiffness is set to $0Nm/rad$. Figure 6.3 shows the results for the 45° wave direction. Here the forces in y-direction are not negligible. In both figures only results for connection 1 are shown, to illustrate the effects on the connections in every direction. In figures 6.4 and 6.5 the significant force in each direction for different lengths are shown for both wave directions. The significant force can be found using the force energy density spectrum as explained in section 4.2.4.

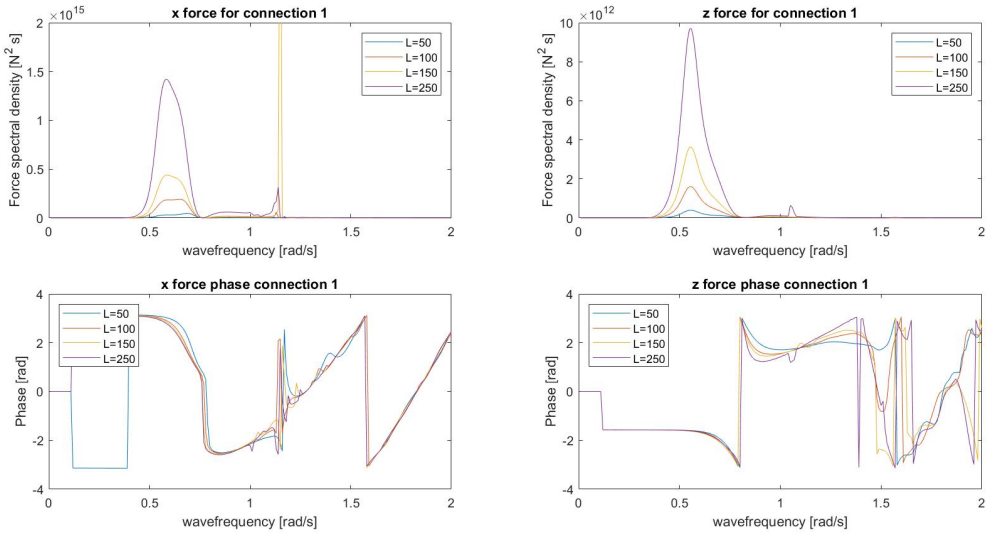

Figure 6.2: Horizontal and vertical force in first connection for case 1.1 for 0° wave direction

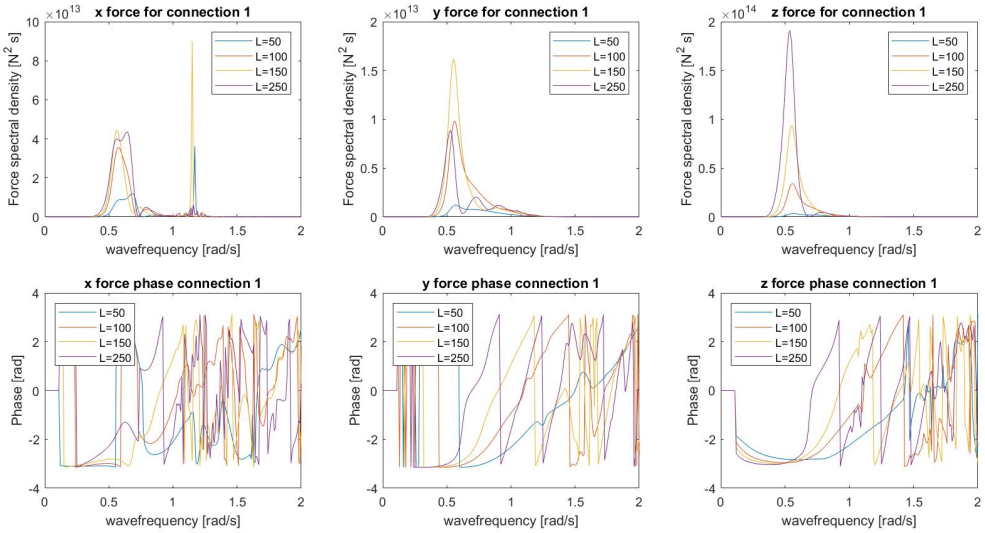

Figure 6.3: Horizontal and vertical force in first connection for case 1.1 for 45° wave direction

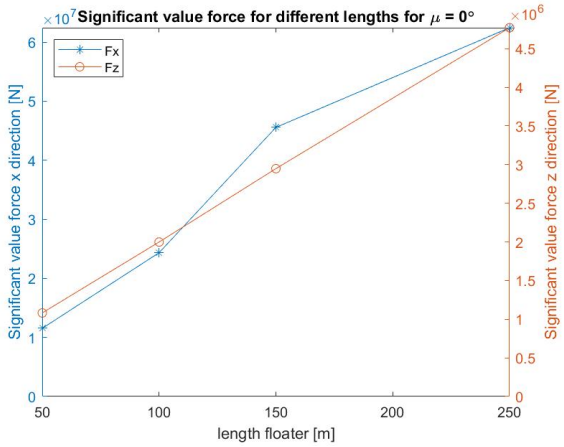

Figure 6.4: Significant value of the force spectra in the first connection for case 1.1 for 0° wave direction

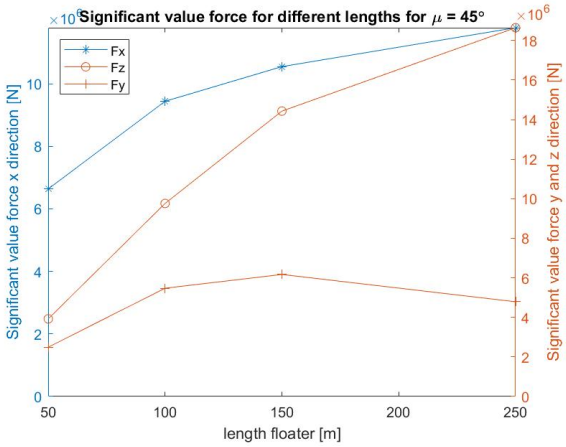

Figure 6.5: Significant value of the force spectra in the first connection for case 1.1 for 45° wave direction

In figure 6.4 it is shown that the significant force increases almost linearly with the length, only for the length of 150m the significant force in x direction is higher than if it was a linear increase, this could be because of the high resonance peak occurring at a frequency of around $\omega = 1.2 rad/s$. Furthermore, for the 45° case as seen in figure 6.5 the force for a length between 100m and 250m increases less than proportional than between 50 and 100m. This is also the case for the significant force in z direction. The significant force in y direction first increases and then decreases. This shows that the length has influence in the total force in y direction for the 45° wave direction for smaller lengths, but for larger lengths this influence is negligible and the significant force becomes smaller. This phenomenon can be explained by looking at the sway RAO for the floaters. The force in y direction is largely influenced by the sway motions of the floaters. As seen in figure 6.6, for the $250m$ long floater, the sway response doesn't interact as much with the occurring wavespectrum, therefore the total force in y direction becomes smaller. Furthermore, the significant force in x and z direction increases less for larger lengths. Finally, the phase of the force changes a lot at higher frequencies and the plot becomes messy.

This phenomenon can be partially explained by the partial suppression of the gap resonance and because of small irregularities in the removal of irregular frequencies. However, due to the energy in the spectrum at high frequencies being very low, the higher frequencies in the phase plots is of less importance.

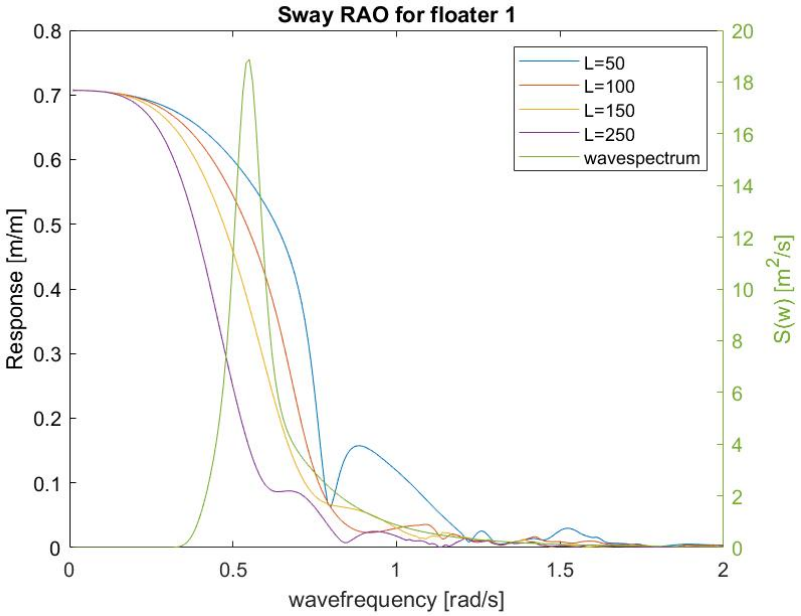

Figure 6.6: Sway RAO for different lengths and the occurring wave spectrum

6.4 Case 1.2: varying the width

In case 1.2 the width of the floater is varied, while the rest of the dimensions stay the same. The forces in the joints are analysed for the wave direction of 45° and 90°. The following subcases are created for case 1.2:

Table 6.2: List of subcases for case 1.2

Casenumber	Length [m]	Width [m]	Draft [m]	Gap [m]	Wave directions [°]	N_{panels}
1.2.1	100	20	5	3.5	[0, 45]	250
1.2.2	100	35	5	3.5	[0, 45]	400
1.2.3	100	75	5	3.5	[0, 45]	700

The forces occurring in each of the joints for wave frequencies from 0 to $2 rad/s$ for each length are then compared. Figure 6.7 shows the results as a force energy density spectrum for the 0° wave direction. The force in y direction is negligible for the 0° direction and therefore not shown. Figure 6.8 shows the results for the 45° wave direction. Here the forces in y-direction are not negligible. In both figures only results for connection 1 are shown, to illustrate the effects on the connections in every direction. In figures 6.9 and 6.10 the significant force in each direction for different lengths are shown for both wave directions.

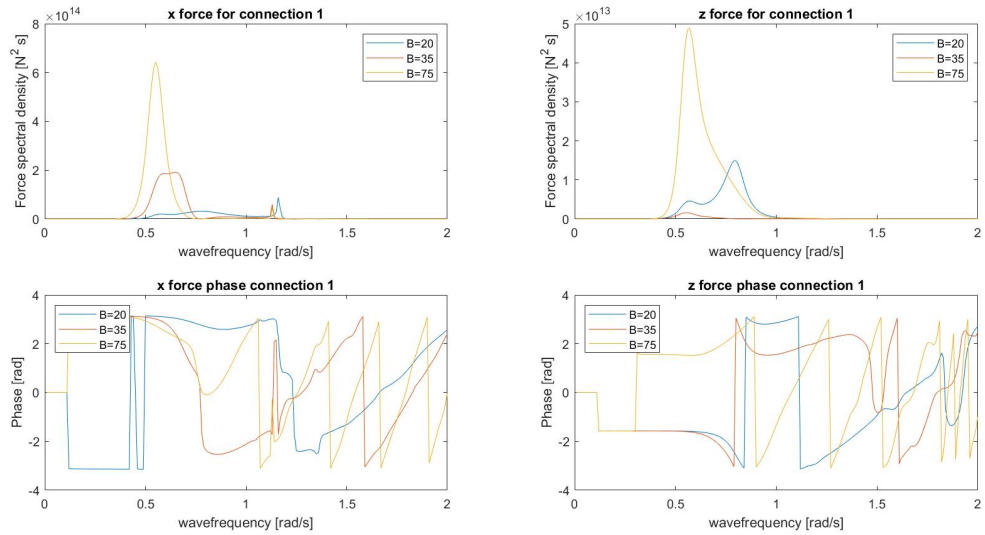

Figure 6.7: Horizontal and vertical force spectra in first connection for case 1.2 for 0° wave direction

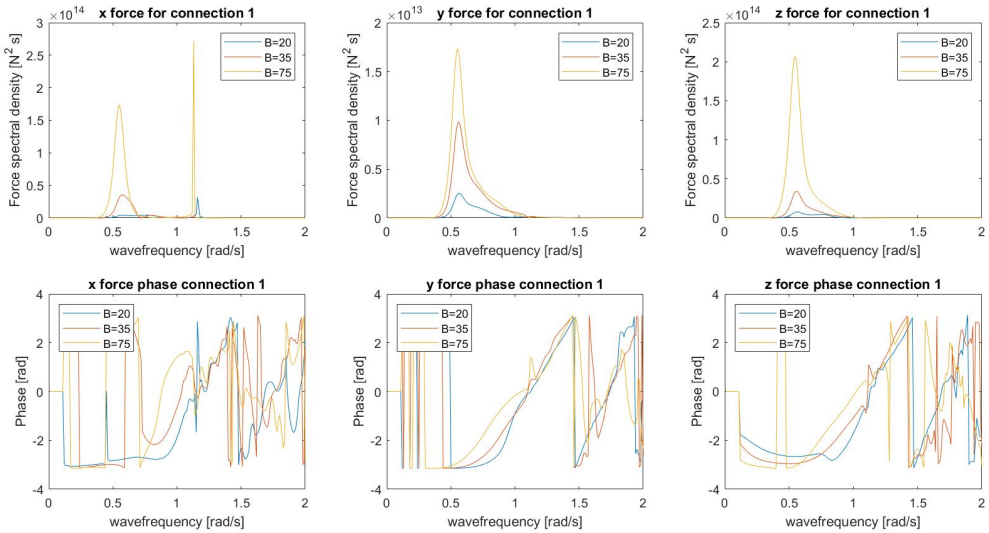

Figure 6.8: Horizontal and vertical force spectra in first connection for case 1.2 for 45° wave direction

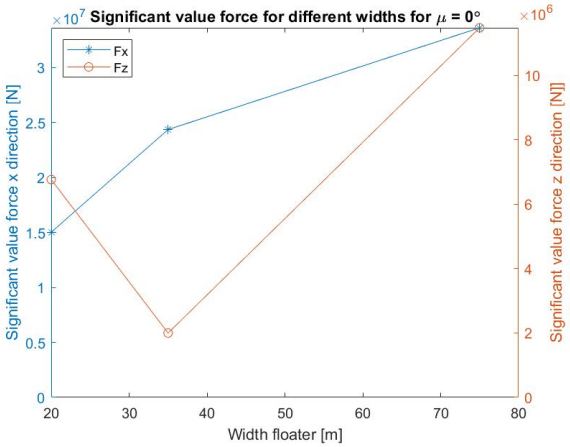

Figure 6.9: Significant value of the force spectra in the first connection for case 1.2 for 0° wave direction

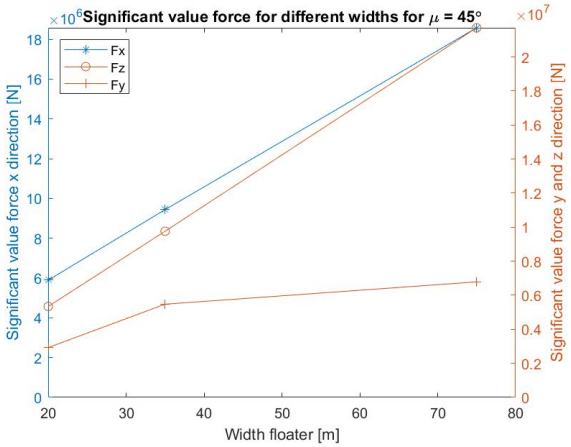

Figure 6.10: Significant value of the force spectra in the first connection for case 1.2 for 45° wave direction

Figure 6.9 shows that the significant vertical force for a width of 20m is higher than the vertical force for a width of 35m. The vertical force is dependent on the difference in the height position of the connection point between each floater. The height is dependent on heave z of the 2 structures as well as the difference in pitch θ as seen in the equation for joint reaction forces, equation 4.17. Because of relatively larger heave and pitch both floaters for a width of 20m, as seen in figure 6.11, this difference in height at the connection point also increases. The difference in height at the connection point for the 20m wide floater and 35m wide floater are shown in figure 6.12 and 6.13. In these graphs is is shown that the main difference in connection force for the 20m wide floater is due to the large difference in heave and pitch around a wave frequency of $0.8 rad/s$. Furthermore, in the phase of the motion it shows that there the difference in phase for the 20m wide floater is larger than for 35m, mostly there is a phase difference of around π, however this differs more for the 20m width floater in heave. In pitch this phase difference is smaller for the 20m wide floater. A resonance peak also occurs at a frequency of $0.45 rad/s$ for the 20m width, however, as can be seen in figure 6.12, this resonance peak is the same for both floaters and doesn't have an influence on the force in the connection. As for case 1.1, the phase of the force changes a lot at higher frequencies and the plot becomes messy. Because of the low energy density at high frequencies, this part of the phase plot is not that relevant.

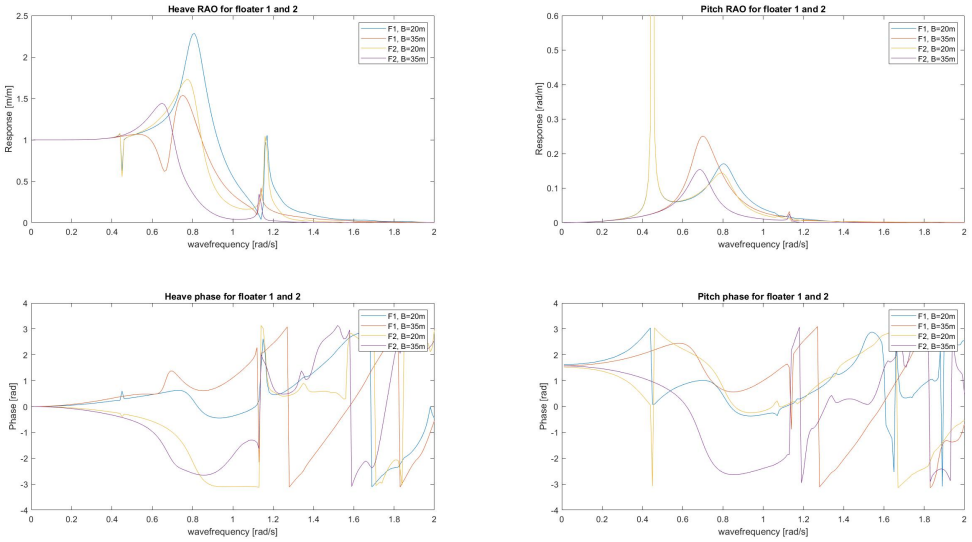

Figure 6.11: Heave and pitch RAO and phase for width of 20m and 35m for both floaters for 0° wave direction

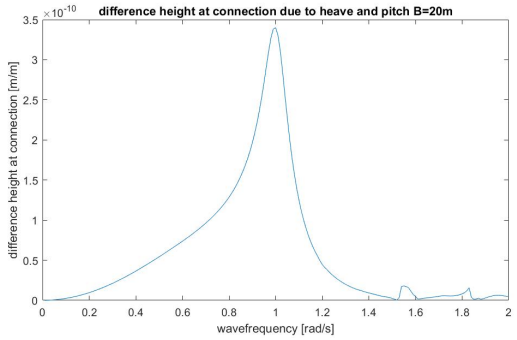

Figure 6.12: Difference in height at connection point for floater of 20m width

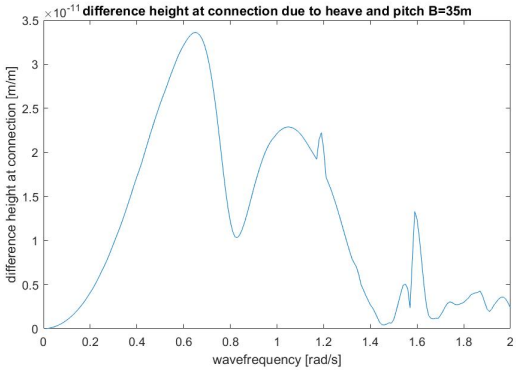

Figure 6.13: Difference in height at connection point for floater of 35m width

Furthermore, figure 6.9 shows that the significant force x-direction increases less when the width of the floater increases. This is also the case for the 45° direction as seen in figure 6.10. However, the decrease of the force is less than for the 0° wave direction. The difference in z-direction for the 20m width and 35m width is not appearing in the 45° wave direction as it now increases linearly with increasing width of the floater. At last, it can be concluded that a change in width does increase the force in y-direction but does not influence the force in y-direction as much as in the x and z-direction. This can again be explained by the response in sway direction interacting less with the occurring wave spectrum as seen in figure 6.14 , as in case 1.1. However, for the width this sway motion is still significant, thus the force doesn't decrease. Therefore, for this sea state, the force in y direction increases less for an increasing width of the structure.

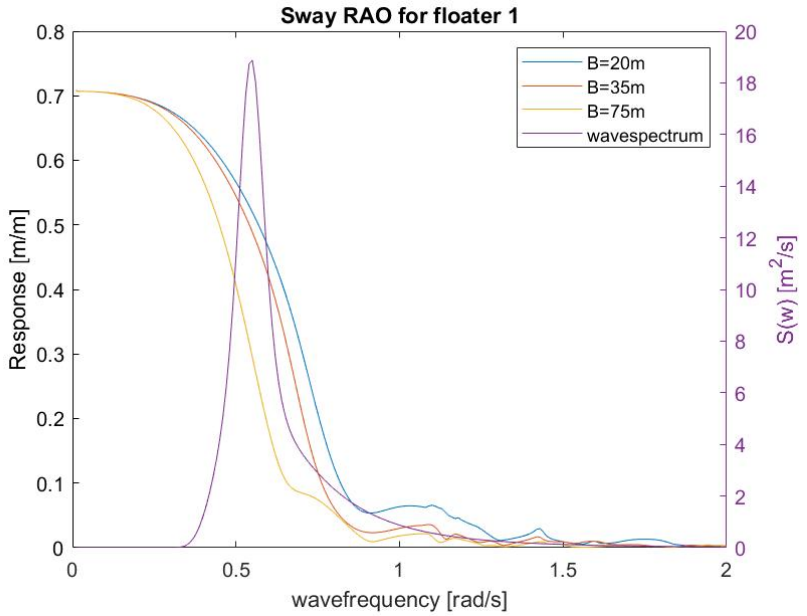

Figure 6.14: Sway RAO for different widths and the occurring wave spectrum

6.5 Case 1.3: varying the draft

In case 1.3 the draft of the floater is varied, while the rest of the dimensions stay the same. The forces in the joints are analysed for the wave directions of 0° and 45°. The following subcases are created for case 1.3:

Table 6.3: List of subcases for case 1.3

Casenumber	Length [m]	Width [m]	Draft [m]	Gap [m]	Wave directions [°]	N_{panels}
1.3.1	100	35	1	3.5	[0, 45]	300
1.3.2	100	35	5	3.5	[0, 45]	400
1.3.3	100	35	10	3.5	[0, 45]	500

The force spectra occurring in each of the joints for wave frequencies from 0 to $2rad/s$ for each draft are then compared. For the 0° case the results can be found in figure 6.15 for connection 1. The relevant results in x and z direction are shown. For the 45° case the results can be found in figure 6.16 for connection 1. The results in x, y and z direction are shown.

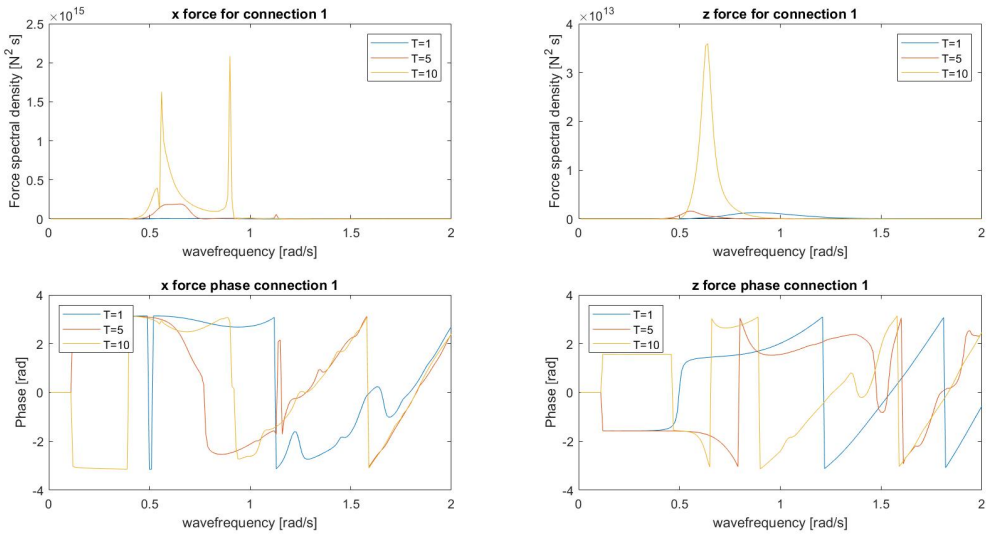

Figure 6.15: Horizontal and vertical force in first connection 1 for case 1.3 for 0° wave direction

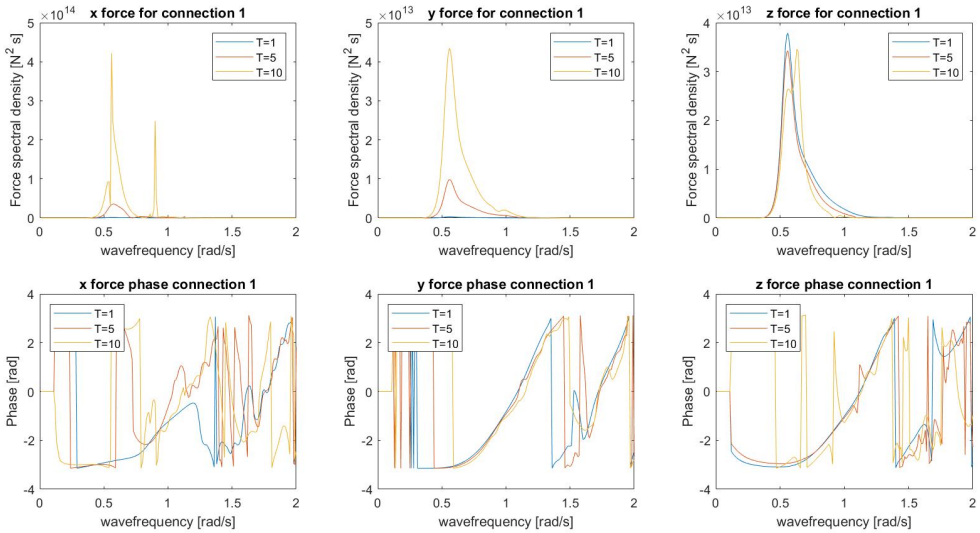

Figure 6.16: Horizontal and vertical force in first connection 1 for case 1.3 for 45° wave direction

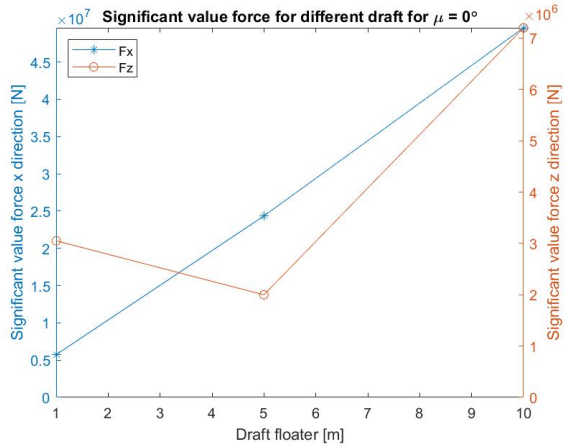

Figure 6.17: Significant value of the force spectra in the first connection for case 1.3 for 0° wave direction

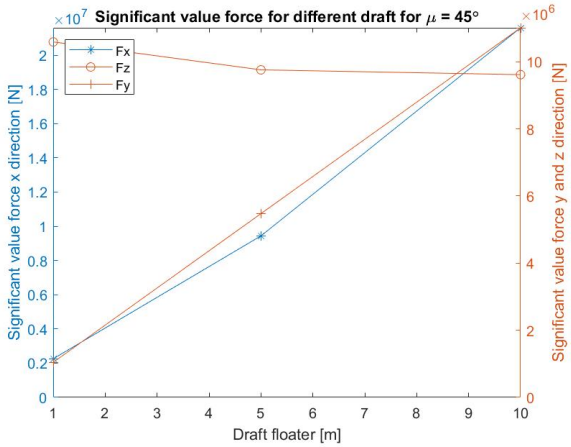

Figure 6.18: Significant value of the force spectra in the first connection for case 1.3 for 45° wave direction

Figure 6.17 shows that between a draft of 1 and 5 m the significant vertical force decreases, and between a draft of $5m$ and $10m$ the vertical force increases significantly. However, figure 6.19 shows that the maximum force does increase for a larger draft, only the width of the force spectrum is much larger for a draft of 1m than for a draft of 5m, therefore the significant force also increases. This indicates that the force is at its maximum for a larger number of wave frequencies for a smaller draft than for a 5m draft. The force in x direction increases linearly for an increasing draft.

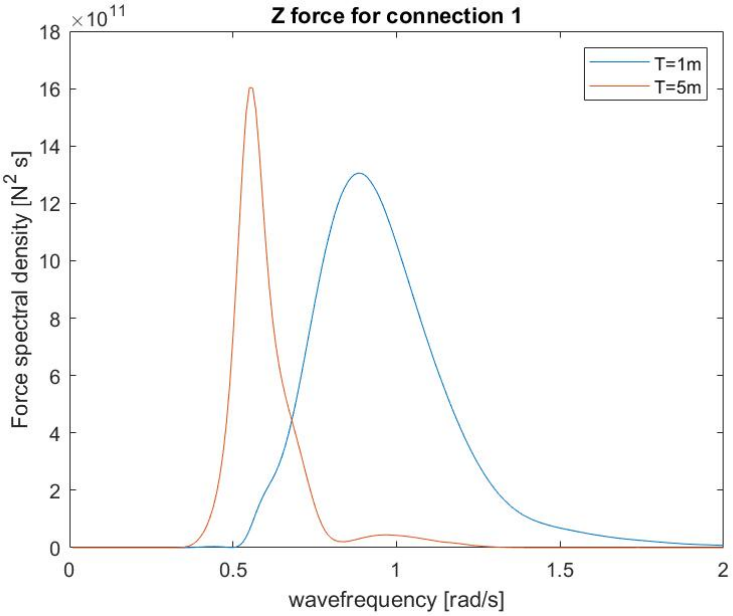

Figure 6.19: Amplitude of force spectrum for draft of 1m and 5m for 0° wave direction

This linear increasing force in x direction is also the case for the 45° wave direction, there is only a slight increase in directional coefficient. The significant force increases linearly as well in y direction. However, the significant force in z-direction decreases slightly for an increasing draft, this can be explained by the spectrum narrowing for the force in z direction. There is a

resonance peak occurring around a frequency of $0.5 rad/s$ in both the 0° and 45° wave direction for the draft of 10m due to an eigenfrequency of the system. As seen, there is also a large difference between the spectra in z-direction in the 45° wave direction when compared to the 0° wave direction. For a draft of $T = 10m$ the force spectral density does not change much between the two wave directions. However for smaller drafts the force in z-direction increases for the 45° direction when compared to the 0° direction. This can be explained by the addition of roll motion (rotation about x-axis) in the 45° wave direction. The additional roll motion increases the significant forces in z-direction. The difference in roll motion between the floaters increases for smaller drafts and therefore increases the energy density spectrum and thus the significant force for smaller drafts. Finally, the phase of the force changes a lot at higher frequencies and the plot becomes messy. This phenomenon has the same explanation as in case 1.1 and because of the low energy density in that part of the spectrum, the phase plot in high frequencies can be ignored.

6.6 Case 1.4: varying the gap width

In case 1.4 the gap width between the floaters is varied, while the rest of the dimensions stay the same. The forces in the joints are analysed for the wave direction of 0° and 45°. The following subcases are created for case 1.4:

Table 6.4: List of subcases for case 1.4

Casenumber	Length [m]	Width [m]	Draft [m]	Gap [m]	Wave directions [°]	N_{panels}
1.4.1	100	35	5	1	[0, 45]	400
1.4.2	100	35	5	3.5	[0, 45]	400
1.4.3	100	35	5	5	[0, 45]	400
1.4.4	100	35	5	7.5	[0, 45]	400

The forces occurring in each of the joints for wave frequencies from 0 to $2 rad/s$ for each gap are then compared. For the 0° case the results can be found in figure 6.20 for connection 1. The results in x and z direction are shown. The results for the 45° case can be found in figure 6.21. Only the relevant results in x, y and z direction are shown.

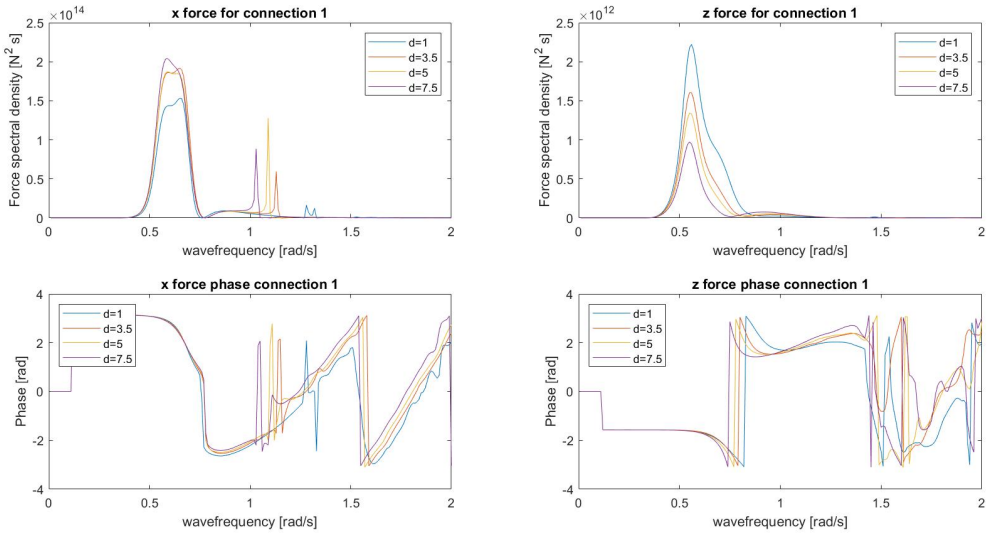

Figure 6.20: Horizontal and vertical force spectra in first connection for case 1.4 for 0° wave direction

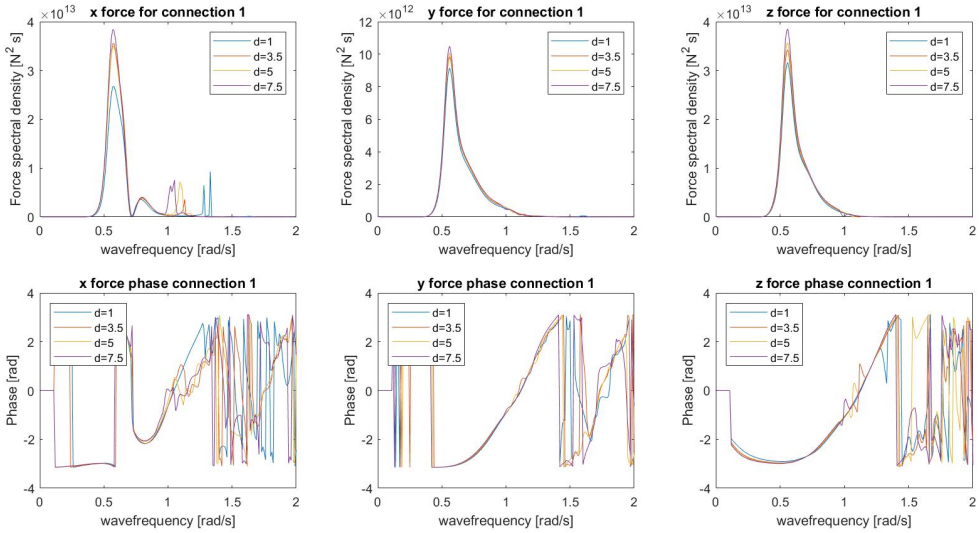

Figure 6.21: Horizontal and vertical force spectra in first connection for case 1.4 for 45° wave direction

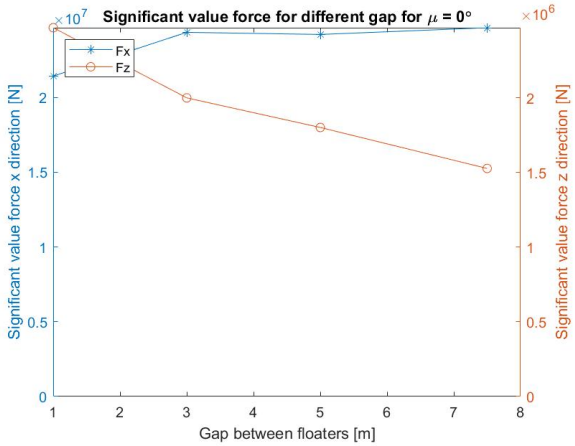

Figure 6.22: Significant value of the force spectra in the first connection for case 1.4 for 0° wave direction

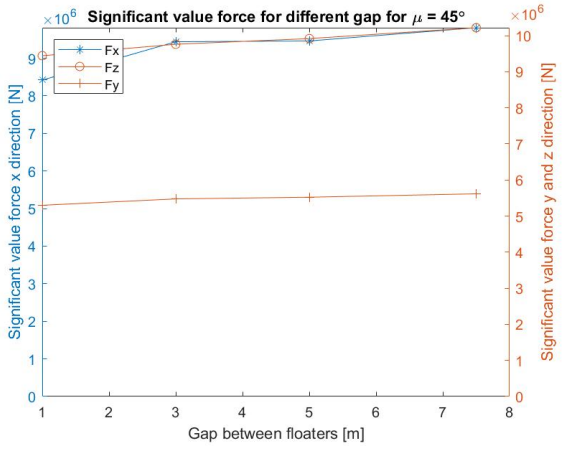

Figure 6.23: Significant value of the force spectra in the first connection for case 1.4 for 45° wave direction

Figure 6.22 shows that the width of the gap does have a significant impact on the vertical force for 0° wave direction. A smaller gap gives higher vertical forces in the connection. This can be explained because a larger gap gives less interaction between the two floaters. This gives a slight decrease in pitch motion as seen in figure 6.24, as the vertical force is influenced by this pitch motion, this force decreases. Furthermore, it is shown that it does increase the horizontal force for increasing gap width. This increase in x direction can be declared by the decrease of the shielding effect of the first floater with regard to the second floater.

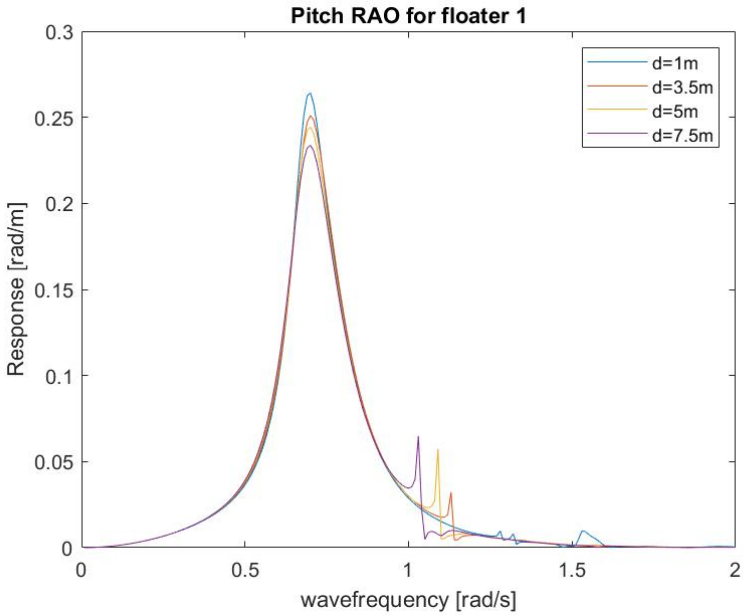

Figure 6.24: Amplitude of pitch motion for different gap widths for 0° wave direction

Figure 6.23 shows that the gap width has significantly less influence on the forcing for the 45° wave direction than for the 0° wave direction. The force in y direction stays roughly the same, the x force increases as was the case for the 0° case, the force in z direction only increases slightly for increasing gap. For the 45 degree wave direction, the gap width has less influence on the pitch motion of the floaters, thus the influence on the vertical force also disappears.

6.7 Overview case 1

A full overview of the results from case 1 are shown below. The data shown is the significant force for each case for the wavespectrum with a 50 year return period. Figure 6.25 shows the results for the 0° wave direction and figure 6.26 show the results for the 45° wave direction. Only the relevant results are shown for each wave direction.

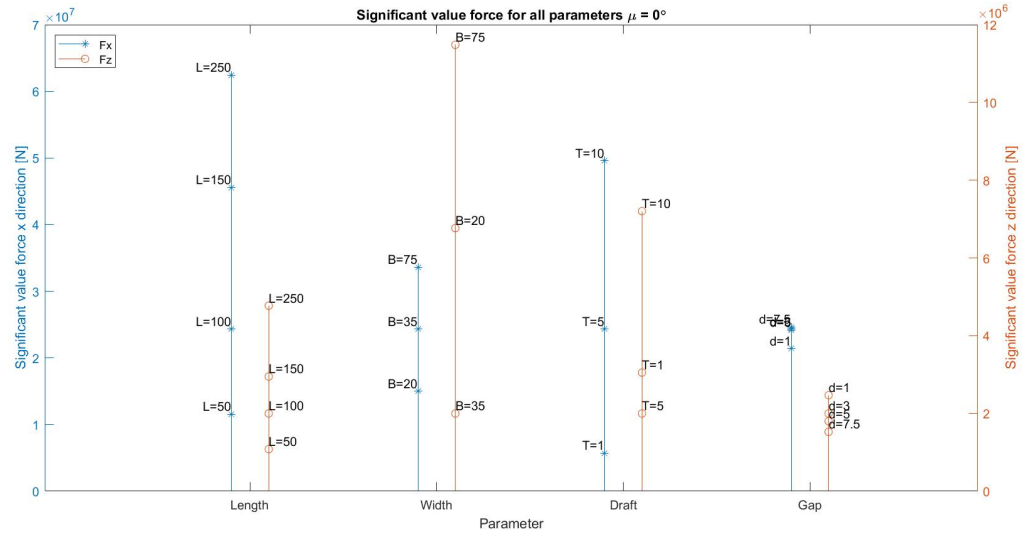

Figure 6.25: Comparison of significant value of the forces and moments in first connection for case 1 for 0° wave direction

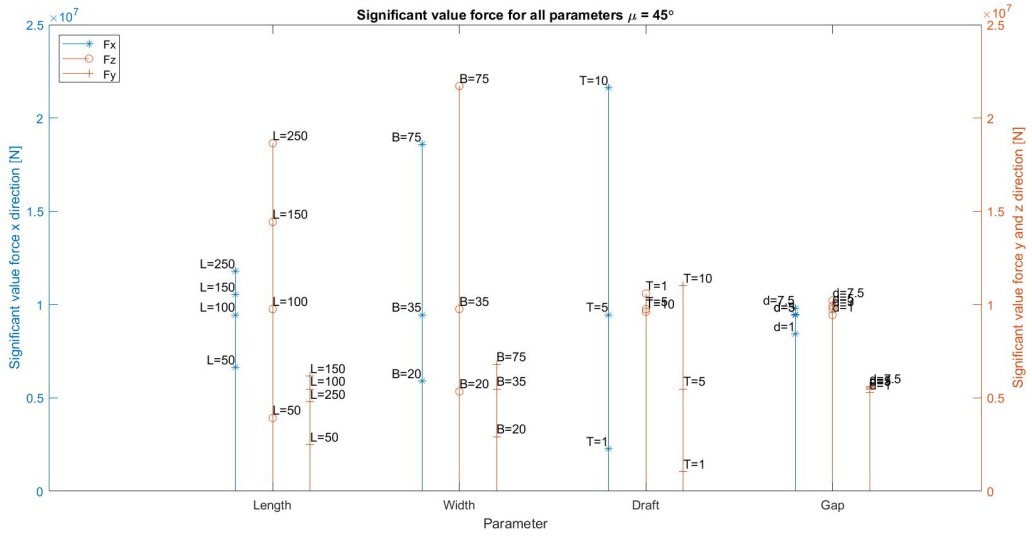

Figure 6.26: Comparison of significant value of the forces and moments in first connection for case 1 for 45° wave direction

6.8 Comparison between connections for $\mu = 45°$

In this section, a comparison is made between the significant value for the two connections for the 45° wave direction. This analysis is not done for the 0° case as the forces for this case are similar for each connection. The comparison is done using the significant value of the force. When there is a large difference between the significant value of the forces this will be explained or elaborated using the relevant force spectra and phase angle of the forces.

For case 1.1 where the length of the floater is varied the significant value of the force for connection 1, the connection on the right side when looking from the 0° wave direction towards the floaters, denoted as con1 in the figure, is compared to the force in connection 2, denoted as con2

in the figure. The results are shown in figure 6.27. As seen in the figure, the force in vertical direction is slightly higher for the second connection, but the shape of the figure is similar. The force in y direction is exactly the same for each connection for the 45° wave direction. However, the force in x direction increases between $L = 50m$ and $L = 150m$ for connection 2, but then decreases for $L = 250m$. This is mainly due to difference in yaw motion. As the floater rotates around the z-axis the force in one joint increases while the other decreases. This phenomenon is occurs with a larger influence for the 250m length floater as this force is defined as the difference in rotation of the floaters times half the length of the floater times the stiffness of the joint. Therefore, there is a larger difference in force for 250m length barge between connection 1 and 2. The results for varying the widths are shown in figure 6.28. Here it is again shown that the force in x-direction is higher for connection 2 when compared to connection 1. The significant force in y-direction stays the same. The force in z-direction is lower in connection 2 for smaller widths, but increases more proportionally to the width when compared connection 1. For varying draft, the comparison between the significant force in connection 1 and 2 can be found in figure 6.29. As seen, the force in x direction is again higher for connection 2. However, an increase in draft decreases the vertical force in z direction more for connection 2 when compared to connection 1. The force in y-direction again stays the same. The comparison between the significant forces in the connections for varying gap width can be found in figure 6.30. Again, the force in x-direction is higher in connection 2 for the 45° wave direction. The significant force in z-direction is higher in connection 1 and the significant force in y-direction is equal in both connections.

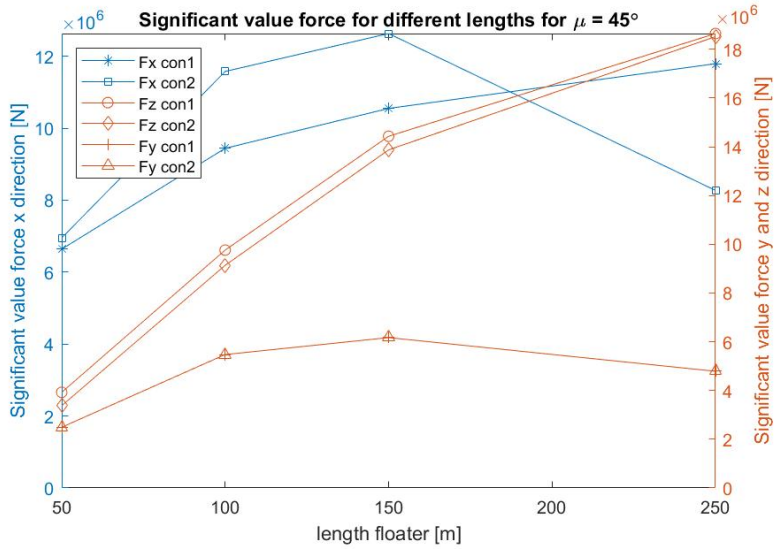

Figure 6.27: Comparison of significant value of the forces in the connections for case 1.1 for 45° wave direction

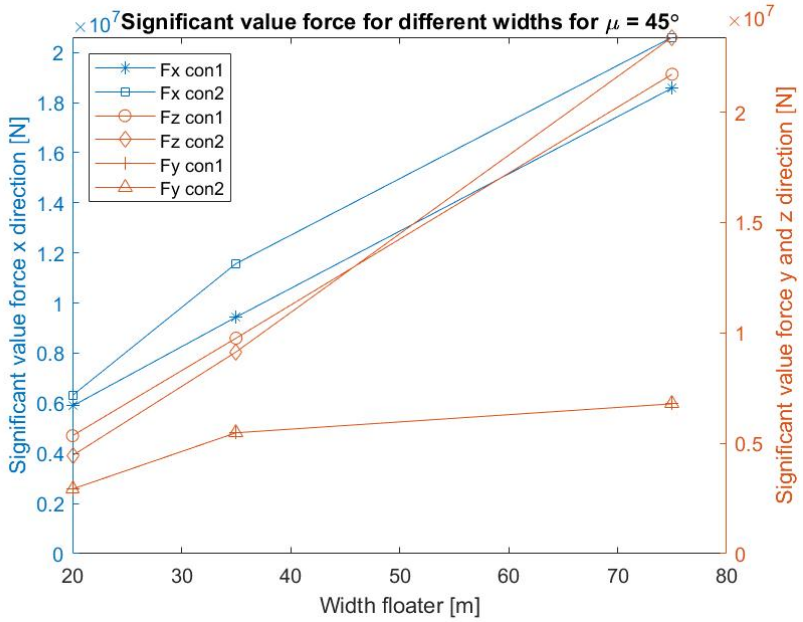

Figure 6.28: Comparison of significant value of the forces in the connections for case 1.2 for 45° wave direction

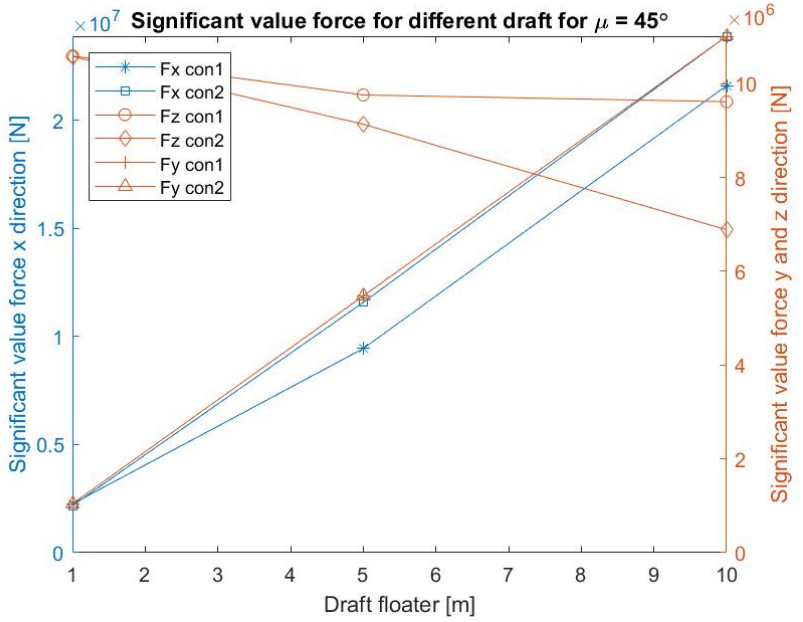

Figure 6.29: Comparison of significant value of the forces in the connections for case 1.3 for 45° wave direction

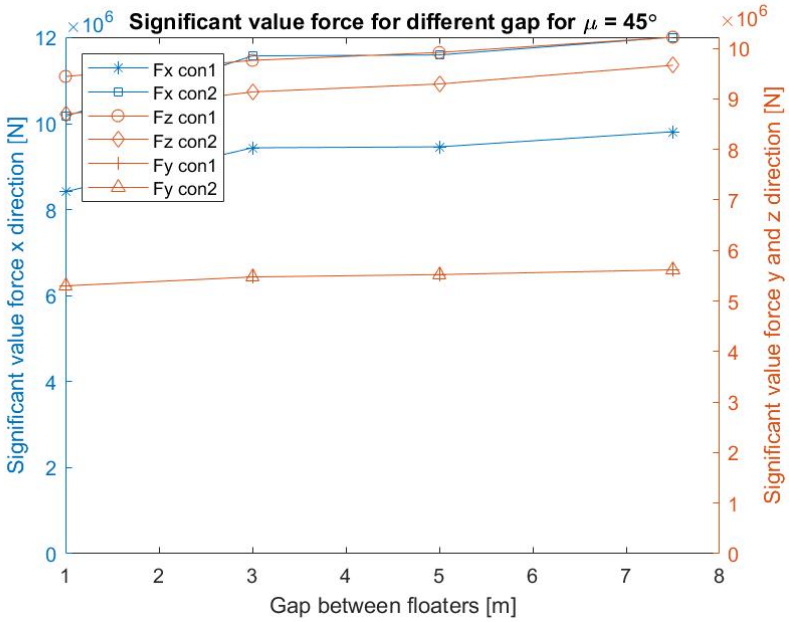

Figure 6.30: Comparison of significant value of the forces in the connections for case 1.4 for 45° wave direction

Chapter 7 Case 2: varying the connection stiffness

In the second case study, the stiffness of the connections between the floaters is varied. In this case study, the influence of the compliance of the connection on the forces in the connection and motions of the floater is studied. Case 2 is separated into 4 subcases. In case 2.1, four different connection stiffness in the axial direction (x direction) of the connection are tested, in case 2.2 the shear stiffness is varied (y and z direction), in case 2.3 the bending stiffness is varied (θ and ψ rotation) and in case 2.4 the torsional stiffness is varied (ϕ rotation). For every sub-case the wave direction for 0° and 45° is applied. Again, the 0° wave direction is defined as traveling towards positive x. For this case, the same configuration as seen in figure 6.1 is used. The length L is set at $100m$, the width, B, is $35m$, the draft, T, is $5m$ and the gap between the floaters, d, is set at $3.5m$. For this configuration a total of 735 panels is required, therefore the target number of panels in NEMOH is set at 400, which is more than half the required number of panels. Furthermore, the irregular frequency removal method as well as the gap resonance suppression as explained in sections 4.1.4 and 4.1.5 is applied.

7.1 Case 2.1: axial stiffness

In case 2.1 the axial connection stiffness is varied, while the rest of the stiffness and dimensions stay the same. The axial stiffness is defined as the stiffness in x direction k_x. The stiffness in all other directions is set at $k = 10^7 N/$ or Nm/rad. The following subcases are created for case 2.1:

Table 7.1: List of subcases for case 2.1

Casenumber	$k_{axial}[N/m]$	$k_{shear}[N/m]$	$k_{bending}[N/rad]$	$k_{torsion}[N/rad]$	Wave directions [°]
2.1.1	0	10^7	10^7	10^7	[0, 45]
2.1.2	10^4	10^7	10^7	10^7	[0, 45]
2.1.3	10^7	10^7	10^7	10^7	[0, 45]
2.1.4	10^{10}	10^7	10^7	10^7	[0, 45]

As in case 1, the forces occurring in each of the joints for wave frequencies from 0 to $2rad/s$ for each stiffness are then compared. Figure 7.1 shows the results as a force energy density spectrum for the 0° wave direction. Figure 7.2 shows the results for the 45° wave direction. In both figures only results for connection 1 are shown, to illustrate the effects on the connections in every direction. In figures 7.3 and 7.4 the significant force in each direction for different stiffness are shown for both wave directions. The significant force can be found using the force energy density spectrum as explained in section 4.2.4.

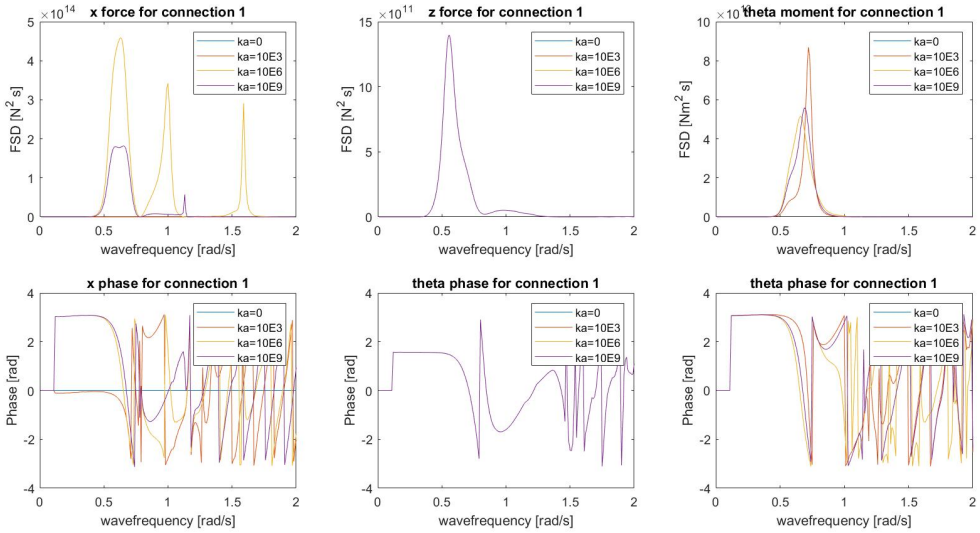

Figure 7.1: Horizontal, vertical and rotational force spectra in first connection for case 2.1 for 0° wave direction

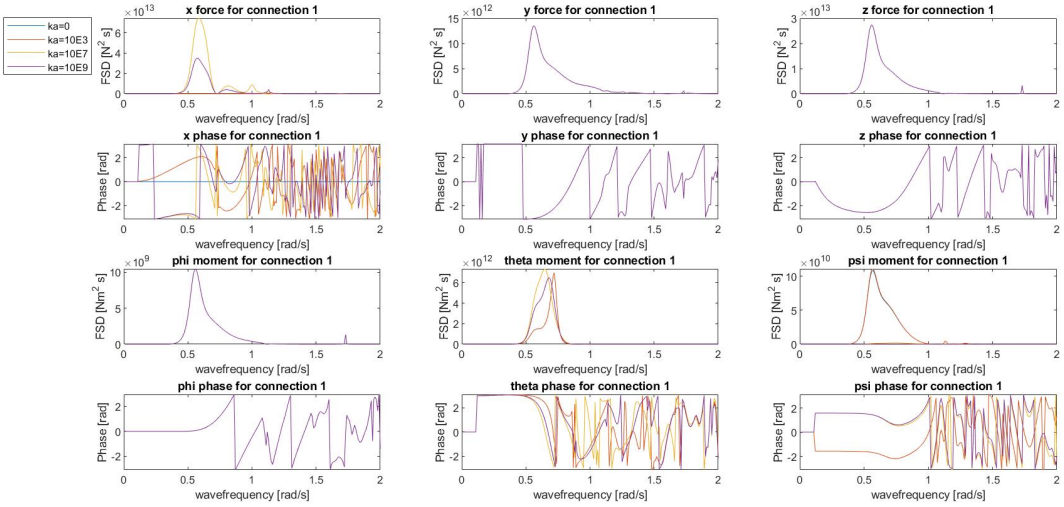

Figure 7.2: Horizontal, vertical and rotational force spectra in first connection for case 2.1 for 45° wave direction

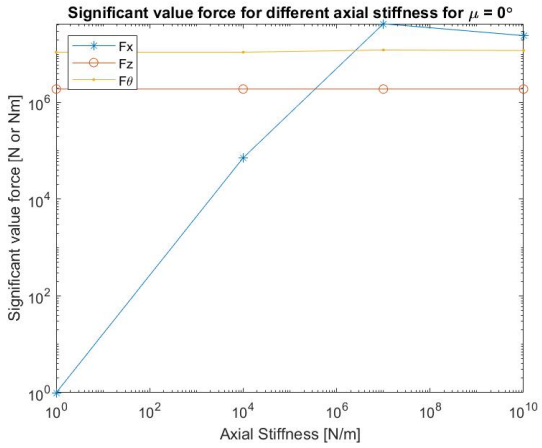

Figure 7.3: Significant value of the force spectra in the first connection for case 2.1 for 0° wave direction

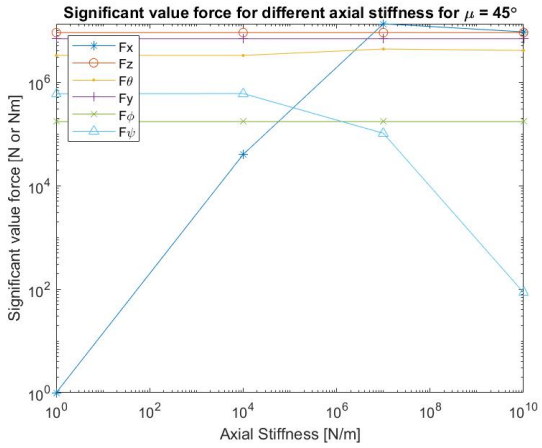

Figure 7.4: Significant value of the force spectra in the first connection for case 2.1 for 45° wave direction

Figure 7.3 shows that a difference in axial stiffness doesn't influence the forces in other degrees of freedom. As can be seen the significant force stays the same in all other directions. The force in axial direction gradually increases towards a certain treshold, this is because the connection functions more like a fully stiff connection that fully constrains the relative motion of the floaters. This is also the reason why the significant force of the axial force for a stiffness of $10^7 N/m$ is higher than for $10^{10} N/m$, because for that stiffness there is more relative motion possible between the floaters and the motion is not yet fully constraint, however the stiffness is very large so this gives large forces in the joint. In the 45° wave direction it shows that the axial stiffness also decreases the force in bending in ψ direction. This is because increasing stiffness in axial direction, decreases the possible rotation of the barge around the z-axis, while the rotational stiffness in this direction stays the same. It is also shown that there is no to little influence on the forces in the other degrees of freedom.

Figures 7.1 and 7.2 shows that the axial stiffness does have an influence on the frequency at which peaks occur in the wave spectrum for the rotation about the y axis for a 0° and 45° wave direction. For the lower stiffness the rotational degree of freedom has the peak at a higher frequency and a narrower spectrum than for a stiffer connection, so the total zeroth order moment and thus the significant force does increase or decrease little to none, but the shape of the force spectrum changes a lot for the pitch rotation for increasing axial stiffness. The phase of the force changes a lot at higher frequencies and the plot becomes messy. This phenomenon also occurred in the previous cases can be partially explained by the partial suppression of the gap resonance and because of small irregularities in the removal of irregular frequencies. However, due to the energy in the spectrum at high frequencies being very low, the higher frequencies in the phase plots is of less importance.

7.2 Case 2.2: shear stiffness

In case 2.2 the shear connection stiffness is varied, while the rest of the stiffness and dimensions stay the same. The shear stiffness is defined as the stiffness in y and z direction k_y and k_z. The stiffness in all other directions is set at $k = 10^7 N/m$ or Nm/rad. The following subcases are created for case 2.2:

Table 7.2: List of subcases for case 2.2

Casenumber	$k_{axial}[N/m]$	$k_{shear}[N/m]$	$k_{bending}[N/rad]$	$k_{torsion}[N/rad]$	Wave directions [°]
2.1.1	10^7	0	10^7	10^7	[0, 45]
2.1.2	10^7	10^4	10^7	10^7	[0, 45]
2.1.3	10^7	10^7	10^7	10^7	[0, 45]
2.1.4	10^7	10^{10}	10^7	10^7	[0, 45]

Again the same plots are created as in case 2.1. A comparison is made between the forces in the connection for the different stiffness. For the 0° case the resulting force spectra can be found in figures 7.5 for the first connection. For the 45° case the resulting forces can be found in figure 7.6. Furthermore, the significant force plots can be found in figure 7.7 and figure 7.8.

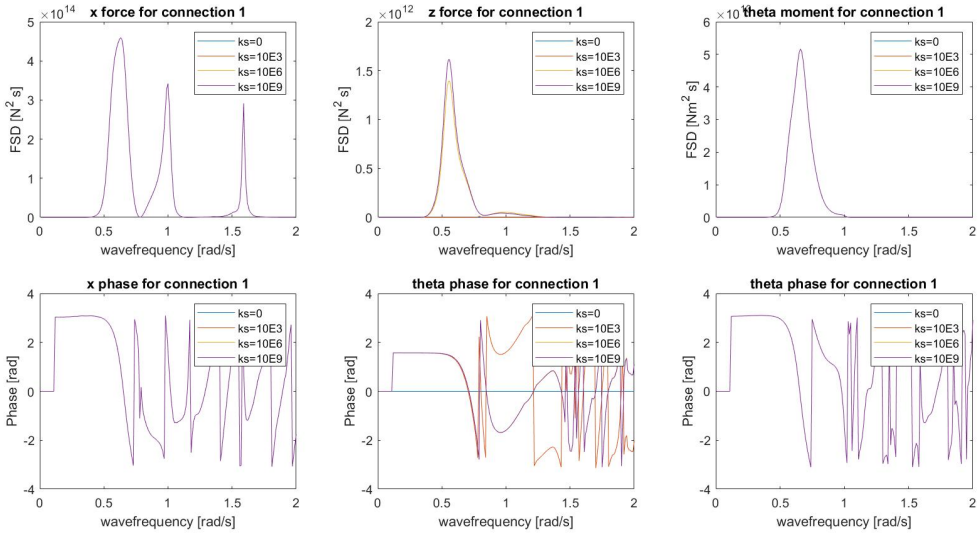

Figure 7.5: Horizontal, vertical and rotational force spectra in first connection for case 2.2 for 0° wave direction

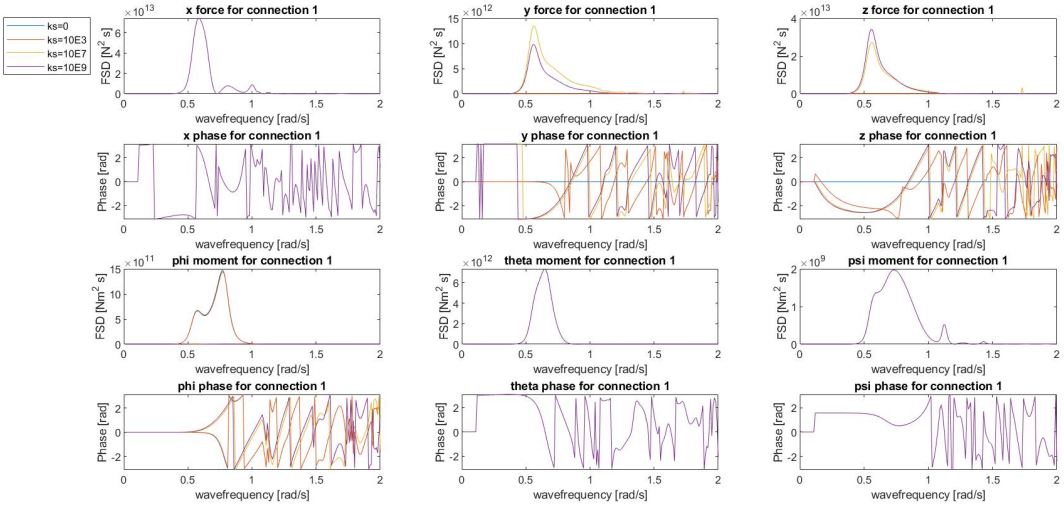

Figure 7.6: Horizontal, vertical and rotational force spectra in first connection for case 2.2 for 45° wave direction

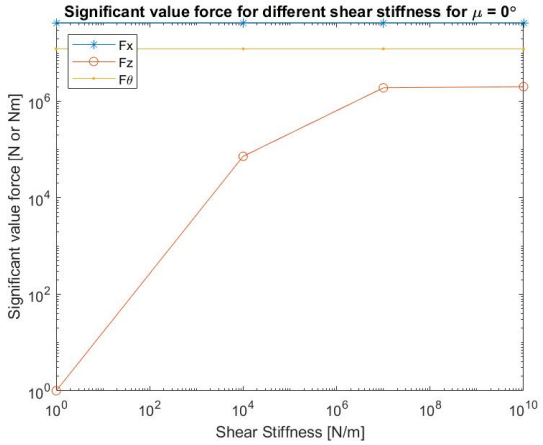

Figure 7.7: Significant value of the force spectra in the first connection for case 2.2 for 0° wave direction

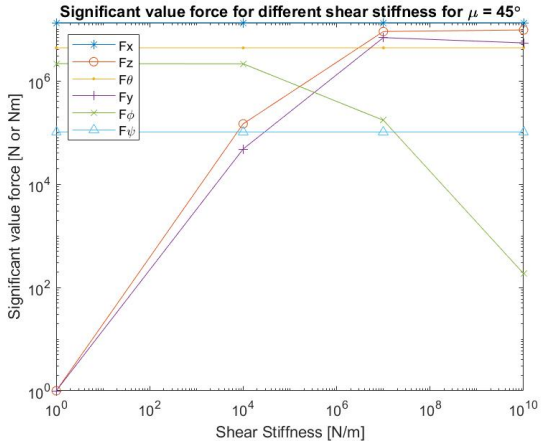

Figure 7.8: Significant value of the force spectra in the first connection for case 2.2 for 45° wave direction

As in case 2.1, the stiffness in shear direction only influences the degree of freedom it operates in for the 0° wave direction. Furthermore, the significant value of the force spectrum increases to an asymptote as the stiffness increases. For the 45° wave direction the rotational degree of freedom that is counteracted by the stiffness in shear decreases. In particular the stiffness in z-direction counteracts the rotation about the x-axis of the floater, so with an equal stiffness in that direction the force and thus the significant value of the force decreases. As also shown in figure 7.8, the significant value in y direction also increases towards an asymptote.

The connection stiffness in shear direction does not influence any other degree of freedom as can be seen in figure 7.5 and 7.6. The shape of the force spectra stays the same in the x, θ and ψ direction. As for the previous cases, phase of the force changes a lot at higher frequencies and the plot becomes messy. Due to the energy in the spectrum at high frequencies being very low, the higher frequencies in the phase plots is of less importance.

7.3 Case 2.3: bending stiffness

In case 2.3 the bending stiffness is varied, while the rest of the stiffness and dimensions stay the same. The bending stiffness is defined as the rotational stiffness in θ and ψ direction k_θ and k_ψ. The stiffness in all other directions is set at $k = 10^7 N/m$ or Nm/rad. The following subcases are created for case 2.3:

Table 7.3: List of subcases for case 2.3

Casenumber	$k_{axial}[N/m]$	$k_{shear}[N/m]$	$k_{bending}[N/rad]$	$k_{torsion}[N/rad]$	Wave directions [°]
2.1.1	10^7	10^7	0	10^7	[0, 45]
2.1.2	10^7	10^7	10^4	10^7	[0, 45]
2.1.3	10^7	10^7	10^7	10^7	[0, 45]
2.1.4	10^7	10^7	10^{10}	10^7	[0, 45]

Again the same plots are created as in case 2.1. A comparison is made between the force energy spectra in the connection for the different stiffness. For the 0° case the resulting forces can be found in figures 7.9 for the first connection. For the 45° case the resulting forces can be found in figure 7.10. Furthermore, the overview of the significant value of the force spectrum can be found in figures 7.11 and 7.12.

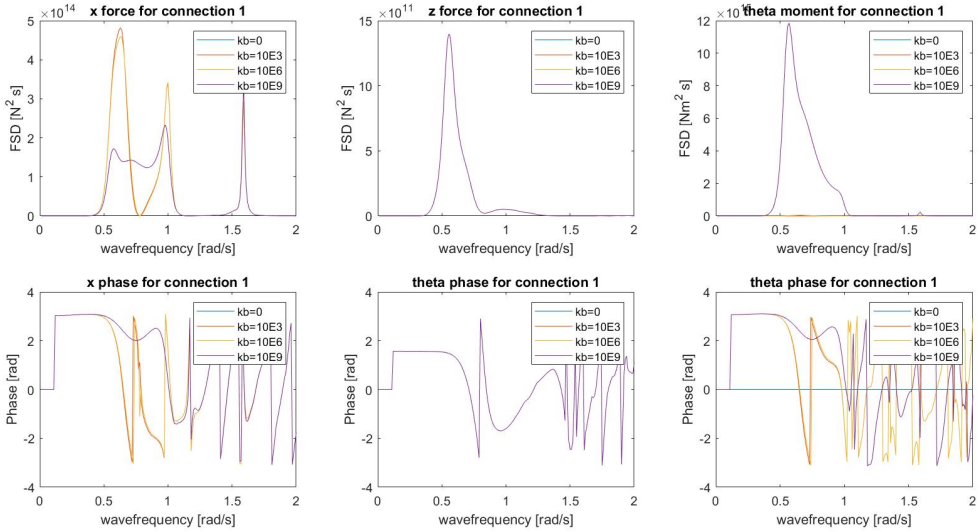

Figure 7.9: Horizontal, vertical and rotational force spectra in first connection for case 2.3 for 0° wave direction

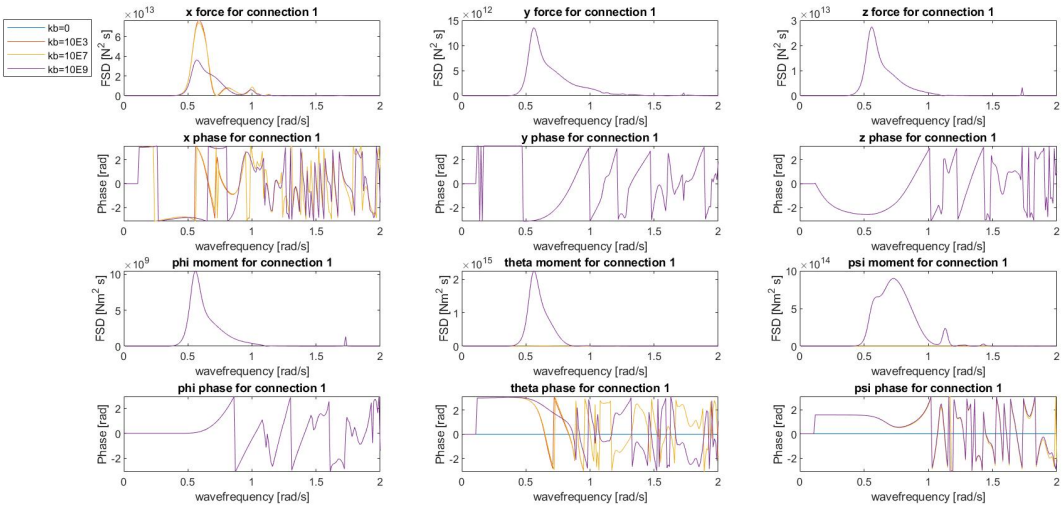

Figure 7.10: Horizontal, vertical and rotational force spectra in first connection for case 2.3 for 45° wave direction

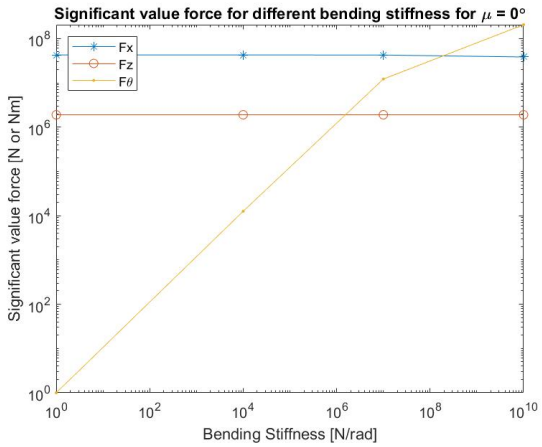

Figure 7.11: Significant value of the force spectra in the first connection for case 2.3 for 0° wave direction

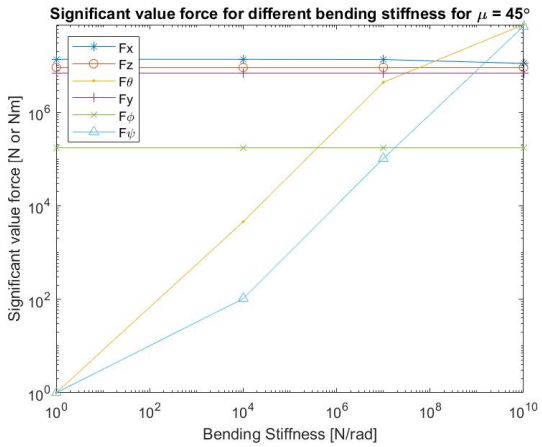

Figure 7.12: Significant value of the force spectra in the first connection for case 2.3 for 45° wave direction

It can be concluded that varying the bending stiffness almost only influences the significant forces in bending, $F\theta$ and $F\psi$. It has a slight influence on the force in x direction. When looking at the shape of the force spectrum in figure 7.9, it can be seen that the bending stiffness however does have a large influence on the shape of the spectrum. The maximum force in x direction is much larger for a bending stiffness of $10^4 Nm/rad$ and $10^7 Nm/rad$, but decreases to almost zero around a frequency of $0.8 rad/s$. For a stiffness of $10^{10} Nm/rad$ the spectrum doesn't decrease to almost zero for that frequency, but the maximum force is smaller and thus the zeroth order moment of that spectrum and therefore the signicant force is quite similar. This seems also the case for the 45° wave direction.

What is also shown in the figures is that for the used stiffness of the connection, significant value of the force does not gradually converge towards an asymptote as seen in the previous two subcases. Furthermore, the bending stiffness only influences the rotational direction it operates

in, thus rotation about y and z axis. As for the previous cases, phase of the force changes a lot at higher frequencies and the plot becomes messy. But as for previous cases, due to low energy density at high frequencies, the phase plots at these frequencies are of less importance.

7.4 Case 2.4: torsional stiffness

In case 2.4 the torsional stiffness is varied, while the rest of the stiffness and dimensions stay the same. The torsional stiffness is defined as the rotational stiffness in ϕ direction k_ϕ. The stiffness in all other directions is set at $k = 10^7 N/m$ or Nm/rad. The following subcases are created for case 2.4:

Table 7.4: List of subcases for case 2.4

Casenumber	$k_{axial}[N/m]$	$k_{shear}[N/m]$	$k_{bending}[N/rad]$	$k_{torsion}[N/rad]$	Wave directions [°]
2.1.1	10^7	10^7	10^7	0	[0, 45]
2.1.2	10^7	10^7	10^7	10^4	[0, 45]
2.1.3	10^7	10^7	10^7	10^7	[0, 45]
2.1.4	10^7	10^7	10^7	10^{10}	[0, 45]

Again the same plots are created as in case 2.1. A comparison is made between the forces in the connection for the different stiffness. For the 0° case the resulting force spectra can be found in figure 7.13. For the 45° case the resulting force spectra can be found in figure 7.14. The graphs showing the significant value of each spectrum of the subcases can be found in figure 7.15 and figure 7.16.

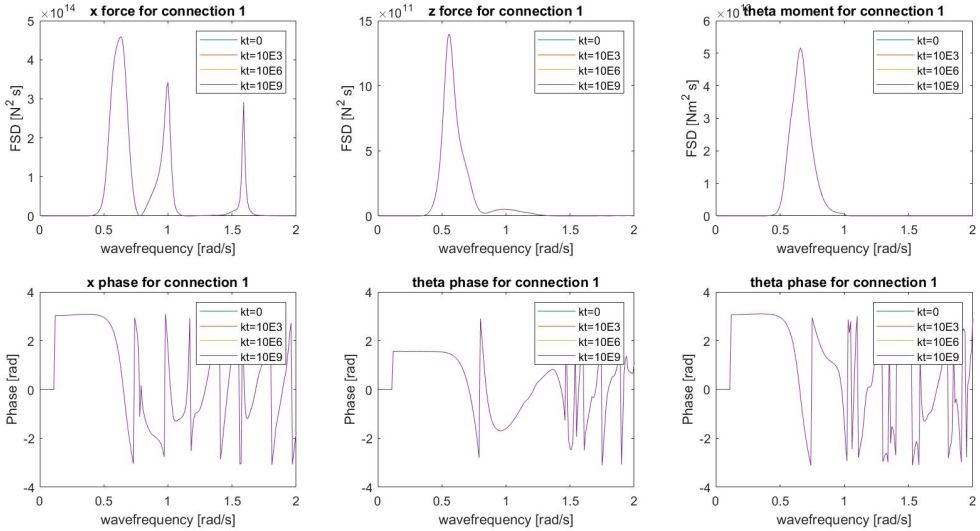

Figure 7.13: Horizontal, vertical and rotational force spectra in first connection for case 2.4 for 0° wave direction

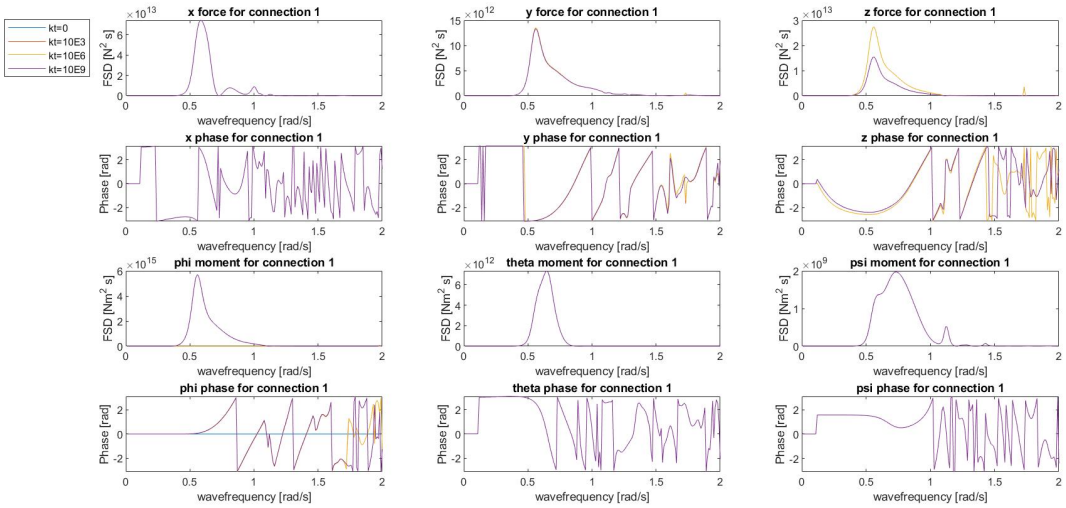

Figure 7.14: Horizontal, vertical and rotational force spectra in first connection for case 2.4 for 45° wave direction

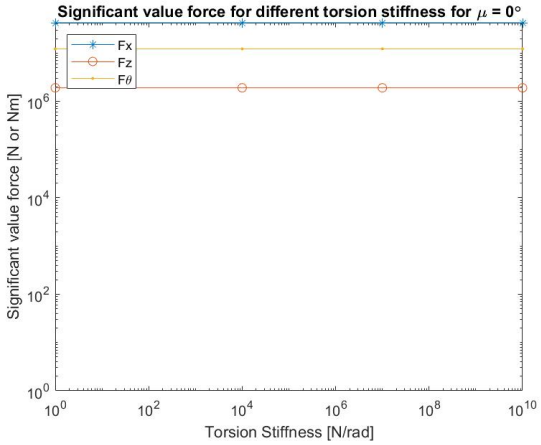

Figure 7.15: Significant value of the force spectra in the first connection for case 2.4 for 0° wave direction

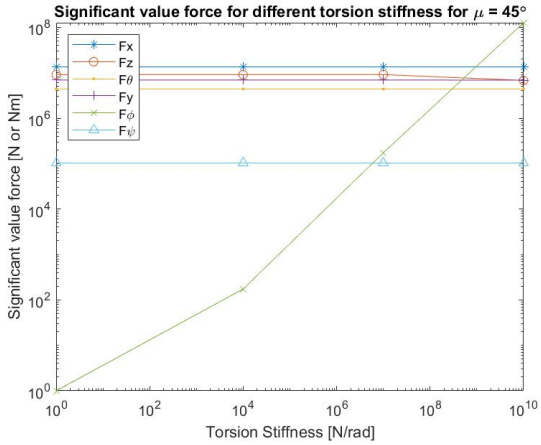

Figure 7.16: Significant value of the force spectra in the first connection for case 2.4 for 45° wave direction

As shown in the figures, the torsional stiffness doesn't influence the significant value of the force for the 0° wave direction as well as the shape of the spectra for this wave direction. This is due to the 0° waves not influencing the rotation about the x axis. Figure 7.16 shows that the torsional stiffness only influences the significant value of the spectrum for rotation about the x axis and the vertical force in z direction. The rest stays the same. As can be seen in figure 7.14 the maximum force in z direction is higher for a stiffness of $10^4 Nm/rad$ and $10^7 Nm/rad$ than for $10^{10} Nm/rad$. This can be explained because the relative rotational movement of the floaters around the x axis is decreased for increasing stiffness in that rotational direction, this decreases also the relative vertical movement at the connection point while the stiffness in z direction stays the same. The forces in x, y, θ and ψ are not influenced by the torsional stiffness. In figure 7.13 and 7.14 it is shown that changing the torsional stiffness is has little influence on the phase of the force, the phase stays the same for the 0° wave direction.

7.5 Overview Case 2

A full overview of the results from case 2 are shown below. The data shown is the significant value of the force spectrum for each different case for the wavespectrum with a 50 year return period. Figure 7.17 shows the results for the 0° wave direction and figure 7.18 show the results for the 45° wave direction. Only the relevant results are shown for each wave direction. Each marker represents a calculated significant value of the force spectra for the different subcases. A dash in the annotation means every stiffness up to and included stiffness has the same significant value.

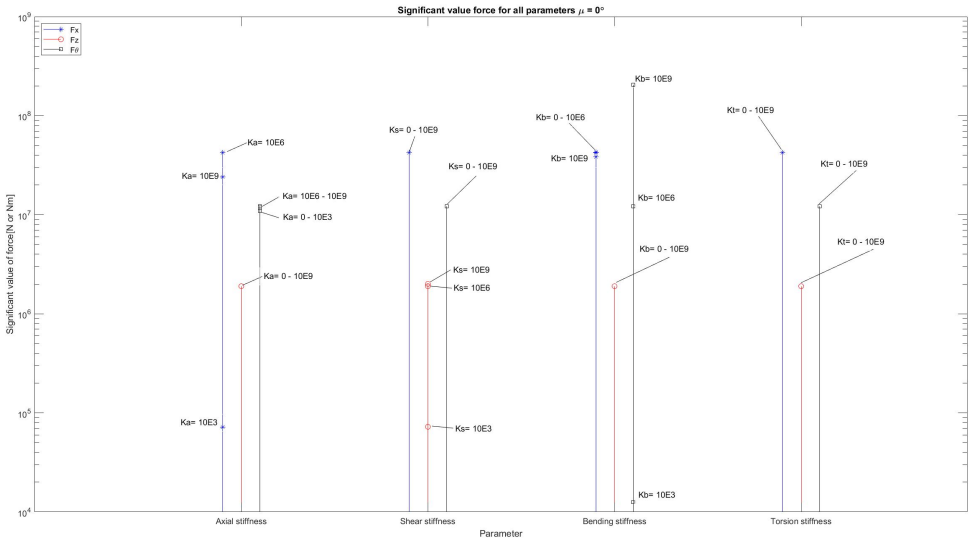

Figure 7.17: Comparison of significant value of the forces and moments in first connection for case 2 for 0° wave direction

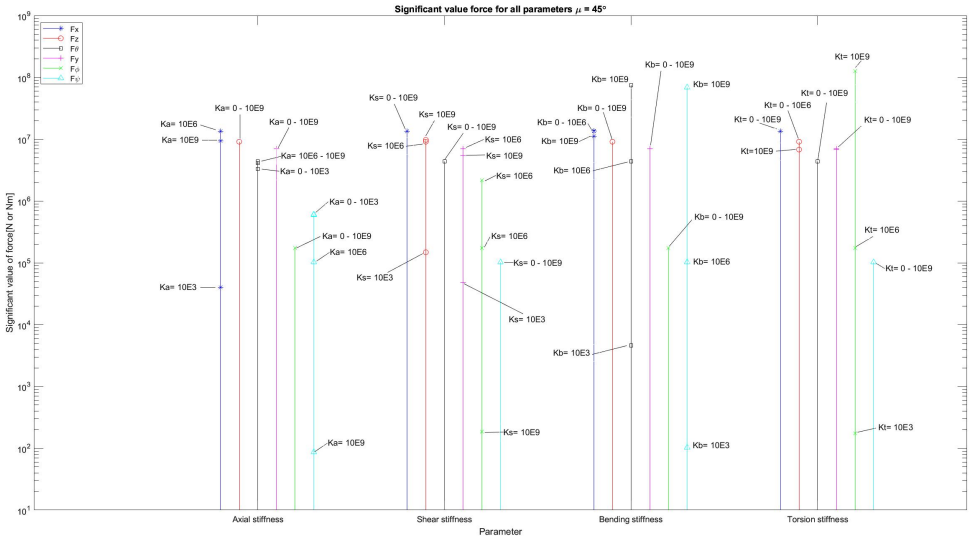

Figure 7.18: Comparison of significant value of the forces and moments in first connection for case 2 for 45° wave direction

7.6 Comparison between connections for $\mu = 45°$

As for case 1, a comparison is done between the forces in both connections for the 45° wave direction for different connection stiffnesses. As can be seen in figure 7.19 there is not much difference in force between the connections for different axial stiffness, except for the force in x direction. The difference between the force in connection 1 and 2 increases for increasing axial stiffness. This phenomenon also occurs when changing the shear stiffness, but the difference in force increases less significantly as can be seen in figure 7.20. Furthermore, in the graphs where the shear, bending and torsion stiffness is changed, the force in x direction is still higher for the second connection with regard to the first connection, also the force in z direction differs a little. As seen in figure 7.21 and figure 7.22, a change in rotational stiffness does not influence the significant force in any rotational direction between the first and second connection.

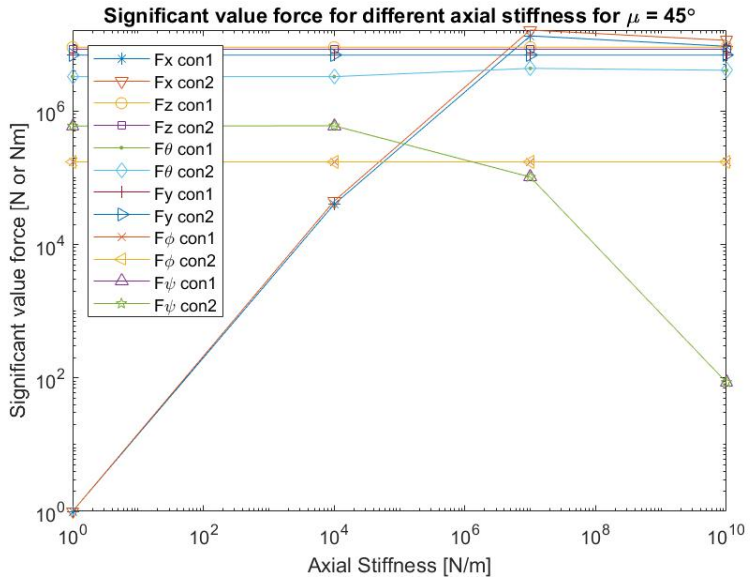

Figure 7.19: Comparison of significant value of the forces in the connections for case 2.1 for 45° wave direction

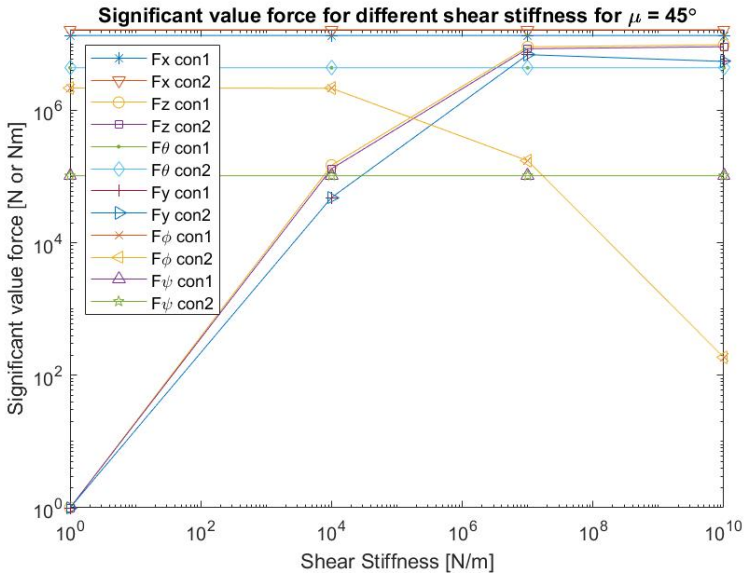

Figure 7.20: Comparison of significant value of the forces in the connections for case 2.2 for 45° wave direction

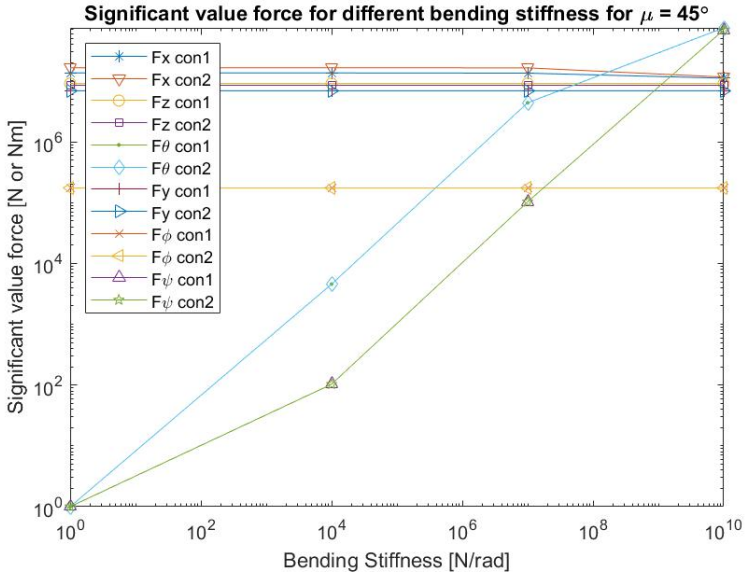

Figure 7.21: Comparison of significant value of the forces in the connections for case 2.3 for 45° wave direction

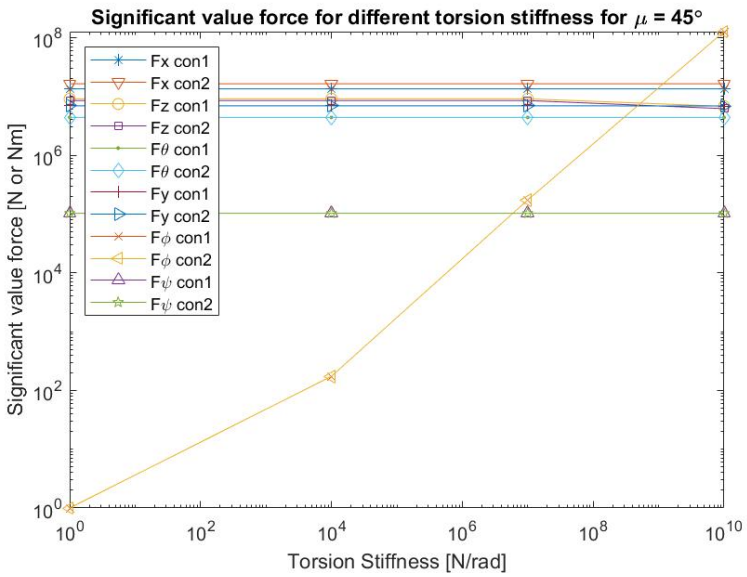

Figure 7.22: Comparison of significant value of the forces in the connections for case 2.4 for 45° wave direction

Chapter 8 Discussion

In this chapter the research is discussed and limitations of the applied model and assumptions are further investigated and discussed. At the end, suggestions for further research are given.

8.1 Model

This research is focused on the difference in floater motions and resulting connection forces for different sizes and connection stiffness of offshore floating solar platforms. This is done by developing a numerical model for two rectangular floaters with connections between the floaters at each end. The motions and forces are calculated using the equation of motion for the floater combination in the frequency domain. From the motion, the resulting connection forces can be computed. The resulting motions and forces are validated using previously made models by Sun et al. [18] and Newmann [46]. After validation, 2 case studies were performed. The first focuses on the floater dimensions. The second on the stiffness of the connection between the floaters. The different aspects of the model and their respective limitations can be divided into several parts, which are discussed hereafter:

- The application of potential theory
- Structural model
- Irregular frequencies
- Gap resonance
- Viscous Damping
- Joints
- Joint stiffness

8.1.1 Potential theory

In this research, the hydrodynamic interaction between the waves and the rectangular floater is modelled using the boundary element method in the software NEMOH. The boundary element method uses the potential theory to solve the radiation and diffraction problems and the wave excitation forces. This results for the two rectangular floaters in a 12x12 matrix describing the added mass, damping, and complex wave excitation for each frequency. The floaters are meshed using the NEMOH internal meshing software and implemented in the NEMOH software together with the used wavefrequencies, wavedirection and waterdepth. The results from this boundary element method software are then used in the frequency domain to compute the motion and forces of the floaters. In order to get accurate results, the number of panels that are used in the mesh should be correctly chosen. The number of panels is dependent on the total wetted surface of the structure and the maximum occurring wavelengths that are taken into account, for this studies the maximum wavelength taken into account is $\omega = 2rad/s$.

Potential theory and the calculation in frequency domain has some assumptions and limitations. First of all, the used model only takes into account first order wave forces. Higher order wave forces are not taken into account. However, when the mooring forces have to be calculated, these second order wave forces should be taken into account [43]. Non-linear effects like wave breaking and overtopping of the waves are not taken into account. Therefore, the calculated forces and

motion should be treated with care and further scale model tests are needed to compute the exact motion and forces of the structure and connections. The calculation in the frequency domain requires a linearization of the problem, thus non-linear effects in the joints and of the structure are neglected. Such non-linear effects include the viscous damping effects, change in wave excitation forces due to change in orientation of the floater with regards to the incoming wave direction and the second order wave loads.

8.1.2 Structural model

The structural model as chosen in this research considers only fully rigid bodies. Thus potential flexibility of the floaters is not taken into account in this research. The effect of flexibility was initially included in this research, but due to time constraints not further executed. It is expected that, for the dimensions chosen in this work, flexibility of the floater will play a role in the motions of the floaters and the forces on the connections between the floaters. Newmann [46] shows this where a barge of length L=80m, width B=10m and draft of T=5m is considered a slender structure where flexibility needs to be taken into account. The dimensions used in this study are of the same order of magnitude. It is important that this aspect of flexibility of the floaters is taken up in future research. However, the used structural model is still relevant to give an initial insight in the relative motion of interconnected offshore floating platforms and in the difference in forces in the connections between the floaters for different design choices regarding the dimensions of the floater and connection stiffness.

8.1.3 Irregular frequencies

In this studies NEMOH is used, to calculate the hydrodynamic coefficients and wave excitation forces on the structure. With the use of NEMOH the irregular frequency phenomenon occurs. As explained, NEMOH doesn't have a tool to remove irregular frequencies from the results, thus this is done during the post processing in the model. In order to investigate the influence of the irregular frequency removal on the forces in the joint, the irregular frequencies are not removed for one test case. The irregular frequencies occur for most cases at higher frequencies than the occurring wave spectrum, so this doesn't have much influence on the calculated force spectra for most cases. However, as the frequencies at which irregular frequencies occur are dependent on the length, the width and draft of the structure these irregular frequencies shift more towards lower frequencies for some cases. For example, for case 1.3, where the draft is changed, for the 10m draft, the first irregular frequency is found at around $\omega = 1.13 rad/s$, which is very much in the range of the occurring wave spectrum. To investigate the influence of these irregular frequencies on the results, the irregular frequencies are not removed for the case with $\mu = 0°$ and the results are then compared to the results shown in section 6.5. In table 8.1 the calculated significant force for both cases are compared. As can be seen, for the occurring wave spectrum where most of the energy lies in beneath $\omega = 1.5 rad/s$ the removal of irregular frequencies doesn't influence the results that much, however it does give slightly higher results in the force in x-direction due to a small resonance peak occurring at $\omega = 1.13 rad/s$. In figure 8.1 the removal of irregular frequencies can clearly be seen in the phase of the force. At the irregular frequencies, there are high peaks occurring due to the irregular frequencies. However, as the irregular frequencies are not a physical phenomenon, this should be left out of the results. In figure 8.1 in the amplitude plot the orange and blue plots are exactly the same.

Table 8.1: comparison significant force without irregular frequency removal and with irregular frequency removal

Parameter	without removal	with removal
Fsig x-dir	$4.961 \cdot 10^7 N$	$4.960 \cdot 10^7 N$
Fsig z-dir	$7.202 \cdot 10^6 N$	$7.202 \cdot 10^6 N$

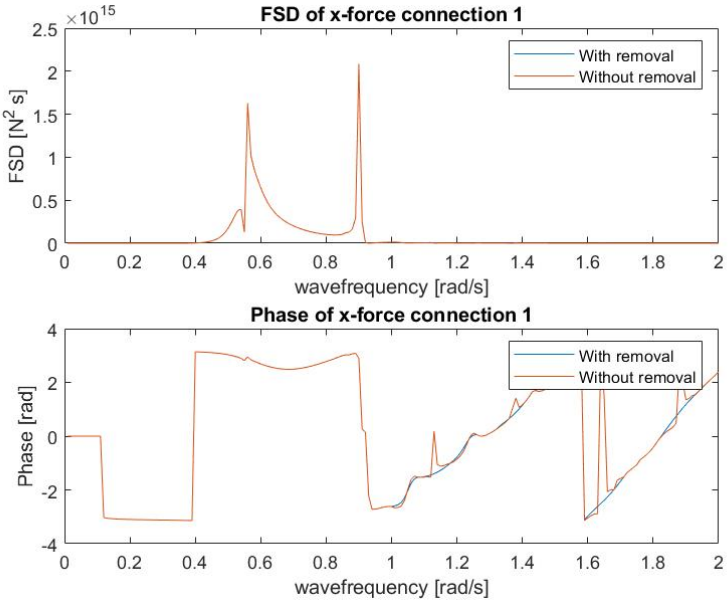

Figure 8.1: Comparison of force spectral density and phase of force in x direction for case 1.3.3 without irregular frequency removal and with irregular frequency removal

8.1.4 Gap resonance

In the post processing of the results, gap resonance is also suppressed. The resonance peaks of the wave elevation in the gap is much higher in the numerical model than it would be in real life due to no wave breaking and no overtopping of waves in the numerical model. The used potential theory model NEMOH doesn't have a tool or function that can deal with unrealistic high resonance in the gap. Therefore this phenomenon is dealt with in the post processing of the results. The frequency at which gap resonance occurs can be estimated using equation 4.7 and 4.8 from section 4.1.5. In the post-processing, the real frequencies at which gap resonance occurs are found by finding the peaks near the estimated gap resonance frequencies, after which the top of the peak is excluded and interpolation is done between the two points that are not excluded from the graph. The sensitivity of this method on the force calculation is investigated and analysed in section 4.1.6. It is concluded in this analysis that the gap resonance peaks differ in height and width for different dimensions of the floater and gap. For this studies it is chosen to only remove the sharp peaks and leave some of the resonance in the graph to represent the real world scenario. However, this method must be further analysed and validated using real world experiments in order to verify that this method represents the real world scenario. Unfortunately this is beyond the scope of this research, as this research is mainly about finding the differences in forces for different floater sizes and connection compliance, but in further research this phenomenon should be further analysed in order to obtain more accurate results for the forces in the connection.

8.1.5 Viscous damping

When using the boundary element method that uses the radiation and diffraction method to calculate the hydrodynamic coefficients, additional pitch damping (for this studies it is in pitch direction, normally reffered as roll damping) is not taken into account [55]. The viscous effects that cause this damping are non-linear effects and therefore not taken into account in this study. However, the influence of additional damping due to viscous effects on the forces between the structures is further investigated using the parameters from the gap resonance sensitivity

analysis and case 1.1.2 as found in table 4.2. The viscous damping coefficient is calculated with the method proposed by Negi and Dhavalikar [55] that gives an estimation of the additional damping. The extra damping is then added in the equation of motion of the structure and the forces within the connection are computed. The additional damping is calculated for a floater of this size at $\beta = 17.84\%$ of the critical damping. This additional damping is than added to the equation of motion for the connected barges and the motion response and forces within the joints are then computed. The results force spectral density and phase in x and z direction for the test case for a wave direction of $\mu = 0°$ is shown in figure 8.2. As seen in the figure, the additional viscous damping in roll influences the force in x direction by narrowing the spectrum. The influence in vertical direction is smaller, however the additional viscous damping give a higher spectral density in z-direction. In table 8.2 the calculated significant force for each of the spectra is displayed. As seen, there is decrease in significant force in x-direction of about 6.5% and an increase in significant force in z-direction of about 3%. Thus, the viscous damping on the structure influences the calculated forces, although this influence is only a few percent. The method used by Negi and Dhavalikar gives an estimation of the additional damping. This additional damping can be further investigated in later studies.

Table 8.2: Comparison significant force without additional viscous pitch damping and with additional viscous pitch damping

Parameter	without damping	with damping
Fsig x-dir	$2.44 \cdot 10^7 N$	$2.28 \cdot 10^7 N$
Fsig z-dir	$2.00 \cdot 10^6 N$	$2.06 \cdot 10^6 N$

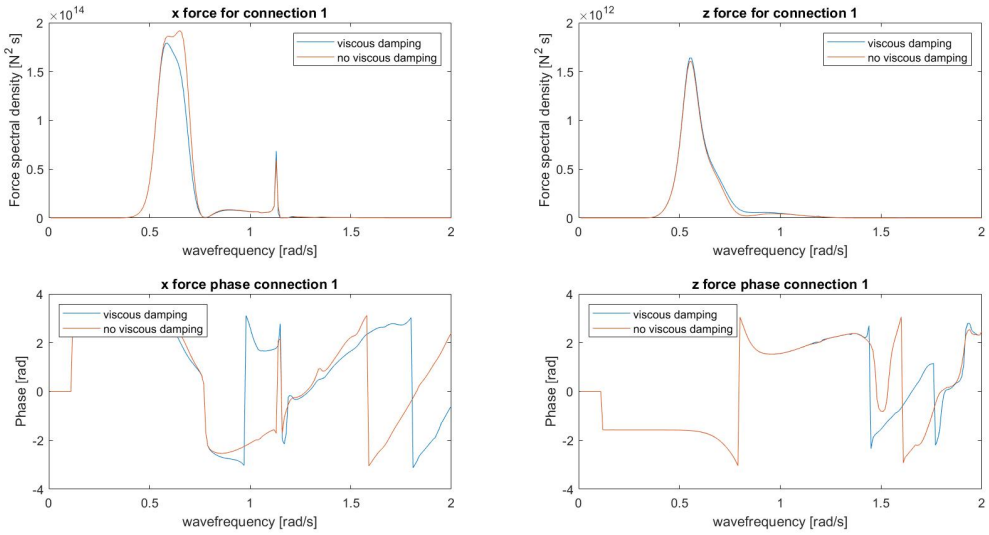

Figure 8.2: Comparison of force spectral density and phase of force in x direction for case 1.1.2 with and without additional viscous damping in pitch

8.1.6 Joints

The connections between the floaters are modelled as three linear translational springs in x, y and z direction and three linear rotational springs in ϕ, θ and ψ direction. This is done in order to simplify the joints and to be able to vary the stiffness of each joint in every direction. The linearization is done in order to be able to compute the joint forces and response of the structure in the frequency domain. Furthermore, no damping is applied in the joints in this studies.

Therefore, the model of the joint is a very simplified model and doesn't take into account some real world phenomena like non-linear effects and inertial effects of the joints. The linearization of the joint stiffness matrix in the equation of motion also assumes small angles. When looking at figure 6.24, it is shown that the pitch angle for this case, which tend to be the biggest angle, is relatively small. Inertial effects in the joints could increase the forces in the joints. In further research, the joint can be modelled more accurately using a finite element model.

In this research the floating solar platforms are only connected by two joints at either end of the floater. The calculated forces of the joints are therefore only applied at either end of the floater. The implementation of more connections should be further investigated. In order to investigate the effect of more than 2 joints between the floaters, the method to calculate the joint stiffness matrix as described in section 4.2.1 could be extended. This will give insight into how the motions and thus connection forces change when applying more connections at different places on the floater. Figure 8.3 shows the difference in connection force for a different location of the joints. The location of the two joints is moved 10m towards the middle of the floater in order to evaluate the influence on the location of the connection with regards to the force in the connection. This is done for a wave direction of $\mu = 45°$ as only moving towards the center in y direction doesn't influence the forces much for $\mu = 0°$. The dimensions of the floater and connection stiffness used for this comparison can be found in table 8.3. As seen in the figure, the vertical force in the connection increases by moving it towards the centerline. The significant value of the force density spectrum increases from $F_{sig,x,notmoved} = 9.44E6$ to $F_{sig,x,moved} = 9.97E6$. The significant value in y-direction stays the same and the significant value in z-direction increases from $F_{sig,z,notmoved} = 9.74E6$ to $F_{sig,z,moved} = 1.21E7$. This is due to the difference in rotation about the x-axis that is counteracted by the connection by a force in z-direction. As the distance between the center of gravity and the connection becomes smaller, this force should be larger in order to have the same moment. There is also a slight difference in force in x-direction. This shows that when applying different locations of the connections the forces will change, thus this should be further investigated in a later stage of the design process when the exact locations of the connection points are known.

Table 8.3: Parameters for joint location test

Parameter	Value	Unit
L	100	m
B	35	m
T	5	m
H	15	m
d	3.5	m
k_{axial}	10E15	N/m
k_{shear}	10E15	N/m
$k_{bending}$	0	Nm/rad
$k_{torsion}$	0	Nm/rad
μ	45	degrees

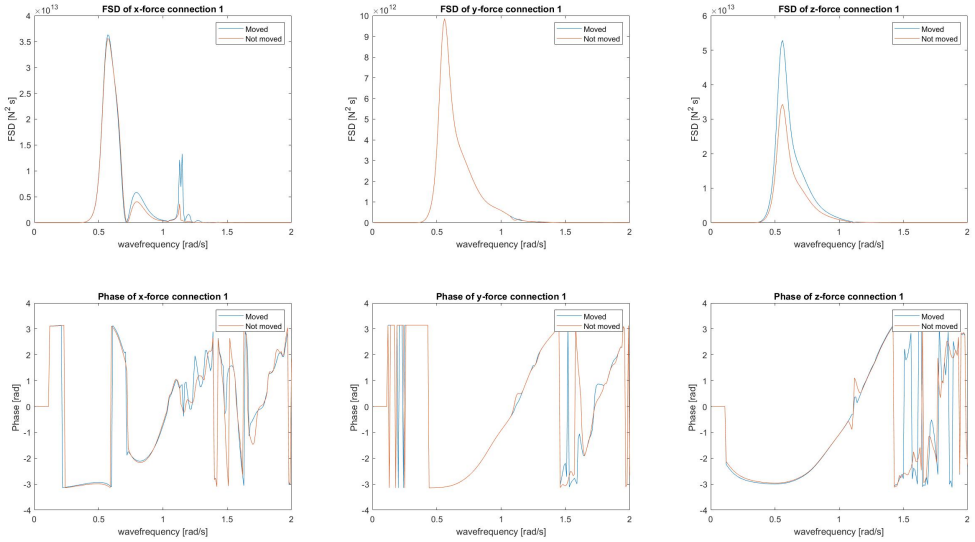

Figure 8.3: Comparison of connection forces between a connection at the ends and connection moved 10m towards the center

8.1.7 Joint stiffness

For case 1, the dimension is varied, for this case the compliance of the connection is chosen as fully stiff in the translational direction with a connection stiffness of $k = 10^{15} N/m$. This assumption gives very small relative displacements at the connection points. This assumption of high stiffness in the joints furthermore restrains the rotational motion around the joint around the x and z axis. In order to see the difference in results for a more realistic compliance of the joints, a comparison is made between the significant force with a connection stiffness in translational direction of $k = 10^7$. This connection stiffness will give higher relative motion at the connection points, however combined with the lower stiffness, this gives a significant force in the same order of magnitude as the fully stiff connection. However, there are some differences in the force spectrum and the significant force for this connection compliance. As seen in figure 8.4 the significant force increases in all three degrees of freedom, furthermore for the largest lengths the increase in x and y direction is even larger for a smaller stiffness. This increase is also seen in the 0° wave direction as seen in figure 8.5. This increase can be explained by looking at the force RAO and phase before it is multiplied by the wave spectrum as seen in figure 8.6. As seen in the figure, there is a big resonance peak in the force in x direction at a frequency around $0.8 rad/s$ for the 250m length floater. Furthermore it is shown that the resonance frequencies for the forces are closer to the applied wave spectrum frequencies for the larger lengths, which give much higher significant forces after the spectral analysis. This phenomenon in x-direction is also seen in when varying in the width of the structure. The force increases significantly in x direction when varying in width. In order to inspect the difference between significant forces for different stiffness in a more convenient way, a stem plot is made where the significant force for the different compliances are compared. These plots are shown in figure 8.7 and figure 8.8 for $\mu = 0°$ and $\mu = 45°$ respectively. As can be seen, the forces for the less stiff connection increase significantly for the 0 degree wave direction, especially in x-direction. for the 45 degree case, the forces increase in x and y direction but decrease in z direction, except for an increase in draft, for smaller draft the significant force is smaller, however for larger draft this significant forces increases a lot. This increase can be mostly explained by resonance frequencies in x and z-direction of the system being closer to the used wave spectrum frequencies for the stiffness of

$k = 10^7 N/m$ than for the stiffness of $k = 10^{15} N/m$. Furthermore, these plots show that for smaller structures, the difference becomes less significant. As seen in figure 8.7 for a length of $50m$ and $100m$ there is not much difference in the significant force in z-direction, however the significant force then increases much more for increasing length.

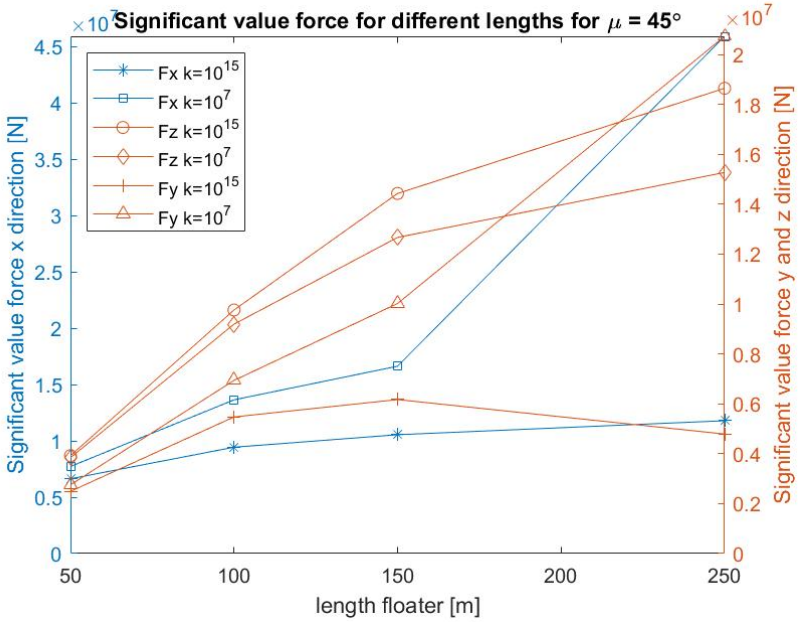

Figure 8.4: Comparison significant forces for different connection stiffness for case 1.1 for $\mu = 45°$ for $k = 10^7 N/m$

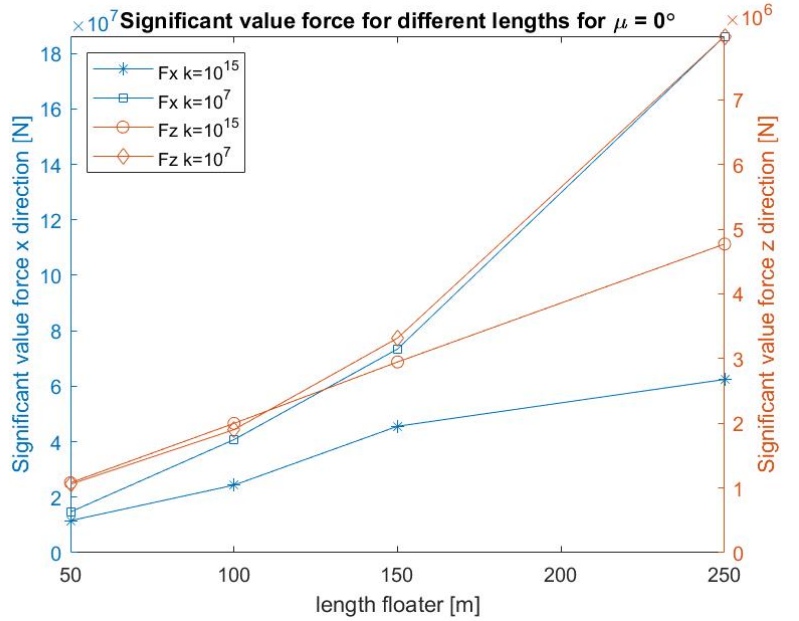

Figure 8.5: Comparison significant forces for different connection stiffness for case 1.1 for $\mu = 0°$ for $k = 10^7 N/m$

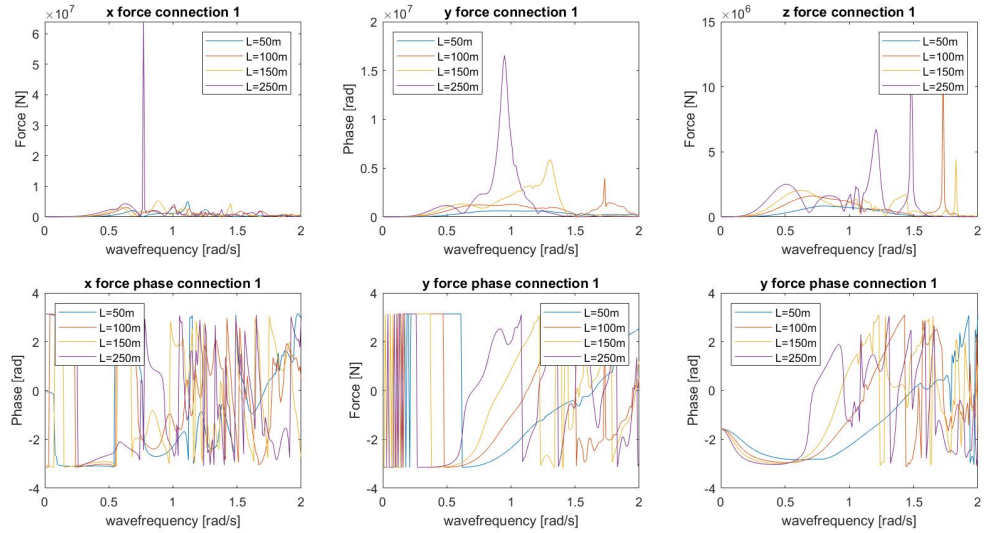

Figure 8.6: Force RAO and phase in translational directions for case 1.1 for $\mu = 45°$ for $k = 10^7 N/m$

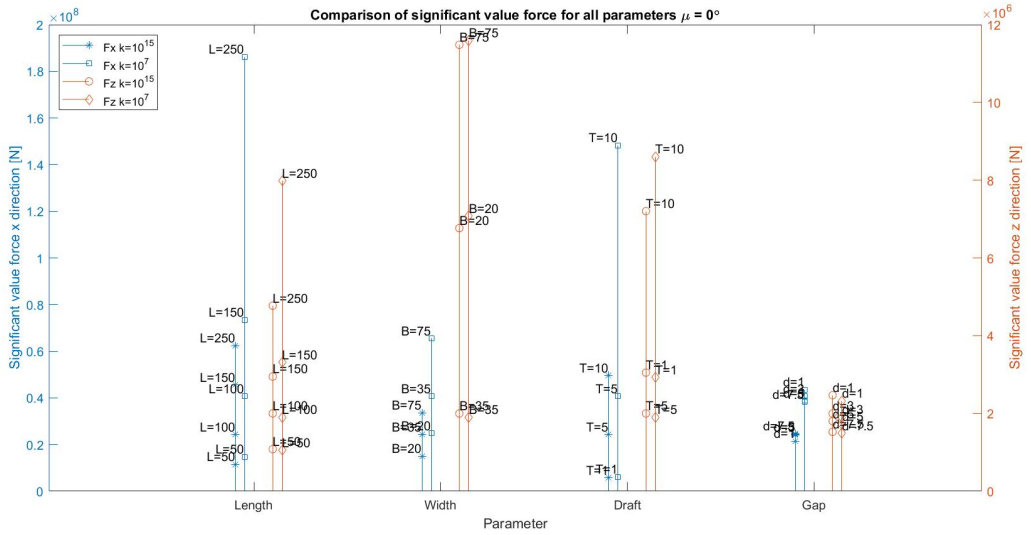

Figure 8.7: Stem plot comparing significant force for different connection stiffness for $\mu = 0°$ for $k = 10^7 N/m$

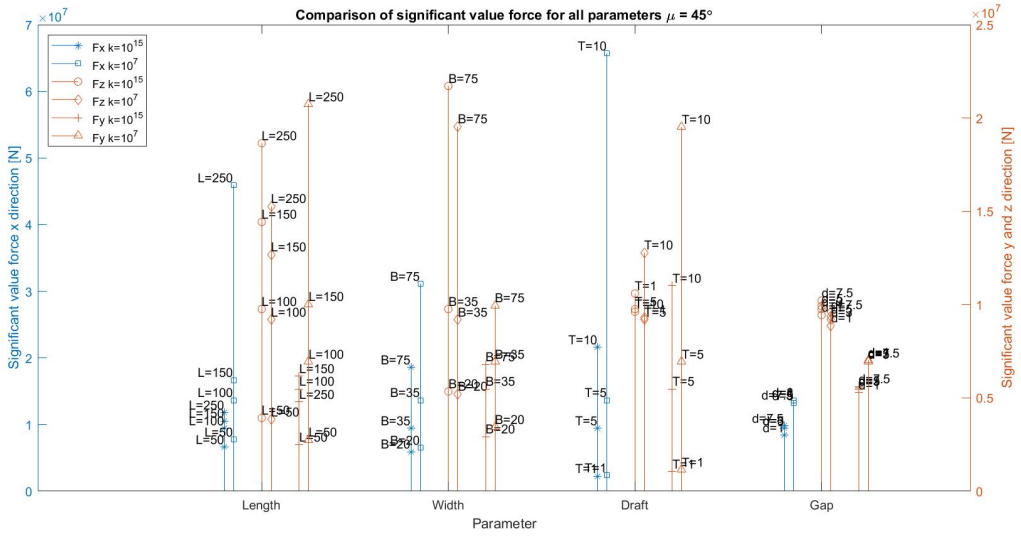

Figure 8.8: Stem plot comparing significant force for different connection stiffness for $\mu = 45°$ for $k = 10^7 N/m$

8.2 Wave spectrum

The results are presented as a force energy density spectrum for each relevant degree of freedom. The computed force energy density spectra are compared using the significant value of the spectrum so that a the interaction between the different design choices and forces and moments within the connections can be quantified. The force energy density spectrum is created for a wave spectrum at the North sea with a return period of 50 years in order to assess the occurring forces for the maximum loads on the structure during its' lifetime. The influence of different design choices regarding size and connection compliance on the structure motions can differ for other wave spectra as the joint reaction forces are a function of the occurring wave frequency. When designing offshore floating PV platforms, other wave energy density spectra should also be investigated.

8.3 Comparison real world connections

In this research, the connections are modelled as a set of springs with a certain stiffness. In order to relate the calculated forces to real world application the calculated significant forces are compared to typical reaction forces of fenders. The forces are compared to super high-capacity QGF QuayGuard fenders from Quayquip [56]. The distance between both platforms is 3.5m therefore, the largest fenders with dimensions of 3.4x7.3m are used for comparison of the forces. For the base case dimensions with $L = 100m, B = 35m, T = 5m$ and $d = 3.5$ the calculated significant force in axial direction for a stiffness of $k = 10^7 N/m$ is the highest and is calculated as $F_{sig,x} = 4.07 \cdot 10^7 N$. The super high capacity fender has a total reaction force at 60% deflection of $8149kN$ according to the company. Thus, a total of 5 of these fenders will be needed at each end of the floater to overcome this significant force in x direction. One thing to highlight is that this is the calculated significant force for a wavespectrum with a return period of 50 years, therefore forces of this magnitude will not occur often.

These types of fenders are often combined with steel wire rope for the full connection. This steel wire rope also needs to be able to overcome the maximum axial force when in tension. To compute how much steel cable is required to overcome the calculated significant force in axial direction in one connection, the modulus of elasticity E is needed of steel wire rope and

the minimum breaking load. These values can be found in [57] and are approximately $E = 1 \cdot 10^5 N/mm^2$ for the modulus of elasticity and a minimum breaking load of approximately $2000 N/mm^2$. Thus, to overcome the axial load of $F_{sig,x} = 4.07 \cdot 10^7 N$ a steel wire of $20350 mm^2$ is needed, which is a radius of $80.5mm$, thus a total diameter of $161mm$ or multiple steel wires with a total area of $20350 mm^2$. One thing to note here is that this is computed without the use of safety factors, thus in real life, more steel wire rope is needed.

8.4 Future research

Further research should take into account flexibility of the floaters. The initial scope of this research was to also investigate the influence of the flexibility of the floater on the motions of the floater and the connection forces. However, due to time constraints, this is not researched in this thesis. Thus, in further research, this aspect should be taken into account.

By using the open source software NEMOH for calculating the hydrodynamic coefficients and wave excitation forces, irregular frequencies as well as unrealistically high gap resonance is present. The irregular frequencies are removed. However, the influence of gap resonance on the behavior and connection forces of the system should be further analysed, as this is not further investigated in this research.

The modelling of the connection between the floaters should be also further investigated. The model of the joints is simplified in this research. In future work, the joints could be modelled using a finite element model in order to take non-linearities and inertial effects of the joints into account. Furthermore, the influence of multiple joints applied at different locations could be analysed.

Because of the calculation in frequency domain, the non-linear effects of the wave-structure interaction can not be taken into account in this research. A time domain model can give more insight into the non-linear effects of the wave structure interaction and their influence on the forces and motions within the system.

In future work, model tests can be used to find the exact forces within the joints and motions of the structure for different waves by taking into account all non-linear effects. This work can then also be used to further verify the model and make adaptations to the model to provide more accurate results.

This model can in later studies also be extended to more than 2 floaters or a grid of floaters. The layout of the floaters will have a big influence on the motions of the system as well as the forces within the joints. Furthermore, the shape of the floaters can be changed to see the influence of the shape of the structure on the motions of the system and the connection forces. Finally, more wave directions can be implemented in the model.

In order to investigate the occurring significant force with for other wave conditions, wave spectra with a shorter return period and thus different sea states can be implemented into the model in order to investigate the influence of sea states on the forces within the connections.

Finally, mooring can be implemented in the model and the influence of mooring on the motion and connection forces should be further analysed. Second-order wave forces can also be taken into account in future work to investigate the mooring demands of different sizes of offshore floating solar concepts.

Chapter 9 Conclusions

In this chapter, the conclusions of this study are discussed. First, the conclusion resulting from the modelling are discussed, after which the conclusions for the separate cases are discussed individually. In the end the answers to the research questions are given.

9.1 Conclusion modelling

In this study, a frequency domain model has been developed in order to investigate the influence of floater size and connection stiffness on the motion of two rectangular floaters and the resulting forces in the connections between the floaters. The hydrodynamic coefficients and wave excitation forces are computed using NEMOH. In the model floating panel size, stiffness, gap size between panels and connector stiffness can be varied and motion results and forces for different wave angles and wave heights can be predicted. The model is validated by comparing results with studies done by Sun et al. [18] and Newmann [46]. Results show excellent agreement, except for a very small difference in roll motion and a difference in vertical motion when rotation in the hinge is allowed. This can be explained by the models' neglection of the viscous damping.

After the validation, the case studies are performed. It can be concluded from these case studies that the modelling technique used in this study can be used for comparing the motions of the floater and resulting forces in the connections. Case 1 shows the influence of floater sizes on the connection forces. Case 2 shows the influence of connection compliance on the connection forces. It should be mentioned that the used model is a simplified linearized model and the effect of non-linearities and flexibility of the floaters on the calculated forces should be investigated in future work.

9.2 Conclusion case 1

From case 1, the following conclusions can be drawn when comparing the results for different lengths, widths, drafts and gap widths.

- In case 1 it is demonstrated that the model can be used to compare the effect of different sizes of the structure on the forces within the joints between the floaters.
- A wave direction of $\mu = 0°$ gives much higher forces in x and z direction than for the $\mu = 45°$ direction. However, for $\mu = 45°$ the force in y-direction isn't negligible anymore.
- An increase in length has more influence on the height of the forces for $\mu = 0°$ than for $\mu = 45°$
- An increase in width can decrease then significant connection force in z-direction because of smaller vertical movement at the connection point due to heave and pitch. An increase in width, gives a higher relative increase in the x and z forces for the 45° wave direction.
- A small draft gives a wider wave spectrum for $\mu = 0°$. A very large draft increases the connection forces significantly.
- The gap width mostly influences the forces in head waves $\mu = 0°$, the influence for $\mu = 45°$ is very small.

9.3 Conclusion case 2

For case 2, the following conclusions can be drawn after comparing the results for different stiffness in different directions.

- In case 2 it is demonstrated that the model can be used to compare the effect of connection stiffness of the joints on the forces within the joints between the floaters.
- The rotational stiffness, bending and torsion, influence the rotational degrees of freedom it operates in the most and have a very small influence on the translational forces. The translational stiffness also influences the rotational degree of freedom. This is due to a decay in relative rotation between the floaters about the axis but the same rotational stiffness of the joint, thus less rotational force (moment) in the joint in that direction. This is seen in the $\mu = 45°$ wave direction as in the $\mu = 0°$ wave direction these rotational forces are negligible.
- The translational stiffness in shear and axial direction increase towards a certain threshold. From a stiffness of $k = 10^7 N/m$ the joint acts as fully stiff in that degree of freedom for shear and bending.
- In Rotational direction the stiffness from which the joint operates as fully stiff is much higher than for the translational stiffness.
- The bending moments increase significantly for increasing stiffness for $\mu = 0°$ and $\mu = 45°$. The torsional moments also increase significantly for increasing stiffness for $\mu = 45°$
- A change in connection stiffness does not influence the difference in force and moment in the two connection for $\mu = 45°$ much.

9.4 Final Conclusion

The created model used in this research can be used to give an indication of the motions of two interconnected floating solar platforms and the forces and moments in the connection points between the floaters. The used boundary element method using NEMOH presented some difficulties due to the occurrence of irregular frequencies and unrealistically high gap resonance. In the model, a method is developed to remove the irregular frequencies and suppress the gap resonance from the hydrodynamic coefficients and wave excitation forces calculated by the NEMOH software. The hydrodynamic coefficients and wave excitation forces are then used to compute the full equation of motion of the system. After the computation of the motion, the corresponding forces and moments of the connections are calculated in the frequency domain. This method proved to be working and the results from the model are similar to the results from literature.

The model is then used to calculate the influence of the dimension of the solar platform on the forces in the connection as well as the influence of the stiffness of the connection on the forces. The study shows how forces on the connections are increased by increasing length, increasing width and increasing draft and what the influence of the connection stiffness and gap width is on this increase for two different wave directions. The model can be used for an initial estimation of floater size and connection stiffness.

For example: at a connection stiffness of $k = 10^7 N/m$ an increase in length increases the forces significantly between lengths of 150m and 250m. In order to keep the forces low, a length of the floater beneath 150m could be recommended. The width has a large influence on the forces in

the connections as well. Based on the calculations a width of around 35m seems to be suitable. A shallow draft increases the force of the connections in z direction for $\mu = 0°$, but decreases the force in x direction. For the chosen connection stiffness, a draft of around 5m would be a suitable option. The gap width mostly influences the force in z-direction, so a larger gap width will reduce the force, however for $\mu = 45°$ this reduction is lost. Thus an initial estimation would be to choose a gap width of around 5m.

This example demonstrates how this research can help give an initial estimation on floater sizes and connection stiffness that would be suitable for application in the North sea. However, model tests will be needed to verify the results from this research and to take non-linear effects into account.

The model shows the interaction between forces and moments in the joints and different design choices regarding size of the floater and compliance of the connections between the floaters. The model and the results of this thesis can be used to give an initial insight into the occurring forces within connections between two floaters and the motions of each of the floater for application in the North sea.

Bibliography

[1] TNO. Unique research into floating solar panels. Consulted on the 27th of May 2021 from https://www.tno.nl/en/focus-areas/energy-transition/roadmaps/renewable-electricity/solar-energy/solar-farm/floating-solar-panels/.

[2] World Bank Group. Where sun meets water, floating solar market report. 2019.

[3] Oceans of energy. A world's first: offshore floating solar farm installed at the dutch north sea. Consulted on the 31th of May 2021 from https://oceansofenergy.blue/2019/12/11/a-worlds-first-offshore-floating-solar-farm-installed-at-the-dutch-north-sea/.

[4] Engineeringnet. Dnv kema lanceert drijvend platform op zee voor zonne-energie. Consulted on the 31th of May 2021 from https://engineeringnet.be/belgie/detail_belgie.asp?Id=8990.

[5] Offshore magazine. Equinor, moss maritime to test floating solar plant. Consulted on the 31th of May 2021 from https://www.offshore-mag.com/renewable-energy/article/14195634/equinor-moss-maritime-to-test-floating-solar-plant-offshore-frya.

[6] Debbie L. Sklar. World's largest solar plant at sea is installed at maldives resort. Consulted on the 31th of May 2021 from https://inhabitat.com/worlds-largest-solar-plant-at-sea-is-installed-at-maldives-resort/.

[7] Oceansun. The institute for energy technology quantifies ocean suns performance gain. Consulted on the 31th of May 2021 from https://oceansun.no/the-institute-for-energy-technology-quantifies-ocean-suns-performance-gain/.

[8] S. Sluijters. Solarduck test nieuwe techniek voor zon op zee. Consulted on the 31th of May 2021 from https://www.change.inc/energie/solar-duck-nieuwe-techniek-zon-op-zee-36193.

[9] A. Andrianov. Hydroelastic analysis of very large floating structures. *Doctoral Thesis, Delft University of Technology*, 2005.

[10] Gyu-Han Lee; Ji-Woong Choi; Ji-Hyun Seo; Hojin Ha. Comparative study of effect of wind and wave load on floating pv: Computational simulation and design method. *Journal of the Korean Society of Manufacturing Process Engineers, vol. 18, no. 11*, October 2019.

[11] Y.Namba M.Ohkusu. Hydroelastic analysis of a large floating structure. *Journal of fluids and Structures, Vol. 19, Issue 4*, pages 543–555, 2004.

[12] A.B.Z. Feys. Support structure for offshore solar: The proposal of a new concept. *Master Thesis, Delft University of Technology*, 2020.

[13] Q.W. Ma and S.Yan. Qale-fem for numerical modelling of non-linear interaction between 3d moored floating bodies and steep waves. *INTERNATIONAL JOURNAL FOR NUMERICAL METHODS IN ENGINEERING, volume 78*, pages 713–756, 2009.

[14] Sofia Caires (Deltares) and Irene Pathirana (Fugro). Hollandse kust (noord) field measurement campaign. *Deltares and Fugro*, pages 48–54, 2019.

[15] Sofia Caires (Deltares) and Irene Pathirana (Fugro). Hollandse kust (noord) field measurement campaign. *Deltares and Fugro*, pages 68–70, 2019.

[16] M. M. Bernitsas. Viscous forces on circular cylinders in separated flows. case study: Cable strumming. *lecture Notes for NA 621*, 1982.

[17] Leo H. Holthuijsen. *Waves in oceanic and coastal waters*. Cambridge University Press, 1st edition, 2007.

[18] L. Sun, R. Eatock Taylor, and P.H. Taylor. First- and second-order analysis of resonant waves between adjacent barges. *Journal of Fluids and Structures*, 26(6):954–978, 2010. ISSN 0889-9746. doi: https://doi.org/10.1016/j.jfluidstructs.2010.06.001.

[19] International Energy Agency. Net zero by 2050: A roadmap for the global energy sector. *summary for policy makers*, 2021.

[20] International Energy Agency. Net zero by 2050: A roadmap for the global energy sector. *Chapter 1*, 2021.

[21] B. Roeffen et al. Reducing global land scarcity with floating urban development and food production. *WWF - Unsustainable fishing*, 2013.

[22] J.A. Palyvos E. Skoplaki. On the temperature dependence of photovoltaic module electrical performance: A review of efficiency/power correlations. *Elsevier - Solar Energy, Volume 83, Issue 5*, 2009.

[23] M.Kashiwagi. A b-spline galerkin scheme for calculating the hydroelastic response of a very large floating structure in waves. *Journal of Marine Science and Technology*, 1998.

[24] M.Kashiwagi. Transient responses of a vlfs during landing and take-off of an airplane. *Journal of Marine Science and Technology*, 2004.

[25] M.Kashiwagi. Research on hydroelastic responses of vlfs recent progress and future work. *Proceedings of the Ninth (1999) International Offshore and Polar Engineering Conference*, 1999.

[26] T. Hamamoto. Stochastic fluid-structure interaction of large circular floating islands during wind waves and seaquakes. *Probabilistic Engineering Mechanics, Vol. 10, Issue 4, pag. 209-224*, 1995.

[27] A.A. Korobkin T.I. Khabakhpasheva. Hydroelastic behaviour of compound floating plate in waves. *Journal of Engineering Mathematics, vol. 44. pag. 21-40*, 2002.

[28] Y.S.Choo M. Riyansyah, C.M. Wang. Connection design for two-floating beam system for minimum hydroelastic response. *Marine structures, vol. 23, Issue 1, Pag. 67-87*, 2010.

[29] Z.T. Tay C.M. Wang. Hydroelastic analysis and response of pontoon-type very large floating structures. *Bungartz HJ., Mehl M., Schäfer M. (eds) Fluid Structure Interaction II. Lecture Notes in computational science and engineering, Vol.73*, pages 103–130, 2010. doi: https://doi.org/10.1007/978-3-642-14206-2_5.

[30] W.Wei et al. A time-domain method for hydroelasticity of very large floating structures in inhomogeneous sea conditions. *Marine structures, Vol. 57*, pages 180–192, 2018.

[31] Liew M.S. Al-Yacouby A.M., Halim E.R.B.A. Hydrodynamic analysis of floating offshore solar farms subjected to regular waves. *Emamian S.S., Awang M., Yusof F. (eds) Advances in Manufacturing Engineering. Lecture Notes in Mechanical Engineering.*, pages 375–390, 2020. doi: https://doi.org/10.1007/978-981-15-5753-8_35.

[32] A. Rodriguez Marijuan. Offshore floating platforms: Analysis of a solution for motion mitigation (dissertation). *Student thesis*, 2017.

[33] V.J. et al. Kurian. Model tests for dynamic responses of float-over barge in shallow wave basin. *Paper presented at the Twenty-third International Offshore and Polar Engineering Conference, Anchorage, Alaska*, June 2013.

[34] S. Van Hoof. Hydroelastic wave deformation of very flexible floating structures: A performance study of a monolithic finite element model. *Master Thesis, Delft University of Technology*, 2021.

[35] Sebastian Schreier and Gunnar Jacobi. Experimental investigation of wave interaction with a thin floating sheet. *Proceedings of the International Offshore and Polar Engineering Conference*, 2020.

[36] E. Dombre et al. Simulation of floating structure dynamics in waves by implicit coupling of a fully non-linear potential flow model and a rigid body motion approach. *J.Ocean Eng. Mar. Energy (2015)*, pages 55–76, 2014.

[37] E. Guerber et al. A fully nonlinear implicit model for wave interactions with submerged-structures in forced or free motion. *Engineering Analysis with Boundary Elements, Vol. 36, Issue 7*, pages 1151–1163, 2012.

[38] Ikhennicheu et al. Analytical method for loads determination on floating solar farms in three typical environments. *Solar Energy, Vol. 219*, pages 34–41, 2021.

[39] DNVGL-RP-C205. Dnvgl-rp-c205: Environmental conditions and environmental loads. April 2014.

[40] M.Folley et al. A review of numerical modelling of wave energy converter arrays. *ASME 2012 International Conference on Ocean, Offshore and Artic Engineering (OMAE2012)*, June 2012.

[41] M.H. Aliabadi. *The Boundary Element Method Vol2: Applications in Solids and Structures*, volume 2. 01 2002.

[42] G. Delhommeau A. Babarit. Theoretical and numerical aspects of the open source bem solver nemoh. *In Proc. of the 11th European Wave and Tidal Energy Conference (EWTEC2015), Nantes, France*, 2015.

[43] J.M.J Journée and W.W. Massie. Offshore hydromechanics. *Delft University of Technology*, 2001.

[44] Y.S. Choo L. Sun, R. Eatock Taylor. Responses of interconnected floating bodies. *The IES Journal Part A: Civil and Structural Engineering*, August 2011. pages 143-156.

[45] Netherlands Enterprise Agency. Metocean investigations for the wind farm zone hollandse kust (noord) certification report metocean. *Netherlands Enterprise Agency*, November 2019.

[46] J.N. Newmann. Wave effects on deformable bodies. *Applied Ocean Research, Volume 16*, 1994. pages 47-59.

[47] O.M. Faltinsen. *Sea loads on ships and offshore structures*. Cambridge University Press, 1990.

[48] Gustavo Paulinelli Guimarães Rogério Pirk, Carlos d´Andrade Souto and Luiz Carlos Sandoval Góes. Acoustics and vibro-acoustics applied in space industry, modeling and mea-

surement methods for acoustic waves and for acoustic microdevices. *IntechOpen*, 2013. doi: 10.5772/49966.

[49] R.B. Inglis and W.G. Price. Irregular frequencies in three dimensional source distribution techniques. *International Shipbuilding Progress, ISP, Volume 28*, 1981.

[50] MATLAB Documentation. Smoothing splines. Consulted on the 20th of Januari 2022 from `https://nl.mathworks.com/help/curvefit/smoothing-splines.html`.

[51] Pasquale Dinoi. Analysis of wave resonant effects in-between offshore vessels arranged side-by-side. July 2016.

[52] Bernard Molin, Fabien REMY, A. Camhi, and Alain Ledoux. Experimental and numerical study of the gap resonances in-between two rectangular barges. 10 2009.

[53] Ivan Ekerhovd; Muk Chen Ong; Paul H. Taylor; Wenhua Zhao. Numerical study on gap resonance coupled to vessel motions relevant to side-by-side offloading. *Ocean Engineering*, 241, 2021. ISSN 0029-8018. doi: https://doi.org/10.1016/j.oceaneng.2021.110045.

[54] L. Sun, B. Teng, and C.F. Liu. Removing irregular frequencies by a partial discontinuous higher order boundary element method. *Ocean Engineering*, 35(8):920–930, 2008. ISSN 0029-8018. doi: https://doi.org/10.1016/j.oceaneng.2008.01.011.

[55] Amresh Negi and Sharad Dhavalikar. Estimation of roll damping for transportation barges. 05 2009.

[56] QuayQuip. Quayquip fenders - english a4 metric. Consulted on the 19th of May 2022 from `https://issuu.com/quayquip/docs/quayquip_fenders_en-a4-metric__v2.1l__web`.

[57] Eurocable. Steel wire ropes. Consulted on the 19th of May 2022 from `https://www.eurocable.be/nl/producten/staalkabels`.

Appendix A Overview results case 1

Table A.1: Overview of results for case 1 for $\mu = 0°$

Case	Param	Value [m] (% of max)	Fsig x-dir [N or Nm]	Fsig z-dir [N or Nm]
1.1	length	50 (20%)	1.1544E7	1.0814E6
1.2	length	100 (40%)	2.4351E7	1.9988E6
1.3	length	150 (60%)	4.5570E7	2.9484E6
1.4	length	250 (100%)	6.2449E7	4.7719E6
2.1	width	20 (26,6%)	1.5020E7	6.7673E6
2.2	width	35 (49.3%)	2.4351E7	1.9988E6
2.3	width	75 (100%)	3.3603E7	1.1484E7
3.1	draft	1 (10%)	5.7375E6	3.0511E6
3.2	draft	5 (50%)	2.4351E7	1.9988E6
3.3	draft	10 (100%)	4.9600E7	7.2025E6
4.1	gap	1 (13.3%)	2.1428E7	2.4624E6
4.2	gap	3.5 (46.7%)	2.4351E7	1.9988E6
4.3	gap	5 (66.7%)	2.4209E7	1.8007E6
4.4	gap	7.5 (100%)	2.4659E7	1.5265E6

Table A.2: Overview of results for case 1 for $\mu = 45°$ for joint 1

Case	Param	Value [m] (% of max)	Fsig x-dir [N or Nm]	Fsig y-dir [N or Nm]	Fsig z-dir [N or Nm]
1.1	length	50 (20%)	6.6382E6	2.4936E6	3.9252E6
1.2	length	100 (40%)	9.4396E6	5.4753E6	9.7610E6
1.3	length	150 (60%)	1.0548E7	6.1710E6	1.4430E7
1.4	length	250 (100%)	1.1792E7	4.7893E6	1.8646E7
2.1	width	20 (26,6%)	5.8957E6	2.9265E6	5.3436E6
2.2	width	35 (49.3%)	9.4396E6	5.4753E6	9.7610E6
2.3	width	75 (100%)	1.8582E7	6.7868E6	2.1714E7
3.1	draft	1 (10%)	2.2576E6	1.0459E6	1.0593E7
3.2	draft	5 (50%)	9.4396E6	5.4753E6	9.7610E6
3.3	draft	10 (100%)	2.1603E7	1.1014E7	9.6173E6
4.1	gap	1 (13.3%)	8.4196E6	5.2989E6	9.4426E6
4.2	gap	3.5 (46.7%)	9.4396E6	5.4753E6	9.7610E6
4.3	gap	5 (66.7%)	9.4615E6	5.5223E6	9.9175E6
4.4	gap	7.5 (100%)	9.8132E6	5.6162E6	1.0219E7

Table A.3: Overview of results for case 1 for $\mu = 45°$ for joint 2

Case	Param	Value [m] (% of max)	Fsig x-dir [N or Nm]	Fsig y-dir [N or Nm]	Fsig z-dir [N or Nm]
1.1	length	50 (20%)	6.9488E6	2.4936E6	3.3769E6
1.2	length	100 (40%)	1.1576E7	5.4753E6	9.1366E6
1.3	length	150 (60%)	1.2629E7	6.1710E6	1.3873E7
1.4	length	250 (100%)	8.2701E6	4.7893E6	1.8520E7
2.1	width	20 (26,6%)	6.3162E6	2.9265E6	4.4445E6
2.2	width	35 (49.3%)	1.1576E7	5.4753E6	9.1366E6
2.3	width	75 (100%)	2.0611E7	6.7868E6	2.3392E7
3.1	draft	1 (10%)	2.1787E6	1.0459E6	1.0582E7
3.2	draft	5 (50%)	1.1576E7	5.4753E6	9.1366E6
3.3	draft	10 (100%)	2.3888E7	1.1014E7	6.8865E6
4.1	gap	1 (13.3%)	1.10169E7	5.2989E6	8.6931E6
4.2	gap	3.5 (46.7%)	1.1576E7	5.4753E6	9.1366E6
4.3	gap	5 (66.7%)	1.1599E7	5.5223E6	9.2935E6
4.4	gap	7.5 (100%)	1.2011E7	5.6162E6	9.6642E6

Appendix B Overview results case 2

Table B.1: Overview of results for case 2 for $\mu = 0°$

Case	Param	Value [N/m or Nm/rad]	Fsig x-dir [N or Nm]	Fsig z-dir [N or Nm]	Fsig θ-dir [N or Nm]
2.1.1	axial	0	0	1.9004E6	1.0998E7
2.1.2	axial	10E3	7.1826E4	1.9004E6	1.0995E7
2.1.3	axial	10E6	4.2486E7	1.9004E6	1.2185E7
2.1.4	axial	10E9	2.4206E7	1.9004E6	1.1880E7
2.2.1	shear	0	4.2486E7	0	1.2185E7
2.2.2	shear	10E3	4.2486E7	7.2441E4	1.2185E7
2.2.3	shear	10E6	4.2486E7	1.9004E6	1.2185E7
2.2.4	shear	10E9	4.2486E7	2.0060E6	1.2185E7
2.3.1	bending	0	4.2649E7	1.9004E6	0
2.3.2	bending	10E3	4.2648E7	1.9004E6	1.2557E4
2.3.3	bending	10E6	4.2486E7	1.9004E6	1.2185E7
2.3.4	bending	10E9	3.8334E7	1.9004E6	2.0545E8
2.4.1	torsion	0	4.2486E7	1.9004E6	1.2185E7
2.4.2	torsion	10E3	4.2486E7	1.9004E6	1.2185E7
2.4.3	torsion	10E6	4.2486E7	1.9004E6	1.2185E7
2.4.4	torsion	10E9	4.2486E7	1.9004E6	1.2185E7

Table B.2: Overview of results for case 2 for $\mu = 45°$ for joint 1

Case	Param	Value [N/m or Nm/rad]	Fsig x-dir [N or Nm]	Fsig y-dir [N or Nm]	Fsig z-dir [N or Nm]	Fsig ϕ-dir [N or Nm]	Fsig θ-dir [N or Nm]	Fsig ψ-dir [N or Nm]
2.1.1	axial	0	0	6.9353E6	9.1148E6	1.7380E5	3.024E6	5.9955E5
2.1.2	axial	10E3	4.0215E4	6.9353E6	9.1148E6	1.7380E5	3.2997E6	6.0473E5
2.1.3	axial	10E6	1.3480E7	6.9353E6	9.1148E6	1.7380E5	4.3923E6	1.0313E5
2.1.4	axial	10E9	9.4071E6	6.9353E6	9.1148E6	1.7380E5	4.1081E6	86.0295
2.2.1	shear	0	1.3480E7	0	0	2.1737E6	4.3923E6	1.0313E5
2.2.2	shear	10E3	1.3480E7	4.8261E4	1.4830E5	2.1571E6	4.3923E6	1.0313E5
2.2.3	shear	10E6	1.3480E7	6.9353E6	9.1148E6	1.7380E5	4.3923E6	1.0313E5
2.2.4	shear	10E9	1.3480E7	5.4798E6	9.7637E6	186.4	4.3923E6	1.0313E5
2.3.1	bending	0	1.3589E7	6.9353E6	9.1148E6	1.7380E5	0	0
2.3.2	bending	10E3	1.3589E	6.9353E6	9.1148E6	1.7380E5	4.5725E3	103.2
2.3.3	bending	10E6	1.3480E7	6.9353E6	9.1148E6	1.7380E5	4.3923E6	1.0313E5
2.3.4	bending	10E9	1.1144E7	6.9353E6	9.1148E6	1.7380E5	7.4877E7	6.9341E7
2.4.1	torsion	0	1.3480E7	6.9353E6	9.1197E6	0	4.3923E6	1.0313E5
2.4.2	torsion	10E3	1.3480E7	6.9353E6	9.1197E6	173.9	4.3923E6	1.0313E5
2.4.3	torsion	10E6	1.3480E7	6.9353E6	9.1148E6	1.7380E5	4.3923E6	1.0313E5
2.4.4	torsion	10E9	1.3480E7	6.8877E6	6.7954E6	1.2653E8	4.3923E6	1.0313E5

Table B.3: Overview of results for case 2 for $\mu = 45°$ for joint 2

Case	Param	Value [N/m or Nm/rad]	Fsig x-dir [N or Nm]	Fsig y-dir [N or Nm]	Fsig z-dir [N or Nm]	Fsig ϕ-dir [N or Nm]	Fsig θ-dir [N or Nm]	Fsig ψ-dir [N or Nm]
2.1.1	axial	0	0	6.9353E6	8.5156E6	1.7380E5	3.3024E6	5.9922E5
2.1.2	axial	10E3	4.4849E4	6.9353E6	8.5156E6	1.7380E5	3.2997E6	6.0473E5
2.1.3	axial	10E6	1.6463E7	6.9353E6	8.5156E6	1.7380E5	4.3923E6	1.0313E5
2.1.4	axial	10E9	1.1549E7	6.9353E6	8.5156E6	1.7380E5	4.1081E6	86.0295
2.2.1	shear	0	1.6463E7	0	0	2.1737E6	4.3923E6	1.0313E5
2.2.2	shear	10E3	1.6463E7	4.8261E4	1.3183E5	2.1571E6	4.3923E6	1.0313E5
2.2.3	shear	10E6	1.6463E7	6.9353E6	8.5156E6	1.7380E5	4.3923E6	1.0313E5
2.2.4	shear	10E9	1.6463E7	5.4798E6	9.1358E6	186.4	4.3923E6	1.0313E5
2.3.1	bending	0	1.6544E7	6.9353E6	8.5156E6	1.7380E5	0	0
2.3.2	bending	10E3	1.6544E7	6.9353E6	8.5156E6	1.7380E5	4.5725E3	103.2
2.3.3	bending	10E6	1.6463E7	6.9353E6	8.5156E6	1.7380E5	4.3923E6	1.0313E5
2.3.4	bending	10E9	1.1626E7	6.9353E6	8.5156E6	1.7380E5	7.4877E7	6.9341E7
2.4.1	torsion	0	1.6463E7	6.9353E6	8.5206E6	0	4.3923E6	1.0313E5
2.4.2	torsion	10E3	1.6463E7	6.9353E6	8.5206E6	173.9	4.3923E6	1.0313E5
2.4.3	torsion	10E6	1.6463E7	6.9353E6	8.5156E6	1.7380E5	4.3923E6	1.0313E5
2.4.4	torsion	10E9	1.6463E7	6.8877E6	6.200E6	1.2653E8	4.3923E6	1.0313E5